Characterisation of casting defects in DC cast magnesium alloys

A thesis submitted to the University of Manchester for the degree of Doctor of Engineering in the Faculty of Engineering and Physical Sciences

2013

David Mackie

School of Materials

University of Manchester

Grosvenor Street

Manchester

Contents

Word Count: 40,520

List of Figures

List of Tables

Abstract

The University of Manchester

David Mackie

Engineering Doctorate

Characterisation of casting defects in DC cast magnesium alloys

25th July 2013

The continued interest in the use of magnesium alloys for new applications demand the successful production of high quality wrought alloys. Magnesium Elektron seek to reliably produce high quality alloy billets by the DC casting method combined with ultrasonic inspection. The main objectives of this study are to characterize the defects which are currently found in the material and to understand the ability of the ultrasonic inspection technique currently employed to detect the defects.

This study began by locating defects using the ultrasonic inspection method which were then characterised using X-ray Computed Tomography (XCT) 3D imaging technique. Attempts were then made to understand and simulate the mechanisms by which the defects form during the casting process. The simulations were used to investigate the flow patterns during casting and the growth kinetics of the intermetallic phase.

The initial phase of this research established that the defects found comprised of an entrained oxide film entangled with an abundance of intermetallic phase particles. These defects were found to be present in the size range of 0.5 – 5 mm, and were deleterious to the materials mechanical properties. Greater understanding of the ultrasonic inspection process was achieved and informed improvements to assisting the production of high quality feedstock.

Simulation of the formation of the defects indicated that there was a region in which the oxide films could form and be free to enter into the final cast product. Simulation of the growth of the intermetallic particles demonstrated that precipitation from the liquid occurs in the mould during which particles are carried by the melt flow and experiences a complex thermal history. The combination of the two phases was established to be due to entanglement of the oxide and particles which when combined will settle out of the melt as a single defect. Improved filtering and melt handling methods were recommended to eliminate the defects and reliably produce high quality alloys.

Declaration

No portion of the work referred to in the thesis has been submitted in support of an application for another degree or qualification of this or any other university or other institute of learning.

Copyright

Acknowledgements

I would like to thank my academic supervisors Dr Joe Robson and Prof Phil Withers and industrial supervisors Dr Mark Turski and Dr Tim Wilks for their support and guidance throughout this research project and without which this work would not have been possible. I would like to extend this appreciation to the members of staff at Magnesium Elektron who provided me with the necessary training, samples and many informative discussions.

The support provided by Dr David Stanley and the Engineering Doctorate Centre was invaluable throughout the project. I am very appreciative of the many courses they organised which were as large a part of my learning as this research.

I am also grateful to all the members of the Light Alloys Research Group at the University of Manchester who made my time in Manchester enjoyable and hope they continue to grow and find somebody to continue to organise and maintain C7 and their laboratory.

Most importantly I would like to acknowledge the support from Philippa and of my family for keeping me on track and supporting me through my time in Manchester.

1 Introduction

This introductory section will present background knowledge to this research and the fields of study within which is focused. The motivation for carrying out such a study will be discussed, identifying the importance of this work to the sponsor organisation Magnesium Elektron, U.K. and then present the objectives which are hoped to be achieved by completing this study.

An overview of the sponsor organisation for this research, Magnesium Elektron, U.K will be included in the motivation. This work will focus on a subject offered by them pertinent to their specific manufacturing process and kindly guided by their technical staff.

1.1 Background

Magnesium is the lightest of all structural metals, yet there is a surprising lack of knowledge of the characteristics and benefits this metal can offer. Discovered in 1808 by Sir. H. Davey, magnesium was not produced in any significant quantities until the early 20th century, prompted by the two world wars. Magnesium development was driven by war however commercial production of magnesium experienced a slump post war due to the large amount of scrap available for recycling and use. The main use of magnesium at this time was in the alloying of aluminium alloys and thus the price and availability was heavily controlled by the aluminium industry. The start of the 21st Century saw a change in the attitude towards magnesium alloys, this was due to the newly available high purity corrosion resistant alloys, increasing environmental pressure on automotive manufacturers, advances in production by a more efficient electrochemical reduction process in the Western world and the availability of low cost magnesium form China. As a result, magnesium usage has increased by 56% from 1993 to 2003 [King, 2007] mainly due to the availability of cheap magnesium from China and pressure to reduce pollution from automotive transport.

Volkswagen was the first automotive manufacturer to adopt magnesium in the Beetle model, used for the crankcases and transmission. In recent years the automotive sector has found many new applications for magnesium alloys and this is a trend that is predicted to continue increasing from 3 kg per vehicle in 2005 to 50 kg in 2015. Environmental conservation has driven the automotive manufacturers to focus on decreasing the weight of vehicle since the CO_2 emission is directly proportional to fuel consumption and car weight [Kulekci, 2008], the same can be said to be true for the aerospace industry.

Magnesium alloys offer a very good solution to cutting vehicle weight, directly cutting transport emissions, however they have not been adopted by automotive component manufacturers due to the high associated costs of processing compared with current materials. The costs associated with magnesium alloys will remain

high compared to other materials until significant developments are made in identifying new alloys and manufacturing processes.

One factor preventing the reduction in cost is due to the hexagonal close-packed structure of magnesium and the resulting limited ductility at room temperature [Kleiner et al., 2003]. As a result, wrought magnesium alloys possess limited formability at room temperature and require heating to above 225°C to be processed [Doege et al., 2001], adding large expense to forming processes. For this reason castings, in particular high pressure die castings, have dominated magnesium use in the automotive industry. Research is currently being done to identify new alloys which exhibit better formability at room temperature [Kleiner et al., 2003].

However, the development of casting methods capable of producing high integrity magnesium engineering components still lags behind those of aluminium. Manufacturers have often selected components produced by methods other than casting or other materials due to better reproducibility and reliability of mechanical properties. The presence of entrainment defects is one cause of increased scatter in the mechanical properties of castings. Entrained oxide films are often the cause of failure in aluminium casting [Cao, 2005; Fox, 2000] and the same has been shown to be true for magnesium alloys [Griffiths et al., 2001]. It is reported that through careful feeding design in castings entrainment defects can almost be entirely removed from casting [Campbell, 2003]. This means the theoretical values of strength can be achieved and the scatter in properties reduced. New manufacturing methods such as thixomolded or Melt-Conditioned High Pressure Die Casting (HPDC), traditional high-pressure die casting combined with a novel twin screw prior mixing stage [Tzamtzis et al., 2009], presents serious opportunities for automotive and aerospace manufacturers to produce high quality components competitively.

The continued development of new alloys and production methods can overcome the cost barrier, produce high quality castings and make magnesium alloys more

attractive to aerospace manufacturers, massively increasing the possible applications for magnesium alloys.

Commercial production and supply of wrought magnesium alloys is an important industrial process that is facing growing demand with even more potential applications for magnesium alloys in the future. The industries that present opportunities for magnesium engineering components are typically high performance and demand very high integrity components. Direct-chill (DC) casting is the most common production process for forging feedstock, however it is susceptible to the same defects that plague die casting and have the same effect on material strength. Defects produced during casting of feedstock are often still present in forged components, hence aerospace manufacturers will only accept the highest quality feedstock for forging. With the current production process and a rigorous inspection regime there is a drive to reduce the rejection rate of cast material. Clearly, a reduction in the rate of material rejection would result in the reduction in the cost in production.

A common technique used for the non-destructive testing (NDT) of cast magnesium alloy billets is automated immersion ultrasonic inspection. This technique provides economical, fast and repeatable imaging of the internal cast structure present in the billets. This technique permits the detection of internal defects, however at present the ability of this technique is limited to defect detection and does not permit any level of defect characterisation. Defect characterisation would help improve the understanding of the cause of formation of the defects that cause material to be rejected.

Advanced ultrasonic inspection techniques can achieve high levels of resolution and increasingly sophisticated detail of the internal structure, permitting 3D visualisation of the microstructure. However, utilising ultrasonic techniques in a commercial environment places limitations on the level of detail achievable due to restrictions on scanning times and equipment capabilities. Development of the available NDT techniques will enable more accurate inspection to become routine

and reduce the amount of material that is unnecessarily scrapped, directly reducing the costs associated with production.

By characterising the defects that form and at the same time achieving greater inspection accuracy, it is hoped that the scrappage rates can be reduced and confidence in the quality of the material being produced increased. By doing so the cost could be lowered making magnesium alloys more attractive to new applications. The success of this will mean the transport industry will be able to utilise magnesium alloy in their quest to reduce emissions.

1.2 Motivation

The growing use of magnesium alloys by more industries in the future depends on the development of alloys and production methods. For magnesium alloys to be adopted, effective production techniques need to be established to ensure a high quality product is achievable and suitable for industrial requirements. This provides the stimulus for research into both the production of high quality material and a reliable non-destructive inspection technique.

Magnesium Elektron, a division of the Luxfer Group, is an international materials technology company specialising in the design, manufacture and supply of high-performance magnesium materials and components. With manufacturing operations in the United Kingdom, North America and Czech Republic, Magnesium Elektron employs 400 staff across all locations. Focussed on continued improvement and the development of new magnesium technologies Magnesium Elektron is responsible for developing alloys for use in aerospace, automotive, power generation and biomaterials. With a Research Centre at their Manchester, U.K. site, Magnesium Elektron seek to improve the quality of their wrought alloy product offering, the area of research this project is concerned with.

Magnesium Elektron produces over 3,000 tonnes of magnesium products per year at its Manchester plant and approximately half of the alloys produced are by the

direct chill casting process. DC cast products are typically used for wrought alloys (forgings and extrusions).

The presence of large inclusion type defects within the cast billet have prevented clearance of the necessary quality checks demanded by the aerospace organisations. This presents two areas of research in order to prevent the continued rejection of material produced to substandard quality levels. The first is to study the production method and how process can be improved to limit the defects contained in the produced material. The second is to understand the best inspection method and how to locate any defects with the highest accuracy such that quality standards can be applied with the greatest confidence.

The incentive to complete the identified studies was to enable the reliable production of high quality magnesium alloys suitable for the aerospace industry with a lower associated production cost than at present. This requires establishing a reliable production method for producing high quality feedstock with reduced incidents of failure at inspection. In addition to improving the quality of the castings, validation of a robust method of carrying out non-destructive inspection suitable for an industrial environment is also needed. Achieving these goals would present a massive opportunity to a magnesium alloy producing organisation due to the decrease in scrapped material and improved delivery of quality product to meet the customer's needs. The ability to produce, at lower cost, magnesium castings certified to a higher quality standard would provide opportunities for new applications and sales, particularly to customers in the aerospace sector.

1.3 Objectives

As this engineering doctorate research project focuses on the specific situation of a single magnesium alloy production organisation, Magnesium Elektron U.K., the aims and objectives are tailored to their requirements. However, the outcomes may be relevant to other organisations in the same industry who wish to achieve the same results.

The overall aim of this research project is to enable the reliable production of high quality magnesium alloy forging feedstock by DC casting without incurring any additional costs than at present. This is to be achieved by two approaches (1) developing a casting process for the production of such material and (2) establishing a reliable inspection technique suitable for the demands of industry.

The first objective is to propose strategies to reduce the occurrence of unacceptable sized defects during production by DC casting. This is the most important objective for the whole project.

This objective will be achieved when the typical defects are fully characterised and the processes by which they form is understood. Once the formation processes are known these can be studied and modifications to the casting process proposed to prevent defects from forming. The modifications must enable production of higher quality material than is presently obtainable while maintaining or reducing the current associated costs.

Establishing a reliable inspection technique will focus on the use of ultrasonic immersion inspection, as currently used by Magnesium Elektron U.K. The aim will be to understand the ability of the ultrasonic equipment to locate defects and provide an assessment of the quality of the billet. Through understanding the responses generated by the defects the suitability and limitations of this technique will be established. Validating the presence of a defect in the location identified by the ultrasonic equipment, for a number of samples, will demonstrate the reliability of this technique. The benefit of this will be that a greater understanding in correlating the defect types to ultrasonic response will be possible and a less conservative assessment can then be made when identifying products satisfying the customer's needs, thus reducing rejection rates. This objective will be met when full confidence in the inspection results is possible.

2 Literature Review

This section will introduce the subjects and the relevant literature pertinent to this study. This includes a discussion of magnesium alloys, the DC casting production method and non-destructive inspection methods including a review of their limitations, which will frame the scope of this research project.

Particular focus will be placed on the casting method and the defect types reported for magnesium alloys. As an objective of this project is to identify the defects which are causing the material to fail inspection and recommend improvements to the current casting method such that clean material can be produced.

2.1 Magnesium Alloys

This section contains a review of the literature relevant to the study of magnesium alloys and their application as engineering materials. The focus is on the metallurgical factors such as alloying and solidification on the microstructure and properties of the alloys used in this study.

2.1.1 Magnesium: Properties, alloys and applications

Magnesium can be produced form a wide range of sources and by a range of methods. There are six sources of raw materials containing magnesium, the three most common sources are dolomite ($MgCO_3.CaCO_3$), magnesite ($MgCO_3$) and sea water, no metallic magnesium is found in nature [Friedrich and Mordike, 2004]. The two main extraction routes are thermal and electrochemical. The thermal method involves the heating of dolomite until thermal decomposition occurs in the presence of lime (CaO) and these are reduced by Silicon (Si) to produce magnesium metal in the gaseous form and dicalcium silicate.

$$2CaO + 2MgO + Si \rightarrow 2Mg + Ca_2SiO_4$$

The electrochemical process uses direct current electricity which discharges chlorine and magnesium ions into gaseous chlorine and metallic magnesium [Friedrich and Mordike, 2004]. The raw materials are often the source of impurities in the final product, which are also introduced by the equipment or tooling, iron or carbon commonly enter the melt in this manner [Engh, 1992].

Magnesium has an atomic diameter of 0.32 nm and atomic weight of 24.31. The crystal structure of pure magnesium is hexagonal close packed with lattice parameters a = 0.321 nm and c = 0.521 nm. Magnesium presents the opportunity for alloying due to the vast range of elements that it can form a solid solution with - especially useful is the high level of solubility with aluminium and zinc. It is the wide range of possible alloying additions that give rise to the diverse array of magnesium alloys available as useful materials for engineering applications.

Typically magnesium alloys contain 10 per cent or less of other alloying elements, which are usually added primarily to improve strength [Engh, 1992]. Alloying elements are also used to control texture (Rare Earths), control impurities (Mn), decrease flammability or to control corrosion resistance.

Alloying is usually achieved when pure magnesium is in the molten state and the alloying elements are added to the melt in the form of pure elements, hardeners or compounds. The hardeners and compounds react when added to the molten magnesium and the alloying elements remain and enter into a liquid solution. In addition to this it is considered favourable for the alloying elements to posses a lower solubility limit at a lower temperature resulting in an alloy with potential for further strengthening by formation of precipitates (age hardening).

The magnesium-aluminium-zinc-manganese alloy system, presents solutions to many engineering applications and has the potential to be used in many more. Currently AZ91 alloy is used in many portable communication devices such as mobile phone and laptop chassis which are produced by die casting and thixomoulding. However, AZ80 is a wrought alloy commonly used in aerospace applications as forged components. The most common processing method of the AZ system is high-pressure die casting , due to its excellent castability, which enables the production of long thin sections desirable for information and communications technology. The wrought production route is often impeded by defects that limit the mechanical properties of the final components. The quality of the cast feedstock used to produce the components is important as many defects present in the stock material will be present in the final product [Dahle et al., 2001].

2.1.2 Nomenclature and Temper Designations

The nomenclature and designations for magnesium alloys and the associated heat treatments follows the method proposed by the American Society for Testing and Materials (ASTM). The format is such that the first two letters indicate the main alloying elements following the convention in Table 1.

Letter	Alloying Element
A	Aluminium
C	Copper
E	Rare Earth (RE)
H	Thorium
K	Zirconium
L	Lithium
M	Manganese
Q	Silver
S	Silicon
W	Yttrium
Z	Zinc

Table 1 Nomenclature for alloying elements in Magnesium alloys.

The letters are ordered according to the quantity of the element present, and if the quantity is the same the letters are listed alphabetically. The numbers which follow the letters indicate the respective weight % of the alloying elements in the same order. However, there are limitations with this system since the stated weight percentages are rounded to the nearest whole percentage therefore actually indicate a range of content and additionally there is no information on the additional alloying elements. An example of this is AZ80 which has the actual composition, Al-8.5 wt.%, Zn-0.5 wt.% and Mn-0.12 wt.%, plus other minor additions.

The heat treatment conditions are similar to those used for other materials such as aluminium alloys and follow the convention summarised in Appendix 1.

2.1.3 Effect of Alloying Elements

2.1.3.1 Aluminium

Aluminium containing alloys are the oldest group of magnesium alloys that were developed and were extensively used in the First and Second World War. Aluminium containing alloys are a distinct group that consist of a much coarser microstructure than that of the zirconium containing group. This is because grain refinement is less effective in these alloys, discussed further in section 2.1.4.

Aluminium containing magnesium alloys are the most widely used commercial alloys available and have increasing applications in transportation industries such as aerospace and automotive.

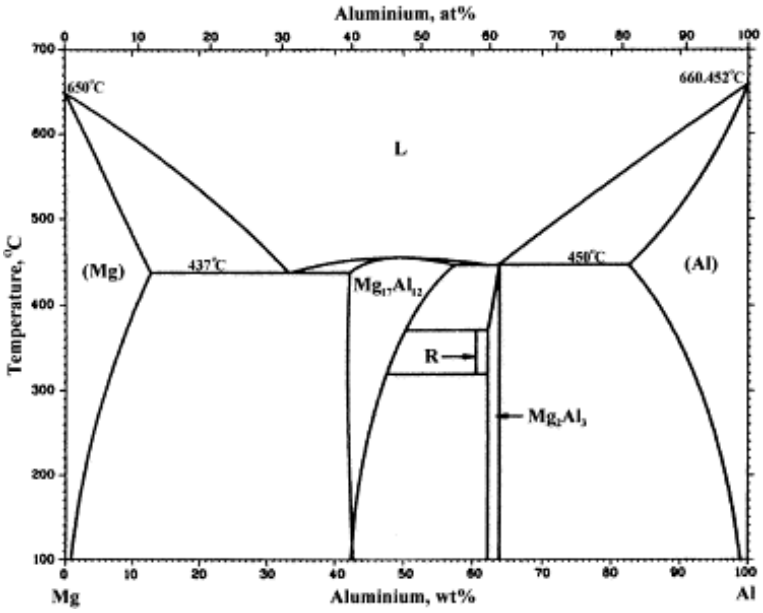

Figure 2-1 Mg-Al binary phase diagram [Dahle et al., 2001].

Aluminium is added principally to improve the fluidity of the melt and provide strengthening; however it also acts to increase the freezing range which directly increases the tendency to form shrinkage porosity defects. The maximum strength is achieved at around 8 to 10 wt.% aluminium content and most commercial cast alloys are found to be within this range. Aluminium has a maximum solubility in magnesium of 12.7 wt.% at 437°C, Fig. 2-1, which is reduced to 2 wt.% at room temperature [Dahle et al., 2001]. The result of this change in solubility level with temperature is the precipitation of the $Mg_{17}Al_{12}$ (β) phase which is stronger but significantly more brittle than the alpha Mg phase. The β-phase typically forms at grain boundaries as isolated particles or discontinuous precipitation when the cooling rate is slow. Precipitation of the β-phase via age hardening treatments is possible, but the strengthening response is only modest.

2.1.3.2 Zinc

In aluminium containing alloys zinc acts to improve the fluidity of the melt and improves room temperature strength by solid solution strengthening; zinc is more effective in strengthening this way than aluminium. The maximum addition of zinc to AZ alloys is around 1 – 2 wt.% at which level it does not contribute to age hardening. The magnesium – zinc binary alloy system forms a eutectic at 51.3 wt.%, Fig 2-2.

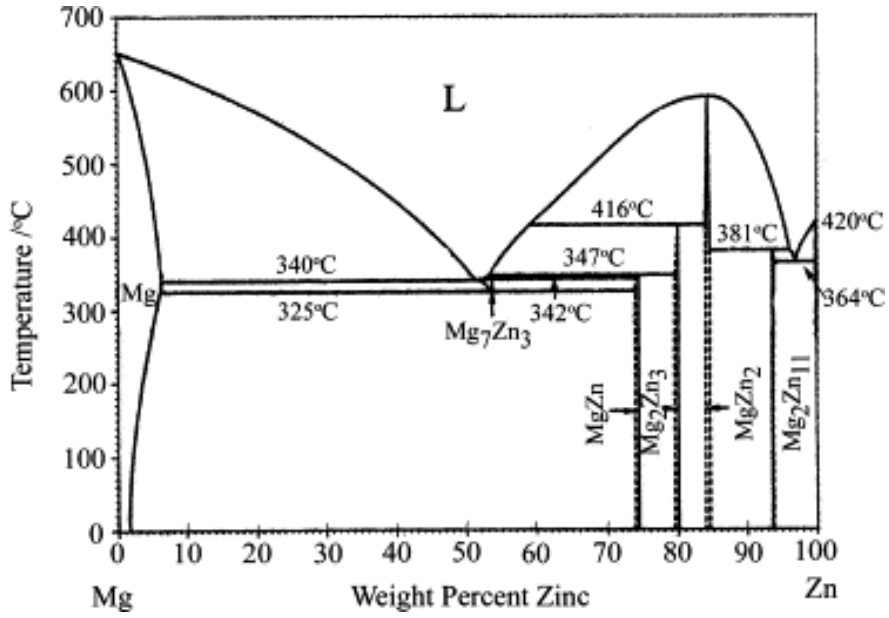

Figure 2-2 Mg-Zn binary phase diagram [Baker, 1992].

Magnesium-zinc alloys are a system of age-hardenable alloys which follow a complex age hardening process and are typically used in the T5 or T6 conditions. The age hardening response can be improved by the addition of copper resulting in greatly improved ductility and elevated temperature stability. The Mg-Zn system alloys suffer from microporosity and thus are not used as commercial castings [Polmear, 1995]. Most aluminium free zinc containing magnesium alloys, which contain a small amount of zirconium, are used as extrusion material due to the insensitivity to extrusion conditions and high strength [Bettles and Gibson, 2005].

2.1.3.3 Manganese

Manganese is added to improve the corrosion resistance of the aluminium containing alloys by forming intermetallic compounds which remove iron from the melt [Friedrich and Mordike, 2004; Sin et al., 2007]. The intermetallic particles that form with iron in the melt are denser than the molten alloy and sink to the bottom, thus will not be poured into the final casting. Iron is found in molten magnesium since steel crucibles are typically used in the melting and holding of the alloys and during the time in crucibles the melt becomes enriched in iron. The effectiveness of these intermetallic particles as heterogeneous nucleation sites for α-phase magnesium grains is a matter of debate [Guang et al., 2009; Fan et al., 2009; Zhang et al., 2005]. Manganese also forms a range of intermetallic phases consisting of different proportions of aluminium and manganese, the aluminium-rich manganese aluminide Al_6Mn is stable at temperatures up to 685°C whereas Al_8Mn_5 can coexist with the melt at a wide range of temperatures [Ye and Liu, 2006]. There is a narrow temperature range where both $Al_{11}Mn_4$ and Al_8Mn_5 may form; otherwise only one of the phases will be present [Laser et al., 2006].

2.1.3.4 Zirconium

Zirconium is the most effective grain refining alloying addition known for magnesium alloys. This is due to the zirconium having the same crystal structure as magnesium and very similar lattice constants [Qian and StJohn, 2009]. The maximum solubility of zirconium in magnesium is 0.6 wt.% at 780°C and can often result in a decrease of grain size by 80% [Qian et al., 2003]. Zirconium can not be added to any magnesium alloys that contain aluminium or silicon as it readily forms stable compounds with these elements which poisons the grain refining effect [Polmear, 1994]. However, zirconium can also replace manganese as an alloying addition which will remove iron from the melt. Thus zirconium is commonly employed as an iron remover to improve the corrosion resistance of an alloy and can often result in iron levels being reduced to below 0.002 wt.%. Zirconium alloying is usually achieved through the use of Zirmax, a master alloy produced by Magnesium Elektron, UK, which contains around one third of zirconium by weight.

2.1.4 Grain Refinement

In Mg-Al alloys, which naturally produce a coarse grain microstructure, there is a need for some form of grain refinement. This can not be achieved through addition of the highly effective zirconium due to the poisoning effect already discussed. Magnesium alloys have a much larger Hall-Petch coefficient than other alloys such as aluminium alloys. Thus grain refinement is a much more efficient method to improve mechanical properties of a magnesium alloys than for other alloy systems [Fan et al., 2009].

There are traditionally two approaches for grain refinement of Mg-Al alloys these are carbon inoculation or super heating of the melt. It is reported [Polmear, 1996] that to achieve grain refinement it is necessary to superheat the melt to a temperature of 850˚C, at which it is held for around 30 minutes and then cooled to the desired casting temperature. This technique can result in a fine grain size however a true understanding of the mechanisms that cause the fine grain size is not clear. An alternative approach that presents a more practical solution is carbon inoculation which has the benefits of prolonging furnace and crucible lives as it involves lower operating temperatures than super heating. Carbon inoculation involves the addition of volatile carbon-containing compounds to the melt, these compounds are added to the melt and held at the bottom until the carbon dissociates into the melt. The grain refining is considered to be caused by inoculation of Al_4C_3 particles which are regarded to be very potent nucleation sites for magnesium [Campbell, 1993; Dahle et al., 2001; Cao et al., 2007].

However carbon inoculation is not as effective as zirconium for grain refinement and thus the benefits of the fine grain microstructure and the associated improved mechanical properties cannot be reliably achieved in AZ alloys [Dahle et al., 2001]. A novel method of grain refinement is by high-intensity ultrasonic treatment which demonstrates more potency than carbon inoculation. This technique relies on the cavitation of bubbles which acts to increase the undercooling and directly increases the nucleation rate, however industrial application of this technique is very limited

[Chen and Wei, 2007; Ramirez et al., 2008]. An alternative and novel approach to grain refinement has been proposed [Fan et al., 2009] which utilises the melt-conditioning and advanced shear technology which will fragment all oxides present in the melt due to the extremely high shear rates. The then fragmented oxides will act as potent nucleation sites in magnesium alloys which has been shown to have a dramatic reduction in grain size in DC cast AZ alloys, shown in Fig. 2-3.

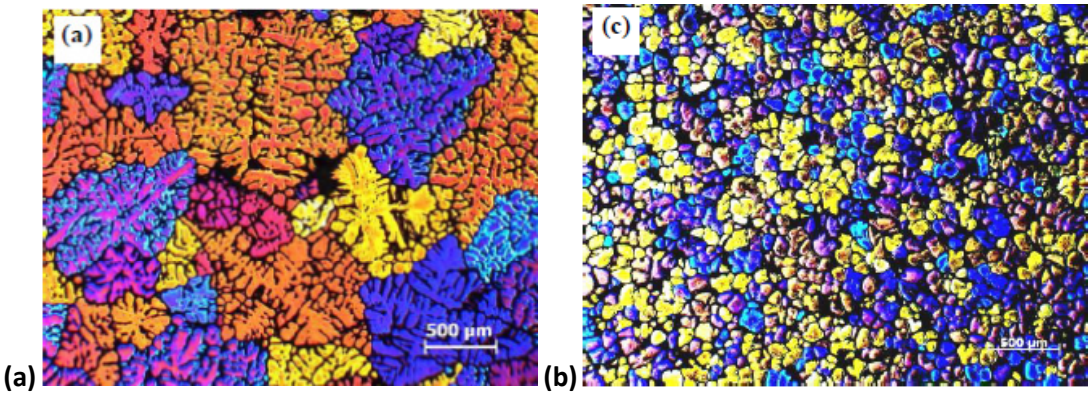

Figure 2-3 Comparison of reported cast microstructures in AZ91 (a) DC cast, (b) MC-DC cast, demonstrating significant grain refining [Zuo et al., 2011].

2.1.5 Solidification

The magnesium rich end of the binary Mg–Al phase diagram is shown in Fig. 2-4 below. As can be seen, the solubility of aluminium is high at the eutectic temperature (~12 wt.%), but decreases on cooling. This suggests age hardening may be exploited in this system to increase strength, with the expected β-phase precipitating out of solution on cooling [Fox et al., 1943].

The main features of the AZ80 microstructure are the primary magnesium dendrites which form just above 600˚C. According to the Mg-Al phase diagram it is clear there is a eutectic temperature of 436˚C, at which a eutectic phase is formed involving a primary magnesium phase (α-Mg) and $Mg_{17}Al_{12}$ (β). The $Mg_{17}Al_{12}$ phase is known to form when the aluminium content is above 2 wt.% and non-equilibrium cooling conditions are experienced, when this is exceeded it is expected that the eutectic will form. Observations by Ohno *et al.* have confirmed that in practical

castings, the solidification proceeds under non-equilibrium conditions close to that expected from the Scheil approximation [Ohno et al., 2006].

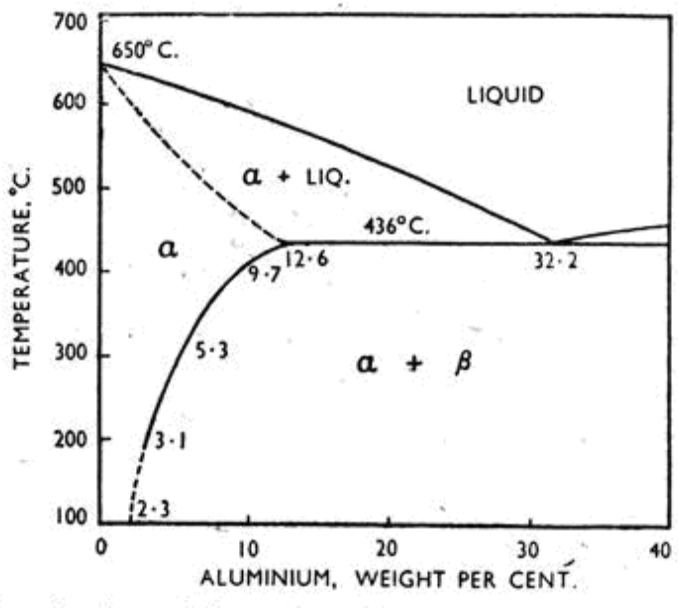

Figure 2-4 Magnesium rich end of Mg-Al phase diagram.

The presence of manganese in commercial AZ alloys leads to the formation of additional phases during casting, as was discussed in section 2.1.3.3. No intermetallic phases are expected in the magnesium-manganese binary alloy system but a series of manganese aluminide particles can be formed in the Al-Mn binary system and are also known to form in the Mg-Al-Mn ternary system. In particular the Al_8Mn_5 aluminide can co-exist with Mg-Al-Mn melt, Fig. 2-5, and can form large particles, reported to range from 0.1-30 µm in diameter [Sin et al., 2007] that are retained in the final casting. The fraction of these particles is known to increase with increasing manganese content [Ye and Liu, 2006]. These Al_8Mn_5 particles are stable and form in the melt as is shown in Fig. 2-5.

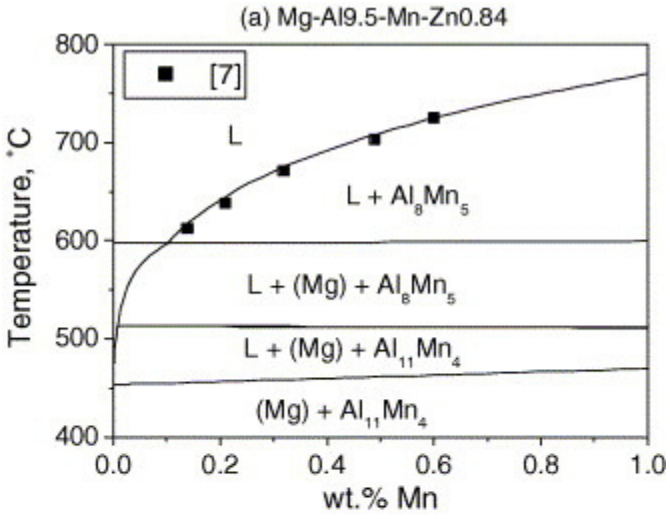

Figure 2-5 Section of a Mg-Al-Mn phase diagram, at Mg-Al9.5-Mn-Zn0.84 [Ohno et al., 2006].

2.1.6 Eutectic Formation

The formation of a eutectic structure involves the nucleation and growth of a second phase. As the liquid solidifies, both α and β phases grow simultaneously, Fig. 2-6, resulting in a solid-liquid interface perpendicular to the direction of growth. As a result the liquid immediately in front of lamellae becomes enriched in the component of the neighbouring lamellae thus transverse diffusion occurs allowing each lamellae to continue growing. A range of eutectic structures may form, however all consist of two phases in a binary alloy.

The solidification process influences and controls the size, shape and distribution of the brittle β-phase involved in the eutectic which directly influences the ductility and creep properties of AZ alloys [Dahle et al., 2001; Fox et al., 1943].

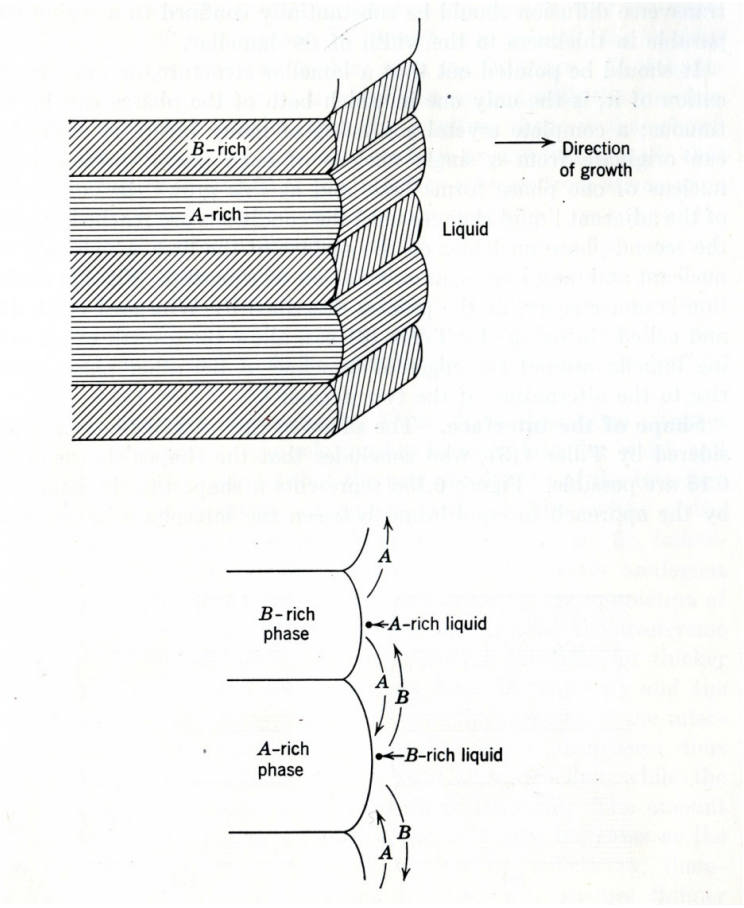

Figure 2-6 Eutectic growth mechanisms and diffusion paths for lamellar eutectic [Chalmers, 1964].

Commercial AZ alloys such as AZ91 are known to form fully or partially divorced eutectic structures, Fig. 2-7 [Dahle et al., 2001]. These differ in morphology; the fully divorced morphology consists of a region of β-phase surrounded by α-Mg which has grown from magnesium dendrites, Fig. 2-7(a). The partially divorced eutectic morphology consists of an isolated region of α-Mg eutectic surrounded by β phase but the bulk of the α-Mg is outside of the β-phase region, Fig. 2-7(b). The occurrence of each type of eutectic depends on the aluminium and zinc contents and the cooling conditions. The general impact is that increasing aluminium content results in a less divorced eutectic but an increase in zinc content and cooling rates will result in more divorced eutectic [Dahle et al., 2001].

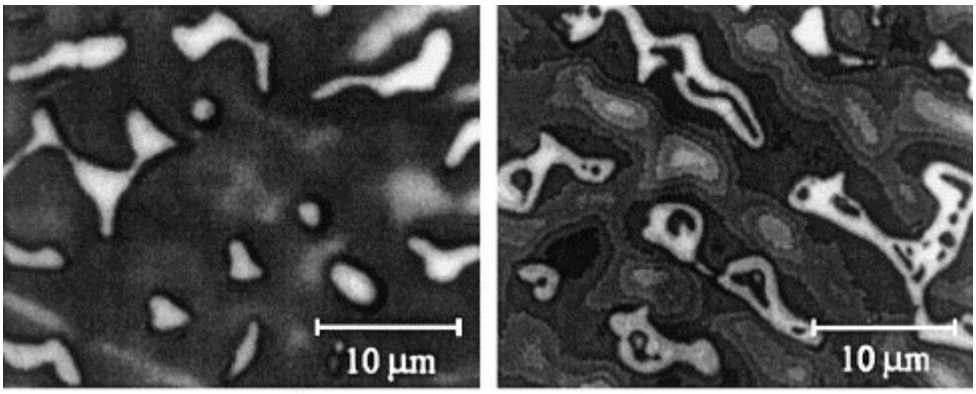

Figure 2-7 (a) Fully divorced and (b) partially divorced eutectic morphologies in Mg-Al alloy. The dark regions are high Al content α-Mg, the grey areas are primary α-Mg and the light areas are β-Mg17Al12 [Dahle et al., 2001].

2.1.7 Precipitation Reactions

The aim with some magnesium alloys is to form precipitates which are the result of the addition of a range of alloying elements. However, many Mg-Al systems present very little precipitation hardening and have alloying elements added primarily to improve fluidity and castability with the secondary aim of strengthening. The addition of zinc to Mg-Al alloys can reduce the solubility of aluminium in magnesium thus increasing the precipitation on ageing, resulting in a moderate increase in strength [Xu et al., 2009]. The effect of age hardening in Mg-Al alloys is known to be significantly less than is observed in some aluminium alloys. The lack of finely dispersed metastable precipitates, as in aluminium and other magnesium alloys, is partly responsible for this, with the β-phase precipitating directly from the magnesium matrix as large, widely spaced particles as described in the eutectic structures above [Polmear, 1996; Mordike et al., 2001].

Fox *et al.* report that the 'as-cast' structure often showed β-phase in lamellar form which had been precipitated from the solid solution during cooling after solidification was completed, demonstrating that formation of the β-phase occurs both during and after solidification. In addition, the β-phase is recognised to precipitate out of the magnesium solid solution in both the continuous and

discontinuous form, with the dominant form depending on precipitation temperature [Dahle et al., 2001; Ohno et al., 2006; Ohno et al., 2006(b)].

The β-phase is reported to precipitate directly from the super saturated areas of the α-Mg and can take place either continuously or discontinuously. Most precipitation occurs by the discontinuous form which involves the growth of lamellar precipitates of β-phase into the α-Mg grains at high angle grain boundaries, Fig. 2-8, with a morphology resembling that of pearlite growth in steel [Zhao et al., 2008]. This results in a moving grain boundary leaving a lamellar structure behind. Continuous precipitation forms in the remaining regions of α-Mg super saturated with aluminium. It is reported that these two forms of precipitation may occur simultaneously and that the two different mechanisms compete [Dahle et al., 2001; Braszczynska-Malik, 2009; Celotto, 2000].

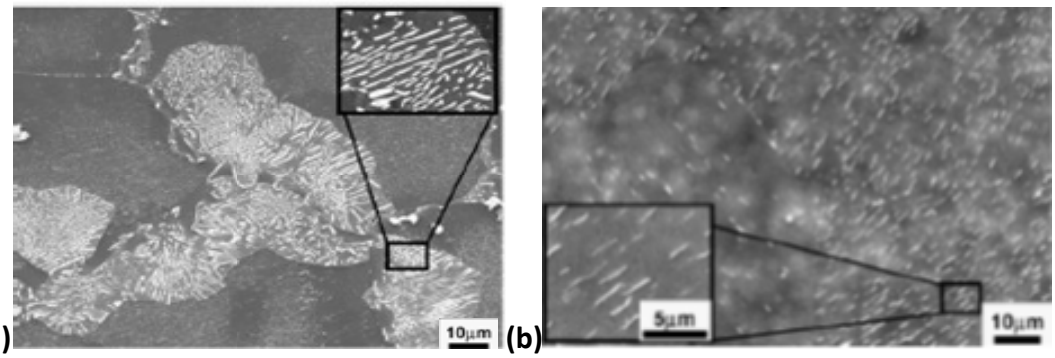

Figure 2-8 (a) Discontinuous precipitation of β-phase at grain boundaries, (b) lathe shaped continuous precipitation of β-phase within grains [Xu et al., 2009].

The precipitation of one phase from another occurs in attempt to reduce the free energy of the system and can vary depending on the crystal structure of the phases involved and also at the location at which the precipitation occurs. The ultimate shape of the precipitate depends on how the system achieves a minimum free energy through optimization of the total interfacial energy and the precipitate to matrix orientation relationship [Porter et al., 1992].

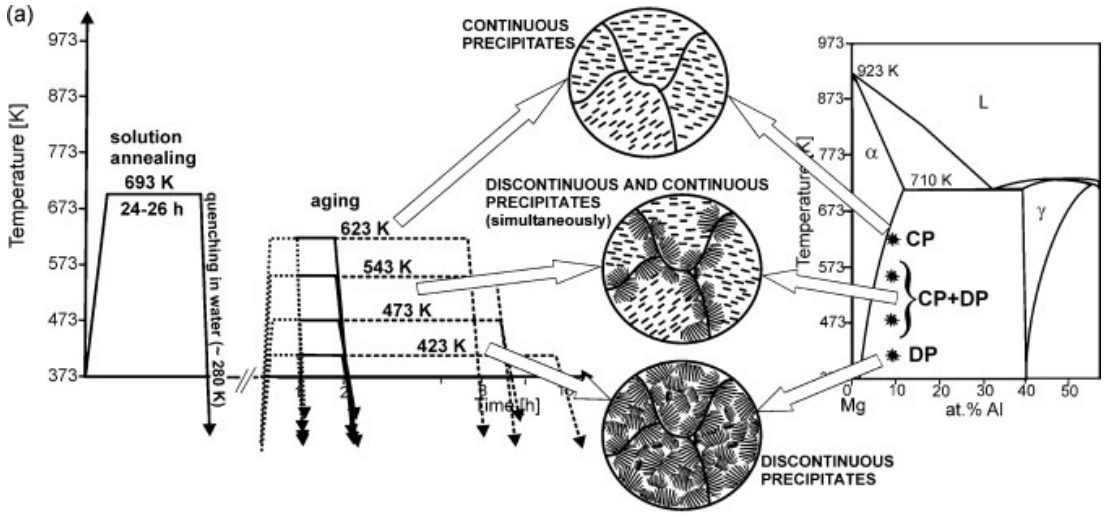

Figure 2-9 Schemes of possible precipitation in Mg-Al alloys depending on heat treatment of supersaturated solid solution [Braszczynska-Malik, 2009].

The discontinuous precipitation can take different forms and produce a range of microstructures as a result of different heat treatments, Fig. 2-9. However at higher ageing temperatures (~623K) continuous precipitation is favoured and at lower temperatures (~423K) discontinuous precipitation only is favoured, any heat treatment in the middle of these limits will result in both precipitation modes being present [Braszczynska-Malik, 2009; Xu et al., 2009]. The discontinuous precipitates are reported to form in three different growth morphologies; cellular, which consists of lamellae or oval-shaped ellipsoid and intergranular precipitate which is considered to be detrimental to mechanical properties of the alloy [Lai et al., 2009]. The discontinuous precipitation will continue to grow into the α-Mg grain until the grain is full or continuous precipitation begins to impede the growth.

2.1.8 Strengthening Mechanisms in Magnesium Alloys

Aluminium containing magnesium alloys are noted for their poor response to age hardening, however there are other mechanisms present that contribute to the strength of the alloys. The strength and ductility of cast magnesium alloys can be influenced by the effectiveness of the alloying additions to act as solid solution hardeners, to form second phase particles, and to produce grain refinement along with the consequences of any heat treatment [Caceres et al., 2002].

The β-phase precipitates are identified as a strengthening mechanism present in high aluminium content AZ alloys (Al>6 wt.%); however the effectiveness of the strengthening depends heavily on the precipitate morphology. There are several morphologies identified including the continuous and discontinuous precipitates discussed earlier and by other authors [Dahle et al., 2001; Lai et al., 2009; Braszczynska-Malik, 2009; Celotto, 2000; Caceres et al., 2002; Xu et al., 2009]. Detailed studies on the precipitate morphologies and their contribution to strengthening enables a better understanding of the strengthening mechanisms and how to achieve the most effective strengthening precipitates by heat treatment and control of composition.

It is reported that the main strengthening mechanisms present in the AZ91 alloy are grain boundary strengthening, solid solution hardening by the aluminium and zinc atoms, Orwan looping and dispersion hardening by the β-phase $Mg_{17}Al_{12}$ particles [Caceres et al., 2002]. Grain boundary strengthening is often the most potent strengthening mechanism in non-age hardening (low Al content) magnesium-aluminium alloys and the dependence of strength on grain size will follow the Hall-Petch relationship where the strength is proportional to the reciprocal of the square root of the grain size [Friedrich and Mordike, 2004 ; Lu et al., 2000; Srivatsan and Wie, 1995]. The strengthening effect of the β-phase can be important when the aluminium content in the alloy exceeds 6 wt.% [Lai et al, 2009]. However there is a notable difference in the peak hardness as a direct result of different ageing temperatures which is associated with the difference in volume fraction of the precipitates formed and most importantly the morphology of the precipitates involved, as discussed in the previous section.

2.1.9 Oxides in Magnesium Alloys

Due to the high affinity with oxygen and the high vapour pressure, molten magnesium rapidly oxidises when exposed to air. A cover gas is thus required in all stages of processing. Alternative methods have been used in the past such as alloying elements to reduce oxidation or the use of fluxes during the preparation of

a melt, however none were are as successful as cover gasses [McGlade and Baker, 2013]. If no cover gas is used the oxide film formed will not protect the melt from further oxidation and will act to increase the oxidation rate leading to burning on the melt surface [Cashion et al., 2002]. If molten magnesium is exposed to moist air magnesium hydroxide ($Mg(OH)_2$) will form on the melt surface. However, due to the high temperatures involved this film will be immediately dehydrated into MgO [Chen and Wei, 2007]. The formation of MgO on the melt surface is the result of oxidation, yet MgO occupies less volume than the magnesium used to make it and is porous. As a result magnesium vapour penetrates the oxide film and forms MgO fume above the film, which involves a highly exothermic reaction, directly accelerating oxidation. The use of the correct cover gas mixture will result in the formation of a stable oxide film on the film surface preventing oxidation. A commonly used cover gas mixture is that of air or CO_2 and sulphur hexafluoride (SF_6), which will act as an inhibitor, however the actual mechanism of protection are not fully understood [Cashion et al., 2002]. There is a growing demand to find an alternative to SF_6 due to the increasing cost of the gas and due to environmental concerns, most importantly the future growth of magnesium demand relies heavily on the much reduced life-cycle environmental impact compared to other engineering materials, which using SF_6 seriously erodes [Gjestland et al., 1996]. Other less harmful gasses are commonly employed in industrial production of alloys such as R134 mixed with nitrogen.

A consequence of the tendency for oxide films to form on the surface of magnesium alloy melts is that they can become entrained into the melt. It was demonstrated [Fan et al., 2009] that magnesium oxide (MgO) films actually consist of fine oxide particles. These oxide films can come from a range of sources and those developed during melt handling are termed young films, old oxide films are those formed on the melt surface and oxide skins are those present from ingot surfaces. It was suggested that these oxide particles can act as potent nucleation sites for both α-Mg and Al_8Mn_5 phases once they are sheared in the melt, to produce a more desirable microstructure. However, Campbell suggests that oxide films will act as favoured nucleation sites for a wide range of intermetallics but not

the matrix phase itself [Campbell, 2006]. Campbell suggests that the $Mg_{17}Al_{12}$ phase will form on the MgO surface film on a magnesium melt, whereas Fan *et al.* identify the Al_8Mn_5 as the phase most likely to nucleate on a magnesium alloy melt oxide film. The discussion on Al_8Mn_5 nucleating on oxides is on-going as little experimental evidence exists to confirm either mechanism.

Entrained oxide skin, if present in significant quantities, can dramatically reduce the fluidity of a melt [Ravi et al., 2008]. This has a significant impact on the quality of the final cast product which may not be completely filled or reproduce the fine detail required during some shape casting processes. Entrained oxide films have also been reported and imaged [Wang et al., 2009], Fig. 2-10, in AZ91 alloy. They are often associated with porosity, and have a deleterious effect on the mechanical properties.

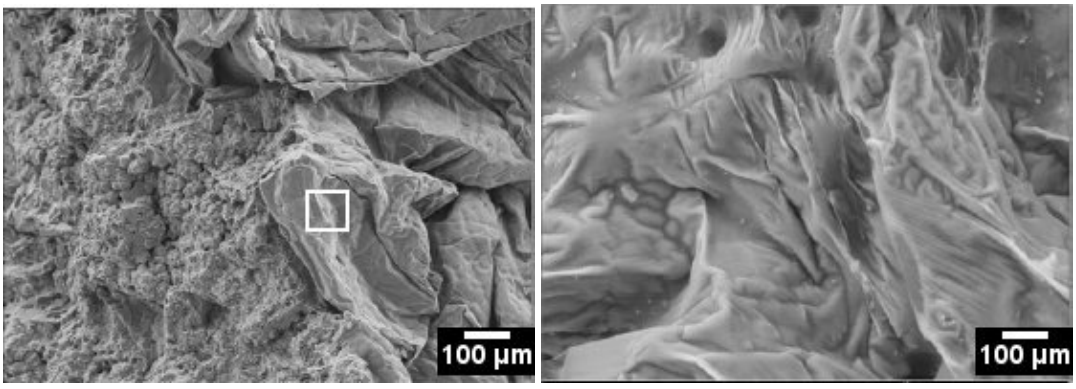

Figure 2-10 SEM image of interface region between oxide film and matrix on fracture surface of AZ91 tensile specimen.

The deleterious impact of the presence of entrained oxide films in magnesium melts has been demonstrated [Griffiths and Lai, 2007] to cause a spread in the mechanical properties and to cause a larger reduction in the elongation to failure than the ultimate tensile strength. This is a trend that is observed in aluminium alloys and has now been shown to be true for magnesium alloys.

As discussed above the formation of a stable oxide film is necessary during any form of processing since the melt will be subjected to transferring and exposed to

air at some point. Campbell identifies that oxides and entrained films are known to be of all shapes and sizes constituting by far the largest defects in a casting. Thus it is most desirable to prevent the entrainment of oxide films if possible and to design the casting process and equipment to overcome this. Several approaches have been proposed such as those which describe how magnesium alloys can be poured as close the mould as possible and from a fixed position. This protects the oxide pipe which forms around the stream ensuring it remains unbroken, preventing further oxidation and avoiding oxide entrainment [Campbell, 1993]. A more common technique is the Cosworth casting technique initially designed for aluminium castings but now applied to magnesium, reducing porosity and inclusion levels in shape castings. In this process the melt is electromagnetically pumped into the mould, filling the mould from the bottom. The pump is submerged in the liquid metal and moves it into the mould without any moving parts. The result is a cleaner casting free from entrained oxide films caused during casting.

2.2 Production of Wrought Magnesium Alloys

Large scale production of magnesium alloys typically starts with the production of billets by the Direct-Chill (DC) casting process. Semi-continuous vertical DC casting is the method used to produce all the materials investigated in this study. The quality of the final product is very dependent on the casting parameters used during production. This section introduces the DC casting process and the typical product of this method. A review of the literature relevant to this process is included which also covers the recent developments and alternative techniques to produce high quality castings.

2.2.1 DC Casting

The first stage of producing the majority of wrought products usually involved the production of cast material by DC casting. The most uniform and desirable microstructures, that is one which has minimal segregation, smallest grain size and little porosity, are achieved by the DC semi-continuous casting process. This method is used to cast feedstock for wrought processing such as forging, rolling and extrusion. Forging and high-pressure die-casting are the two most common production methods of magnesium alloy engineering components [Polmear, 1996] yet growth of the forging market depends on high quality feedstock. The DC casting process can be adapted to produce feedstock for forging by using a round mould or for rolling by using a rectangular mould to produce slab.

Alloys are prepared by melting master alloys, concentrated hardeners or recycled material to meet the desired composition. Suitable fluxes and cover gasses must also be used during preparation of the alloy which from a protective layer on the surface preventing the liquid metal from reacting with the oxygen in the air for the reasons presented in section 2.1.9. Degassing and filtering is also employed to remove any oxides and non-metallic inclusions in the melt prior to or during transfer to the mould.

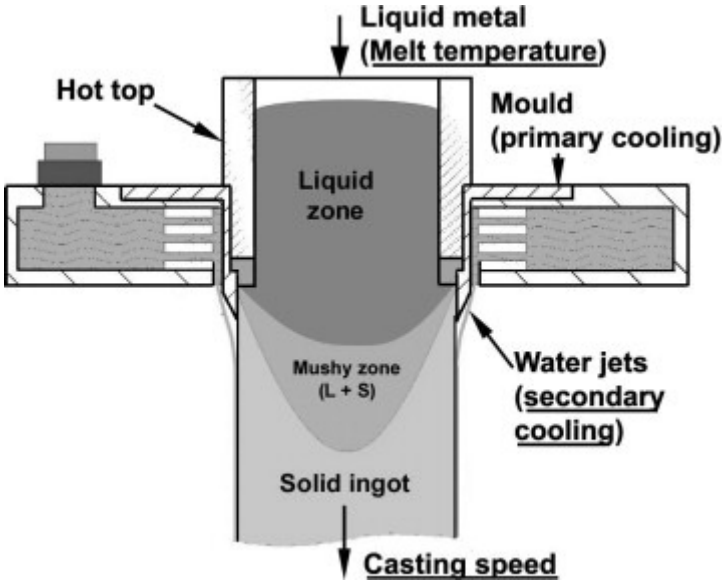

Figure 2-11 Schematic of DC casting arrangement (Hot Top configuration also shown). [Nadella et al., 2008].

The DC casting technique involves introducing the prepared melt into a water-cooled metal mould, having a retractable base, as in Fig. 2-11. The molten alloy is typically transferred from the crucible by the use of a launder [Zuidema and Katgerman, 2006] and then introduced into the mould by a submerged entry nozzle or equivalent inlet pipe, however other systems are available. The solidification of the molten metal is completed in two stages: first the solidification of the metal at the cooled mould wall followed by solidification of the remainder of the billet content. Complete solidification is aided by a cooling water spray as the metal emerges from the bottom of the mould. The limiting speed at which continuous casting can be completed is the time taken for a solid skin to form which can contain the remaining liquid melt after it has emerged from the base of the mould [Chalmers, 1964].

The most common method of DC casting is carried out using an aluminium water jacket or copper moulds which are continuously sprayed with cold water directed at the outside of the mould walls to achieve the necessary primary cooling. Additional secondary cooling is also required and this is achieved by a lower ring that sprays cold water at the metal as it emerges and runs down the billet surface, shown in Fig. 2-11.

A critical region in the casting arrangement is the melt delivery from the crucible to the mould. The transfer equipment used to achieve this commonly contains a form of filtering which acts to remove any inclusions in the melt prior to it entering the mould and can also be used to condition the flow. At this point it is important to limit turbulence and to prevent the entrainment of any further inclusions [Zuidema and Katgerman, 2002] and to control the flow rate of melt into the mould. Several different techniques are available to achieve the molten alloy transfer from the crucible to the mould, with various levels of sophistication.

The simplest technique is to use a launder, which is typically an open U-channel constructed of steel, which carries the melt to the mould and controls the flow rates by a valve like control pin at the top of the inlet pipe, at the base of which there is the submerged entry nozzle. As shown in Fig. 2-12, it is common for jetting to occur as the melt exits the submerged entry nozzle of the transfer equipment which can initiate complex recirculating flow patterns which directly impact on the final microstructure and defect content level in the final cast product [Eskin et al., 2004]. The open channel launder is a low cost solution to melt transfer however provides poor control over the melt flow and can result in poor quality castings.

Siphoning offers an alternative melt transfer system, similar to another option of electromagnetic pumping. These two options are commonplace in the aluminium industry and provide more flexibility on foundry layout and generally reduced defect content in the cast material [Fisher, 1978]. These melt transfer systems are also commonly combined with some form of filtering. A more detailed discussion on filtering and melt transfer methods is presented in sections 2.2.5.2 and 2.2.5.3 respectively.

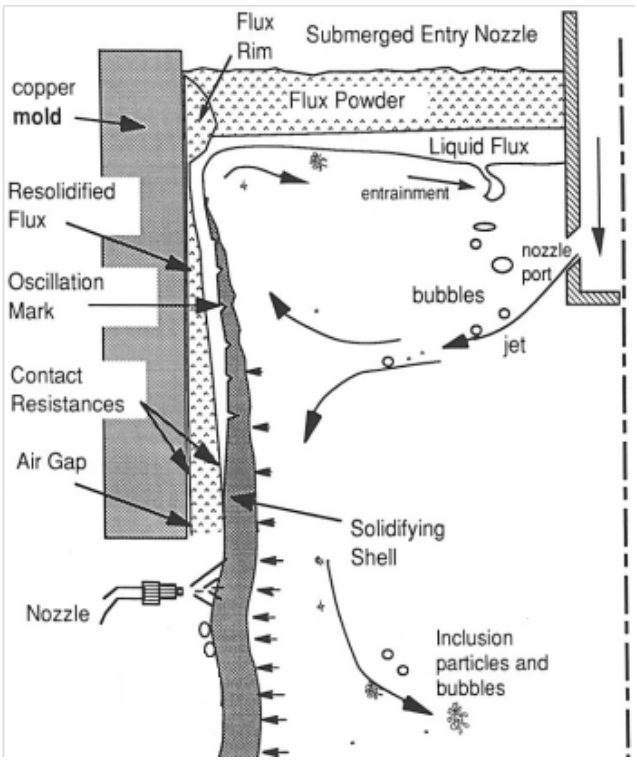

Figure 2-12 Adapted schematic of DC casting mould region. Molten metal is fed into the melt pool via the entry nozzle [Thomas, 2001].

The majority of casting quality problems including inclusion entrainment are directly associated with the in mould flow [Zhang, 2006] which is initiated by the flow in the transfer and delivery system upstream. Modelling of these stages of the casting process has been completed in previous studies [Szekey et al., 1972; Thomas et al. 2001; Eskin and Katgerman, 2009] in attempt to identify the best practice to producing high quality castings. The velocity of the molten metal is an important factor however, the resulting flow pattern can be even more critical to the production of clean material. Many studies have been carried out using numerical modelling techniques to predict and understand the fluid flow involved in DC casting [Matys, 1985]. There have also been attempts to monitor the flow in aluminium melts during casting using electromagnetic sensors [Ricou and Vives, 1984], however this has proven to be very difficult and unreliable, an alternative approach using magnetic probes has also been trialled [Weissenfluh, 1985]. A different approach is to use physical models to simulate the fluid flow involved in the DC casting process, especially the sump region. These models involve water being used to simulate the molten alloy and transparent plastic mock casting

equipment so that flow regimes may be observed, often highlighted by the use of coloured die or added trace particles [Szekey et al., 2008; Campbell et al., 2001]. Direct interpretation and translation of the flows observed in these models to the molten alloy arrangement is not possible however as they fail to consider the important effects of convection and heat transfer and solidification. Thus computer modelling is often the most reliable and successful method.

"Hot Top" DC casting is a development on conventional DC casting involving very similar equipment and arrangement. The system differs from the conventional casting by not requiring a submerged entry nozzle and flow control valve to regulate the entry of molten alloy into the mould. The transfer launder is flooded and the melt enters the mould through a wide channel that is not restricted, Fig. 2-13. All this occurs under the melt surface, which possess an oxide film that is not disturbed, thus this process benefits from much lower entrained oxide films, inclusions and other associated defects.

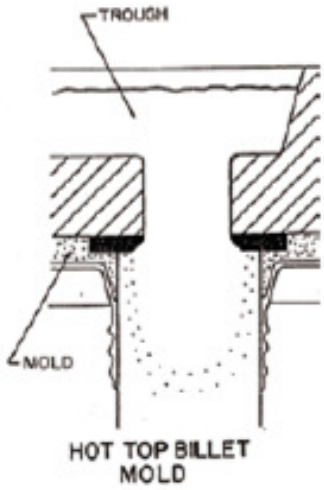

Figure 2-13 Comparison of conventional DC casting equipment arrangement and Hot Top Billet DC casting arrangement [Pyrotek magazine].

Another alternative arrangement to achieve cleaner castings and reduce manufacturing waste is to use an electromagnetic mould [Fisher, 1978]. During casting if the initial cooling is too high in the mould, molten metal will flow over the rapidly solidified metal and form surface folding defects. The presence of folding

defects requires that the surface of the cast billet is removed prior to further processing; this is achieved by machining or scalping. The problem of a skin forming on the billet can be avoided by using electromagnetic casting technique whereby the molten metal is repelled by the mould walls, thus the only heat transfer is through the base of the mould and secondary cooling by water sprays onto the emerging billet as with the traditional method. This technique is reported to result in a smoother billet surface, a reduction in waste and studies also suggest a finer and more uniform microstructure [Polmear, 1996].

The magnetic field can be expanded to be used as a brake for the incoming molten alloy. This has the effect of reducing any high speed jetting which may occur, which as discussed can be detrimental to the casting quality, by separating the incoming molten flow into separate strands. The reported results also included are a more even distribution of particles and inclusions in the final cast microstructure [Kolberg, 1985].

2.2.2 Cast Microstructure

The typical microstructure resulting from casting is one that contains three distinct regions; the chill zone, the columnar zone and the equiaxed zone, as in Fig. 2-14. This is true for the Mg-Al system which typically contains large and variable sized grains. It is therefore important that some form of grain refiner is used when casting Mg-Al alloys, this is discussed in section 2.1.4 [Polmear, 1996].

The first region of the cast microstructure to form consists of very fine equiaxed grains at the billet surface, formed very quickly as the molten alloy comes into contact with the cooled copper mould. This section is known as the mould chill zone (MCZ). The neighbouring region consist of columnar grains which have grown parallel to the heat flow, which is significantly reduced as the billet contracts and creates an air gap between the billet surface and the mould. The final region to solidify is the centre of the billet which forms larger equiaxed grains.

In DC casting there is often an observed reduction in the grain size at the billet centre and this is also thought to be associated with a region of inverse segregation [Eskin et al., 2004] also reported to occur during DC casting of aluminium alloys [Nadella et al., 2008]. Current theories suggest this is achieved by free-floating dendrites which act as nucleation sites for new grains and disrupts the columnar grain growth [Vreeman and Incropera, 2000]. Free-floating dendrites are fragments that are caught up in the currents in the liquid sump and circulated with the fluid flow. The floating dendrite pieces commonly settle at the centre of the billet and this is where they nucleate new grains and continue to grow themselves. The effect of the free-floating dendrites on the traditional three zone casting microstructure is an expansion of the equiaxed zone and as a result reduced columnar region and reduced segregation from the billet centre [Vreeman and Incropera, 2000].

The growth of large grains is undesirable in cast alloy microstructures, this typically occurs without the presence of any form of grain refiner. The advantages of having smaller grains are recognised both in terms of the material's improved mechanical properties and practicality; improved resistance to hot tearing, reduced scattering of X-rays and ultrasonic waves (important during inspection), improved resistance to grain boundary corrosion and also higher yield strengths, toughness and fatigue resistance [Campbell, 1993]. The addition of zirconium as a grain refining alloying element has a notable impact on the grain size and therefore on the strength of the material and the resulting toughness. Grain refining of the Mg-Al system is achieved by alternative means to the addition of zirconium, either by superheating or by carbon inoculation. The reasons for this are explained in section 2.1.3.4.

The flow of molten fluid in a mould is very important when attempting to produce high quality castings. During DC casting into a circular mould the molten alloy is fed into the mould by a central inlet, usually a submerged entry nozzle, and a distinct flow pattern occurs in the molten sump. This flow pattern is thought to directly influence the defects present, the location of the defects, segregation and the resulting grain size distribution [Zhang, 2009]. Modification of the submerged entry nozzle can offers an easy and inexpensive route to improved casting quality.

The flow in the mould is initiated by the falling stream of molten alloy which is directed to the edges of the mould by a distributor plate or similar in a submerged entry nozzle at the base of the inlet pipe. This provides the edge with a continuous supply of molten alloy and creates a circulating flow of alloy in the mould. These flow patterns have been reported in continuous casting and semi-continuous DC casting processes [Thomas and Zhang, 2001, Zhang, 2009] and were also observed in the simulations carried out as part of this study. The flow within the molten sump in the mould is responsible for the transportation of the free-floating dendrites and can also explain the differing microstructural features present within the same location of a billet.

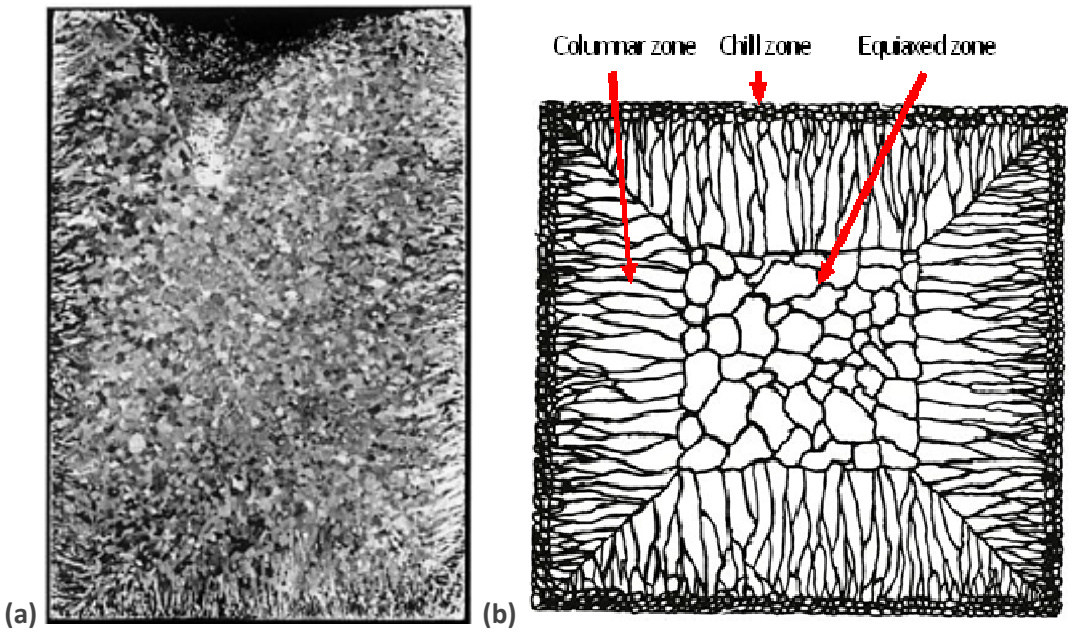

Figure 2-14 (a) Macrograph of Mg-1Al casting [Dahle et al., 2001] (b) Schematic of cast structure demonstrating the three distinct regions of grain growth: chill zone, columnar zone and equiaxed zone [Flemings, 1974].

The microstructure of the casting can also be modified by controlling the cooling rate, the amount of alloying additions and grain refinement. The cooling rate impacts on the size, shape and volume of second phases and intermetallic particles present [Grandfield and McGlade, 1999]. The cooling rate during DC casting is typically under 5°C/s in the central region and around 15°C/s at the billet surface [Eskin et al., 2004]. The cooling rate can be increased slightly by increasing the

casting speed, increasing the casting temperature or reducing the metal level in the mould [Larouche and Brochu 1996].

The cast microstructure almost always contains a second phase and a level of inclusions. Those present in AZ80 alloy are discussed fully in section 2.2.3. These inhomogeneities in the microstructure are often encouraged to form, as a reinforcing phase, or attempts made to limit their presence as desired.

2.2.3 Casting Defects

2.2.3.1 Inclusions and Second Phases

Anything contained within the cast billet that is not continuous with the structure will impact on the properties of the material and if not added deliberately will therefore be considered a defect. Defects occur as individual discontinuities, however grouping or clustering of defects is also observed and must be taken into consideration when studying defect content, since a cluster of small defects can be as harmful as a single large defect. The main defect types present in castings are compact defects and planar defects which are differentiated on the basis of shape. Planar defects are significantly more damaging to the materials properties due to their shape.

The most important type of compact defect is inclusions; an inclusion has been defined as any undissolved foreign material [Kaye and Street, 1982]. Non-metallic inclusions are one of the most detrimental defects found in castings as they act as stress-raisers, reduce corrosion resistance and increase porosity [Makarov et al. 1999].

Inclusions are typically formed or entrained in the melt during the casting process. These can often be the product of a reaction with the mould walls or oxide and flux inclusions; flux is necessary to reduce the amount of air flowing with the molten metal by removing it, and is essential when casting magnesium alloys. The

formation of inclusions is also highly probable if deoxidizers or grain refiners are added to the melt.

Intermetallic and second phases can form in regions between the growing primary phase dendrites which contain liquid that is rich in solute and these are also classed as inclusions. Intermetallic phase inclusions are also found to form in the region of negative segregation (in the centre of the billet) where the solute rich liquid provides sufficient amount of solute atoms for the second phase to grow.

Second phases can also take the form of a eutectic however the second phase present in this form are relatively small compared to intermetallic phase inclusions and can often be removed by homogenisation or thermo-mechanical treatment. The homogenisation process effectively dissolves the second phases present and on controlled cooling limits the formation of the undesirable phase, often even this type of processing will not remove intermetallic inclusions.

The majority of casting defects, including second phases, can be removed during further processing such as homogenisation or thermo-mechanical processing yet some of the initial DC cast structure is found to remain [Chaijaruwanich et al., 2007]. Entrained inclusions and intermetallic phases typically cannot be removed by post production processing due to their extremely high melting point.

2.2.3.2 Entrainment of Oxide Films

Entrainment defects are one of the most commonly observed planar defects in all cast materials and are particularly prevalent in magnesium alloy castings. Entrained oxides can be present in melts if they already exist in the stock material or due to moisture on the surface of master alloys prior to melting. During transfer or pouring the liquid metal is often subject to turbulence which can lead to entrainment of surface oxide films, gas or other debris present on the surface, as shown in Fig. 2-15.

During transfer or pouring, the oxide skin may be broken or folded over, which will trap a small volume of air or debris between the two surfaces, Fig. 2-16. Once entrained the folded oxide film will act as a crack in the final casting and is referred to as a double oxide film defect [Cao and Campbell 2000]. The presence of entrained defects can reduce the leak-tightness of components and increase the distribution of mechanical properties, neither a desirable characteristic.

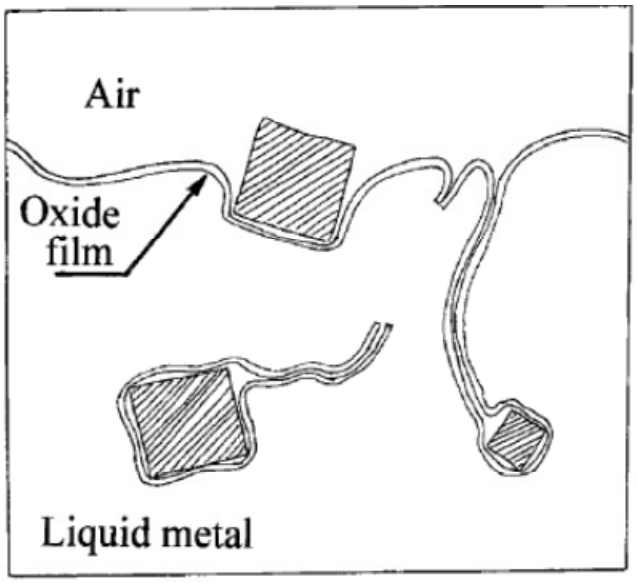

Figure 2-15 Schematic of the entrainment of surface oxide films, debris and gas [Campbell, 2006].

The mechanisms by which a surface oxide skin may become entrained are many, but by far the most common is surface turbulence, at which point the film is incorporated into the melt by a breaking wave on the surface, Fig 2-16. The cause of surface turbulence is often due to poorly designed gating systems or high molten metal velocities during pouring. Any disturbances during the handling of the molten alloy can cause an expansion or contraction of the free surface, which the oxide film cannot accommodate, resulting in folding, fracturing and entrainment of the film.

Other mechanisms of entrainment are due to surface flooding, the result of which may be a confluence weld when two molten metal surfaces meet within the casting

mould resulting in the loss of the free surface trapping the film which existed on both previous free surfaces [Cao and Campbell 2000; Campbell, 1993].

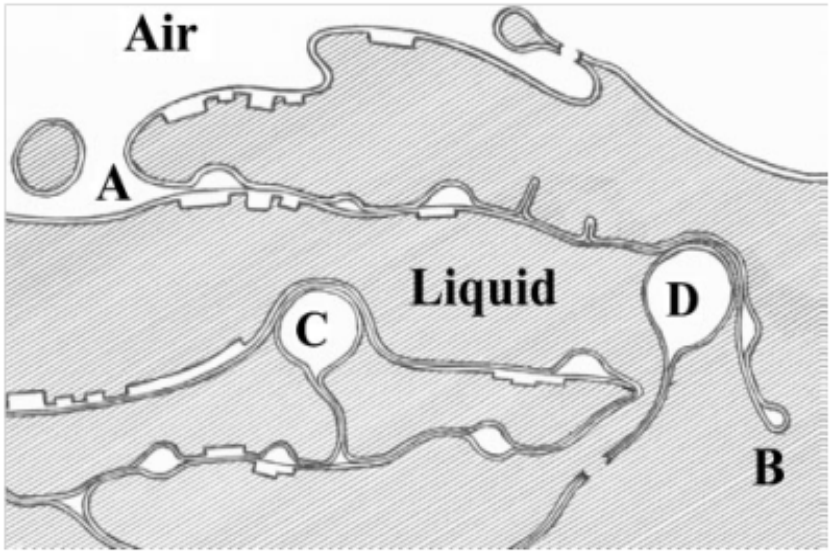

Figure 2-16 Schematic of surface turbulence causing the entrainment of surface oxide skins and creating pores [Campbell, 2006].

For continuous or semi continuous casting processes controlling the transfer of the melt into the mould is most critical. The velocity of the melt during transfer, pouring and flow patterns in the mould are the most common causes of entrainment and limiting these during pouring are essential to produce clean castings.

During pouring an initial oxide film will grow around the falling stream and with increasing height of pouring, it is likely oxide films detach and become entrained along with air as in Fig. 2-17 [Campbell, 2003]. The entrainment of air can result in a large bubble trail defect, a long bifilm left in the trail of a gas bubble rising through the molten alloy [Campbell, 2011]. In order to reduce this effect it is important to pour from as low a position as possible and maintain a constant flow where possible.

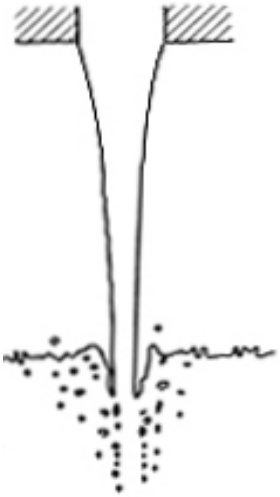

Figure 2-17 Oxide film and air becoming entrained during pouring of a melt from a large height [Campbell, 2003].

The presence of any oxide films in the final cast material can be hard to detect using NDT techniques and can therefore result in a high variability in the castings final mechanical properties. Entrained oxide films can be very large, on the scale of millimetres Fig. 2-18, and are often associated with other defects such as porosity and cracks, resulting in a reduction in the mechanical properties [Wang et al. 2001] however defect of this type and size are more reliably detected by NDT techniques. Entrained films are also frequently broken up and results in a large number of small film fragments which are extremely hard to detect using NDT techniques, contributing to the variability in the mechanical properties.

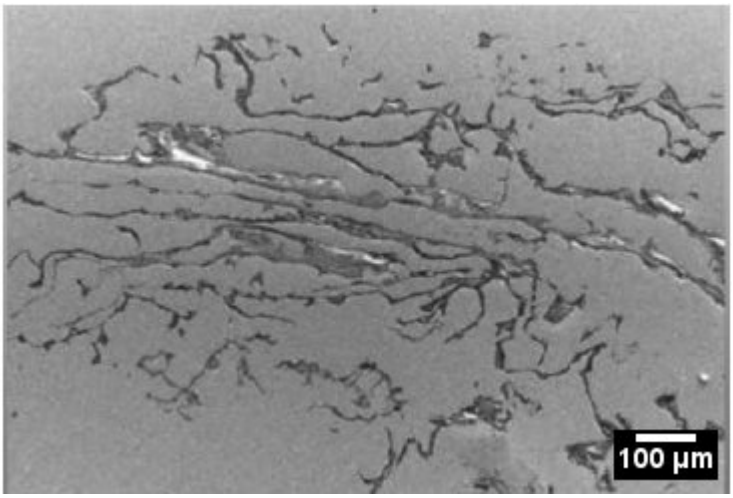

Figure 2-18 Tangled bifilm observed on polished surface [Campbell, 2006].

Entrained oxide films are frequently favoured as nucleation sires for intermetallic phases in aluminium alloys [El-Sayed et al., 2011; Cao and Campbell, 2005; Campbell, 2006]. As an approach to high quality castings this mechanism is suggested to be utilised for the deliberate nucleation of an intermetallic phase on entrained oxide films which will promote the settling of the films and improve the cleanliness of aluminium alloys. Entrained films that are associated with second phase and intermetallic particles [El-Sayed et al., 2011; Campbell, 2006] can also result in large defects which are significantly easier to detect by NDT methods.

2.2.3.3 Porosity

Porosity is reported to be one of the most common defect types found in castings. Porosity defects may form as the result of many mechanisms; large freezing range of an alloy, incomplete feeding, reduced solubility of hydrogen on cooling, gas entrainment, association with oxides and shrinkage are all identified as the main causes [Monroe, 2005]. Porosity cannot always be removed by post production treatments such as homogenisation or thermo-mechanical processes. It is for this reason that forgings and machined parts are often favoured over cast components.

For light alloys such as aluminium and magnesium alloys, especially AZ91 alloy, microporosity is a persistent defect which is difficult to remove [Wang, 2009]. Microporosity is reported to be present in almost all cast aluminium alloy products [Lee et al., 2002] and the same abundance is expected to be true for magnesium alloy castings. The distribution of porosity across DC cast aluminium billet is reported to both coarsen and increase in area fraction towards the centre of a billet. For a typical billet the pores were determined to be 4 μm at the billet surface increasing to 6 μm at the centre [Eskin et al., 2004; Nagaumi, 2001] representing a significant defect in the microstructure. The distinction between micro- and macro-porosity can be made by classifying pores less than a dendritic cell size, e.g. 100 μm as microporosity, and those larger than 100 μm as macroporosity [Caceres, 1995].

The occurrence of insufficient feeding can result in shrinkage porosity. Solidification of an alloy is associated with a decrease in volume which is usually

accommodated by any remaining fluid flowing in to fill the volume. As solidification proceeds the remaining feeding channels, within the interdendritic network, reduce in size and eventually freeze, ceasing to supply the required liquid to accommodate the shrinkage. As a direct result, the shrinkage causes tension and voids form to relieve this tension [Lee et al., 2001]. This type of porosity is observed as interconnected or clustered and is of an irregular morphology, typically taking up the shape of the interdendritic region [Sabau and Viswanathan, 2002].

Different eutectic growth modes are suggested to impact on the formation of shrinkage porosity in magnesium alloys, where liquid is required to be drawn through the dendritic network. The pore size and percentage porosity is reported to increase with increased solidification time [Dahle et al., 2001].

Gas porosity is typically rounded, isolated and well distributed, caused by the dissolution of hydrogen gas on cooling [Sabau and Viswanathan, 2002]. Pores ranging in size from 25 μm up to 100 μm have been reported in cast aluminium alloys, with percentage porosity ranging from 0.1% up to 0.5% in the centre of an as-cast Al-Mg billet [Lee et al., 2002].

Gas porosity and shrinkage porosity have been observed to be present in DC cast Al-Mg alloy as small round pores (<5 μm) associated with much larger pores which create complex networks [Chaijaruwanich et al., 2007]. Both optical and SEM micrographs along with an X-ray micro-tomography image are shown in Fig. 2-19 of the resulting pores observed in an as-cast Al-6Mg alloy [Chaijaruwanich et al., 2007]. The volume of porosity was found to increase with magnesium content which is thought to be due to increased levels of interdendritic liquid and increased hydrogen pick up. Similar features are likely in DC cast magnesium alloys, although these have received much less study.

Porosity is also found associated with entrained oxide films, as mentioned earlier [Monroe, 2005; Campbell, 2006; Wang et al., 2009]. This type of porosity can be significantly more damaging than gas porosity due to its morphology, it is often very

narrow and faceted acting as potent stress concentrator. Any porosity due to the entrainment of gas will have an associated oxide film, as discussed in section 2.1.9.

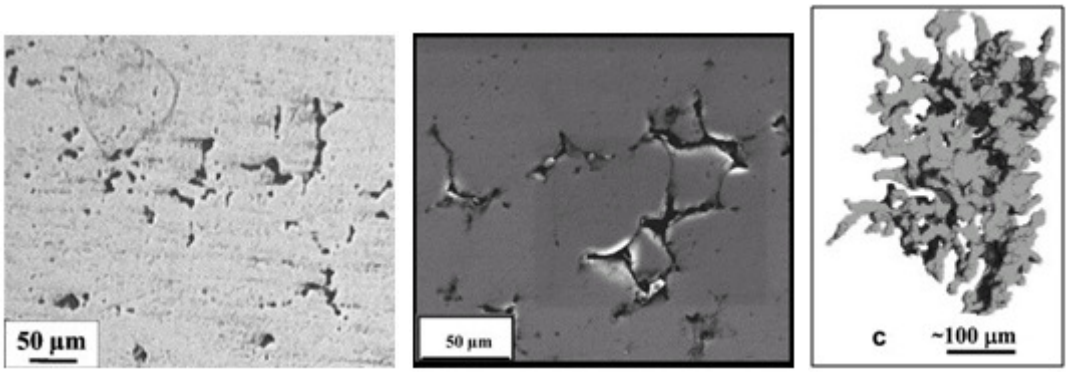

Figure 2-19 Observed typical pore morphology due to insufficient feeding and shrinkage in aluminium alloy Al-6Mg alloy in the as-cast condition [Chaijaruwanich et al., 2007].

2.2.3.4 Hot Cracking

Hot tearing and cracking is another type of casting defect, and is the combined result of inadequate liquid feeding and tensile stresses generated by shrinkage of the alloy on solidification [Li et al., 2010]. The occurrence of this type of defect is affected by the alloy composition, amount of liquid present during solidification, the ability of the solid present to resist the stresses generated on solidification and the casting geometry.

The formation of a hot tear involves the pulling apart of dendrites formed early during solidification to form a crack that is usually filled with eutectic-rich solid to prevent a defect forming; this can often result in segregation in the resulting microstructure. If there is no liquid available to fill the newly created crack then a defect remains, Fig. 2-20. This differs from porosity which occurs solely due to limited feeding of molten liquid and creates pores surrounding the dendrites, hot tearing also involves the movement of the dendrites. The resulting defect can often not be removed by homogenisation or thermo-mechanical processes.

It is possible for the whole casting to fracture if the internal stresses are greater than the yield strength of the semi-solid metal at any time during cooling [Flemings,

1974]. The resistance of an alloy to hot tearing can be improved by grain refinement [Li et al. 2010]. The smaller and more equiaxed grains improve feeding due to their geometry and delay the point at which the mush begins to behave like a solid. As a result a smaller grain size is better at resisting hot tearing as it is weaker during solidification and can accommodate stresses by movement of both solid and liquid.

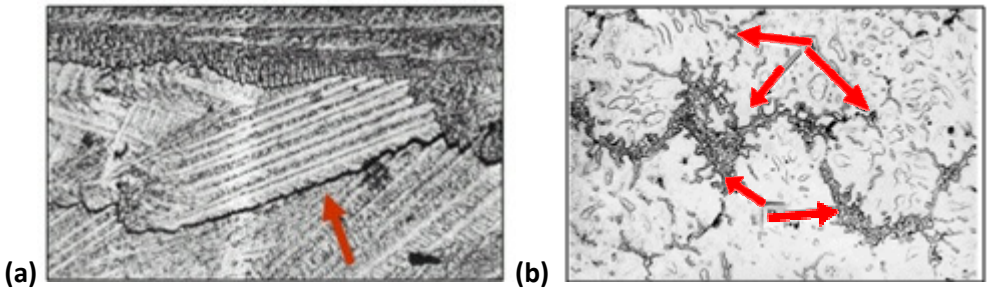

Figure 2-20 Hot tearing in (a) a polycrystalline metal indicated by red arrow and (b) indicated by A and B in AZ91 alloy [Wang et al., 2002].

2.2.3.5 Clustering

The presence of inclusions and second phases in the melt at temperatures above the solidus has a number of detrimental effects on the castability and final mechanical properties of the material. These inclusions often accumulate in the remaining liquid and as a result effectively form a single larger defect or a cluster in the final cast product. The explanation for the clustering is a matter of debate but has been the focus of numerous studies involved in the production of metal matrix composites (MMC) [Watson et al., 2005; Kennedy and Wyatt, 2000; Feng and Froyen, 2000; Stefanescu et al., 1991] and will be discussed in this section as they are pertinent to the defects found in this study.

Previously, particles and inclusions present within dendrites were previously thought to be primary inclusions and those in the interdendritic regions were formed later during solidification. It is now recognised that this is not an accurate description and that particles may be pushed by the growing dendrites during all stages of solidification [Flemings, 1974], some are engulfed by the dendrites during

growth while others are not. This realisation opens the discussion up to identify possible mechanisms resulting in the clustering of inclusions during casting.

Clustering can occur due to the interaction between particles in the melt, this may be due to settling, agglomeration or the result of convection currents which direct particles towards the same region of the casting. Once in contact, the driving force for agglomeration is a small reduction in overall interfacial energy [Vugt and Froyen, 2000]. Agglomeration will occur if it leads to a reduction in interfacial energy; that is the wetting between the liquid alloy and the particle is poor and the particles will then adhere. Inversely if the wetting between the particle and the matrix is good, a layer of liquid will remain and prevent adhesion between particles.

Clustering has also been described in terms of collisions of particles resulting in sintering. The collisions occur due to the same processes as described by Vugt and Froyen, such as convection and floatation/sedimentation bringing particles into close proximity. Coarsening may occur after particles collide and sinter, explaining the very rapid growth of the newly created particle, which is known to occur in steel and other alloy systems. However, it was observed that the rate of coarsening is actually very small. The rapid increase in size of the particles is mainly due to the sintering process alone which results in large interconnected clusters that may consist of hundreds or more individual particles.

Particle pushing leading to clustering is most commonly discussed in the context of MMCs [Youssef et al., 2005; Lloyd et al., 1989; Rohatgi and Asthana, 2001] but are equally applicable to alloy systems which exhibit either early nucleation and growth of a second phase or those castings which possess high inclusion levels. These theories aim to form a reliable model which explains the pushing of solid phases present in the melt into the remaining liquid during solidification ultimately directing a number of these particles into clusters.

Previous studies [Feng and Froyen, 2000; Watson et al., 2005] discuss the particle pushing theory in terms of a critical velocity of the solidification front of the primary

phase which either pushes the particles ahead of it or engulfs it. The engulfing of a particle occurs when the velocity of the solidification front is above a critical velocity at which point the grain will grow around the particle or inclusion. The critical velocity mentioned is a function of the particle or inclusion size and the temperature gradient at the solidification front [Feng and Froyen., 2000]. In general the models consider the conditions necessary and the critical velocity for particle pushing or particle engulfing. The models mainly differ on the sophistication of the mathematics and boundary conditions of the solidifying front but all similarly describe the interaction by balancing the forces which repel and attract the particle to the interface [Asthana and Tewari, 1993].

As well as particle pushing, clustering can be attributed to settling. Sedimentation of particles and inclusions significantly denser than the liquid alloy will occur, as discussed previously. Settling calculations have been carried out for inclusions in both magnesium and aluminium alloys [Qian et al., 2001; Cao and Campbell, 2004; Cao et al., 2004]. The studies used Stokes Law to predict the settling times and velocities for various particle and defect types with good agreement with experimental observations. A settling period is usually incorporated into the melt preparation stage to effectively clean melts before casting. However, if the cooling conditions are controlled to result in dendrite spacing smaller than the particle size, clustering may not occur and the resultant particle distribution will be similar to prior solidification producing a relatively clean casting.

An alternative approach to clustering, and most applicable to this study, which suggests the formation process for defects consisting of entrained oxide films and particles is 'trawling' of the oxide film. This 'trawling' mechanism produces clusters of particles without pushing by the solidification front. The results of a study [Kennedy and Wyatt, 2000] to investigate the impact on mechanical properties of producing MMCs by powder processing or melting the powder and casting, demonstrated that the casting production method resulted in significantly in a reduction in both strength and ductility. The cause was suggested to be due to the oxide present on the individual particle surfaces, which when melted become

mobile and proceed to 'trawl' the particles into clusters [Kennedy and Wyatt, 2000]. The presence of such oxide films are not present in traditionally prepared casting melts but the concept of mobile oxide films 'trawling' any inhomogeneities present in the melt into clusters is one that is transferable to many casting methods.

2.2.4 Alternative Production Techniques

As mentioned previously castings can suffer from a large range of defects which have a deleterious effect on the mechanical properties of the material produced. Alternative production techniques of forging and casting feedstock have been developed in an attempt to eliminate defects.

2.2.4.1 Melt Conditioning

The melt conditioned direct chill (MC-DC) casting process is a novel development of the DC casting process designed to produce high quality billet and slabs by employing the melt conditioned by advanced shear technology (MCAST) machine, Fig. 2-21(a), in combination with a traditional DC caster [Haghayeghi et al., 2008]. This process can produce magnesium alloy billets with fine and uniform microstructure, uniform chemical compositions and reduced cast defects, such as porosity and cracks. The MCAST machine consists of a pair of co-rotating, fully intermeshing screws designed to achieve high shear rates and turbulence in the melt which is then continuously fed into a traditional DC casting mould. The results of this technique demonstrate that the typical three zone cast structure is eliminated and a fine equiaxed grain structure is achieved across the billet section [Haghayeghi et al., 2008]. This is achieved by an increase in the effective nucleation rate, breaking-up the existing oxide particles in the melt such that they will act as heterogeneous nucleation sites [Fan et al., 2009; Men et al., 2010].

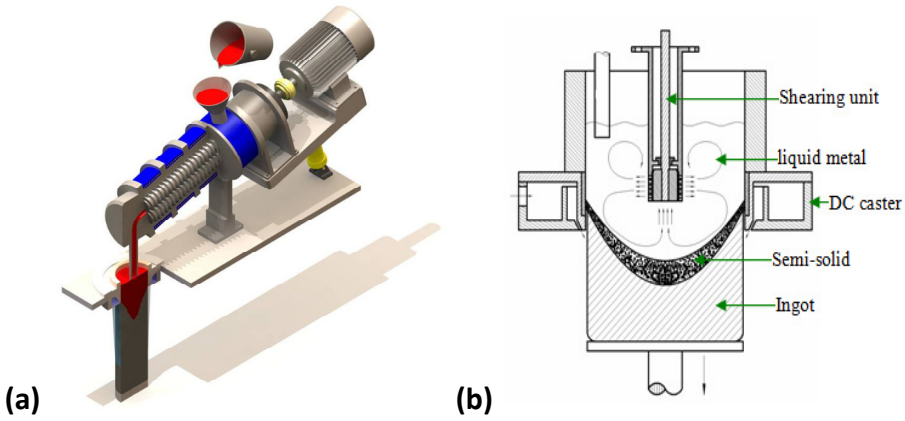

Figure 2-21 Schematic of MC-DC casting processes. Melt conditioning achieved by (a) MCAST [Haghayeghi et al., 2008], (b) Stator-rotor arrangements [Zuo et al., 2011].

Melt conditioning can also be achieved by the use of a high shear rate stator-rotor arrangement placed within the mould of the DC casting equipment, Fig. 2-21(b) [Zuo et al., 2011]. This technique provides the same benefits as the MCAST and by the same mechanisms, however it also provides the additional benefit of creating a macro flow within the melt contributing to the benefits experienced.

2.2.4.2 Twin Roll Casting

An alternative method of producing wrought magnesium alloys is by the twin roll casting (TRC) technique or strip casting. Strip casting is still a very new development and is advantageous as it offers a one-step process for the production of flat rolled products [Park, 2004]. The advantage of TRC over traditional route is the time and energy saved, as it is no longer necessary to heat the DC cast slab or billet to enable rolling and subsequent passes through the rolling mill. The conventional route of sheet production is very complex due to the limited deformability of magnesium alloys. To overcome this, the TRC technique involves the injection of molten alloy from a nozzle located at the entrance of the rolling mill which contains cooled rollers. As the molten alloy enters the rollers it solidifies and is immediately rolled. The sheet alloy produced by this procedure is reported to have comparable tensile properties to the conventional ingot produced sheet. This is thought to be due to the fine dispersion of intermetallic phase particles in the microstructure [Park, 2004].

The melt-conditioned process can also be applied to twin roll casting process (MC-TRC). This process is suggested to result in magnesium alloy sheet with a uniform equiaxed grain structure and reduced segregation [Bian et al., 2009].

2.2.5 Approaches to Clean Castings

The DC casting method can be used to produce high quality wrought alloy feedstock, however consideration must be given to the individual processes used to achieve this. Techniques, commonly used in the aluminium industry are available and should be considered by the magnesium industry, such as those to monitor and minimise the amount of inclusions which pass into the final product. This section will review the techniques and technology that can be adopted to improve quality.

2.2.5.1 Settling

Inclusions present in alloy melts almost always possess a different density to the molten alloy and this can be utilised for a process of removal. Preparation of the melt usually allows for settling or floatation of the inclusions which occurs naturally due to the contrasting densities.

In the case of aluminium alloys the oxide film is more dense than the molten alloy and thus would be expected to sink, however the trapped air associated with the entrained film will result in the inclusion possessing neutral buoyancy. In this case, filtering or some form of removal is necessary [Campbell, 2006]. The oxide film in a magnesium melt is less dense than the melt and the ever present air will ensure the film floats to the surface, however castings are still found to contain oxides.

A novel approach to remove an entrained film or iron rich phase from aluminium alloy was studied [Cao and Campbell, 2003]. The results of this study showed that the heat treatment of the melt, stimulated the precipitation and sedimentation of intermetallic compounds from the melt, which grew on the entrained oxide film. The oxide film was then expected to sink under the weight of the newly precipitated particles, resulting in a cleaner casting. Applying this same theory to

producing magnesium alloy castings could be utilised in the reliable production of cleaner casting.

An assessment of holding time, same practice as a settling time, was assessed on aluminium alloys [El-Sayed et al., 2011] and shown that an increase in the Weibull modulus was observed after 20 minutes yet this decreased for a duration longer than this. It was suggested that the oxide films were broken up in this initial period and the internal environment, in this case air, was consumed. However after this time gas evolution was suspected to lead to porosity, hence a settling or holding time must be fully assessed and a longer holding time is not always better in the attempt to produce high quality castings.

2.2.5.2 Filtering

In general many lessons from casting practices of other metals such as aluminium and steel can be applied to magnesium, this is especial true for filtering. Ceramic filters are commonly used in the aluminium industry and have been identified to be very effective with magnesium alloys [Bakke et al., 1994].

The two most commonly used filter types used in the casting industry are either metal mesh (or foam) and ceramic foam (or bonded particle). Cartridge filters are an alternative solution, which is a separate unit operating in a similar way to heat exchangers, however are typically very expensive and require substantial changes to the casting equipment for them to be accommodated. They employ the same filter types and only have the advantage of larger surface area which can accommodate higher flow rates through a finer grade filter.

Filters operate based on two modes, depth filtration and cake filtration. Cake filtration relies on the build-up of inclusions on the filter surface which contribute towards the filter effectiveness, compared to depth filtration which operates by collecting the inclusions within the filter. Ceramic foam filters actually have three distinct operating phases, initially a priming period, common with all filters, followed by depth filtration and then cake filtration. These stages correspond to a

change in the flow rate through the filter which is shown to be almost constant during the depth filtration stage and then begins to decrease at the transition to cake filtration mode.

The pressure required to prime a filter is an essential consideration on selecting a suitable filter. Cartridge filters require a larger metallographic head to prime than others, which is often not available for DC casting arrangements. In the aluminium industry there is typically only around 0.1 – 0.2 m of head available to prime a filter in typical DC casting arrangement. The head required to prime a ceramic foam or steel mesh filtering is much lower, making them suitable for DC casting practices.

A novel approach to filtering molten aluminium used during continuous or semi-continuous casting is to use a sock style filter bag fitted within the launder. This is a woven filter made from glass fibre typically bonded with a ceramic. It is particularly effective in oxide filtration and has the additional benefit of reducing turbulent flow during the transfer of molten metals. This type of filter is particularly effective for larger defects and agglomerates but is less effective at retaining particle like inclusions. The employment of the filter bag is common in the aluminium DC casting industry and is one approach that the magnesium industry could benefit from.

An alternative to filtering all together is to fit an inline cyclone particle removal in the transfer line [Katgerman et al., 2005]. This relies on the density difference between the undesirable inclusions and the bulk of the melt. The aim is that all the inclusions will be collected at the bottom of the cyclone and the clean melt continues on to enter the mould.

2.2.5.3 Transfer

A different approach to achieve high quality castings using launder or gravity fed systems with filtration is to use a transfer pumping system, which is commonly used in the aluminium industry. The advantages of using such a system is that more molten metal can be transferred in less time and as such there is less need for

superheating to accommodate heat loss during transfer. Transfer pumps operate by lifting the molten metal by an impeller into a piping system which can then be directed anywhere, providing more flexibility in foundry configuration. The only limitation is when not in continuous use external heating is required to prevent freezing of the molten metal in the piping system [Davis, 1993].

Alternatively melt siphoning, first trialled in the aluminium industry [Locatelli and Liu, 2010], offers a transfer process by which almost no surface turbulence is created. All of the melt is transferred under the free surface, when operated in weir mode which means incomplete filling of the siphon pipe, or when completely filled, thus there is very little opportunity for the entrainment of surface oxide films, Fig. 2-22. Fully automated siphoning removes the dependence on skilled operators and can be continuously operated, reliably producing quality castings. Siphoning offers a safe and reliable method of alloy transfer that improves efficiency and quality.

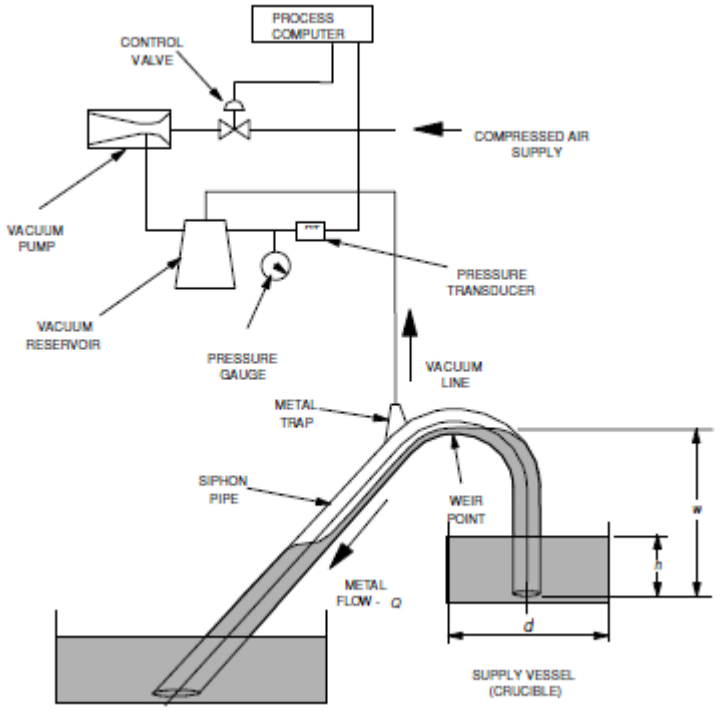

Figure 2-22 Schematic of siphoning process [Locatelli and Liu, 2010]

2.2.5.4 Inline Monitoring

Besides filtering and particle removal, monitoring of inclusion content can be employed to ensure an acceptable defect level is not exceeded. An alternative use of ultrasonic inspection techniques is to employ them to inspect the molten alloy. To achieve this, the ultrasonic probe must be modified to withstand the high temperatures of the molten alloy, which is achieved by using buffer rods [Ono, 2003]. This technique enables online inspection of the melt cleanliness prior to casting and has been demonstrated to detect signals from non-metallic inclusions 50 µm in diameter in a molten alloy at 780 °C. This provides a major improvement from the traditional techniques which involved the time consuming extraction of a sample followed by laboratory analysis which is often too slow to make any significant changes to the casting process. The ideal process would allow for online inspection of the melt while it is in the molten state, this is commonly achieved by the Liquid Metal Cleanliness Analyser (LiMCA) in the aluminium industry.

The LiMCA system operates within the molten alloy before casting and is an online technique used to detect inclusions. The equipment consists of an orifice in a tube suspended in the molten alloy which is aspirated in and out through the orifice using alternative pressure and vacuum. The presence of any particles which have passed through the orifice into the tube is detected by a change in the electrical resistance across the orifice which is directly in proportion with the size of the inclusion which passed through. This technique is very effective and is reported to be able to measure a minimum inclusion size of 20 µm in molten magnesium [Guthrie and Li, 2001]. The limitations of this technique are reported as blockage due to large inclusions, those around the same size as the orifice, and an inability to measure a wide range of inclusion sizes [Guthrie and Li, 2001].

Alternative melt cleanliness assessment methods are commonly used in industrial settings. The porous disk filtration analysis (PoDFA) and K-mould methods provide a quick assessment of the melt cleanliness prior to casting.

The PoDFA method involves the sampling of a small amount of the melt (~2kg) by pouring it into a preheated crucible which is fitted with a fine grade filter at the base. The crucible is attached to a vessel which contains a vacuum and draws the molten alloy through the filter in the pressure vessel. Any inclusions in the melt will then be collected on the filter surface which can then be analysed by metallographic examination. The measure of inclusion is then expressed as a fraction of the amount of inclusion in the area examined relative to the total mass of molten alloy filtered. This method provides a batch like inspection method and is good at identifying the type of large scale inclusions in the melt.

The Prefil method is a development on the PoDFA method which involves weighing the melt as it flows through the filter and plotting the results against time. A steeper gradient on this plot is representative of a cleaner melt as there are fewer blockages due to inclusions. This removes the need for metallographic examination, however it is still necessary to inspect the filter to understand the type of inclusion present [Djurdjevic et al. 2010].

The K-mould method is another batch like inspection method to assess the inclusion type and level of content in the melt. It is achieved by sampling a small volume of the melt prior to casting which is poured into a notched bar permanent mould. Once fully solidified, the bar is then fractured at each of the notches and visual inspection is carried out on each of the fracture surfaces. The number of inclusions is counted and the K-value is determined as the number of inclusions per section of the sample inspected. This method is very quick, however is not very suitable for large castings and does not discriminate between the different size and type of inclusions present [Wannasin et al., 2007].

2.3 Non-Destructive Inspection

Non-destructive inspection plays an important role in the production of high quality cast products. Typically all castings are inspected for both internal and external surface defects. Qualification of the casting against a recognised standard can add significant value to the product and provide assurances to the customer of the level of quality. Non-destructive inspection can be achieved by a range of techniques such as radiography, ultrasonic, electromagnetic or visual depending on the application.

The use of ultrasonic inspection as a NDI technique for light alloys was first developed by Shrayber in 1939 to inspect propeller blades [Banks, 1962]. The ultrasonic techniques and equipment employed today across the world still resemble those developed by the pioneers of ultrasonic testing methods for materials.

This section will discuss the ultrasonic inspection method and its application to defect detection, as used for all samples in this study. A discussion on the X-ray Tomography imaging technique will also be presented and its application in materials science and characterisation.

2.3.1 Fundamentals of Ultrasonic Inspection

Ultrasonic inspection relies on the propagation of mechanical vibrations in materials, typically these vibrations have a frequency above 10,000 Hz and are referred to as ultrasonic waves [Banks, 1962]. The use of high frequency (short wavelength) ultrasonic waves enables the detection of small defects in solid material. Propagation of the ultrasonic wave depends on the elastic behaviour of the material under inspection, as a result the wave will have different wavelengths in different materials [Halmshaw, 1991]. The only requirement is that the material in which the waves are to be passed through behaves in an elastic manner, such that there is a restoring force opposing any displacement of an atom. The wave can propagate through a material because as each particle begins to oscillate it will

immediately effect its nearest neighbour, the speed of propagation therefore depending on the elastic properties and density of the material [Banks, 1962].

Ultrasonic inspection detects reflections of the propagating wave at any interface between two materials with different elastic properties. The size and position of defects can be estimated from these reflections. However the true size, geometry and position require more detailed scanning due to the scattering effect of the defect on the ultrasonic wave [Banks, 1962]. Information on the grain size can also be obtained through analysis of the attenuation of the ultrasonic signal by different materials [Smith, 1982].

The generation of an ultrasonic wave utilises the piezo-electric effect demonstrated by some crystals as this is the only practical method to generate and detect the high frequency waves required. The ultrasonic probe consists of a transmitter and detector crystal both housed within the same unit, as shown in Fig. 2-23. The probe presents a pre-configured transmitter and receiver couple, known as a transducer, which can easily be set-up and operated for a range of materials.

Many scanning techniques and methods are possible with ultrasonic inspection such as A, B, C, and D scans which mainly differ in the format that the data is presented. The A scan displays the ultrasonic signal amplitude on the Y-axis against a linear time-base on the X-axis on a cathode ray tube (CRT) display. B scan is very similar to an A scan but will represent the size and position of the defect on a cross-sectional plane normal to the surface on the X-axis on a CRT. The C scan is also represented in a 2 dimensional format but as a test surface plan view on a display screen, this technique is commonly used with immersion inspection. The defects are indicated as bright patches in their respective position on plan view, however this does not provide any information on the through thickness location of the flaw. The D scan is very similar to the C scan where the data is displayed as a 2 dimensional cross-section but the section is normal to the test surface. Thus, the combination of the C and D scan provide the exact location of the defects

contained, the simultaneous display of both is referred to as a P scan [Halmshaw, 1991].

Focused probes and phased arrays are another two ultrasonic scanning methods that involve specialised probes and equipment that can be steered to a focal point in order to increase inspection quality and reduce inspection time [Drinkwater, 2006]. The two most common methods of inspection for materials, and those used in this study, are the single hand probe transducer and the automated immersion probe scanning.

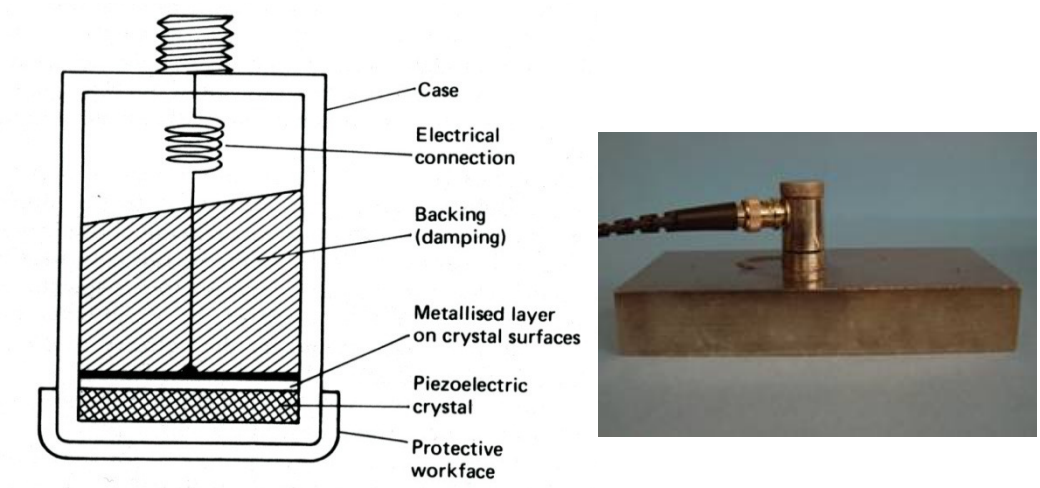

Figure 2-23 Schematic of an ultrasonic probe suitable for hand scanning, photograph of hand probe on calibration block [Halmshaw, 1991].

Automated ultrasonic inspection is simply a mechanically controlled transducer probe that is linked via computers and motors to accurately scan the complete component. With the computer and motor interaction a map of the scan responses can be created from which data on the internal structure can be obtained. The use of computers in this process enables the inspection quality standard to be input and the response data to be analysed relative to the standard. The computer can then instantly identify any response signals that appear to be above the limits and record its location. However the limitation of this approach is that defect response signals cannot be maximised by small movements of the probe, the path the probe takes is predetermined before the scan begins and fine control of the probe is limited by the step size of the motor movement [Deutsch, 2000].

A major problem with using an ultrasonic probe is ensuring suitable surface contact is achieved to transmit the ultrasonic signal. Components often have their surfaces machined to create a smooth surface and coupled with a gel to improve transmission of the signal. In the case of immersion inspection, which is how most automated scanning is carried out, water is used as the coupling material. However the formation of bubbles on the submerged probe and component surface can inhibit transmission. The formation of bubbles on the component surface can be addressed by attaching a brush to the probe such that the component's surface is brushed immediately prior to being scanned. However, bubble formation on the probe surface is still a major problem. It is estimated that in practice over a two meter long billet around 3 to 4 dB can be lost due to bubbles on the probe surface [Mackie, 2011].

2.3.2 Flaw Detection by Ultrasonic Inspection

Flaw detection by ultrasonic inspection relies on the reflection and refraction of ultrasonic waves at the interface of the defects. Any defect which reflects the ultrasonic energy can be considered as a source of an ultrasonic signal. For defect detection achieving a strong reflected response is most important.

The height of the returning signal is directly proportional to the cross-sectional area of the defect's reflecting surface and inversely proportional to the distance from the receiver [Halmshaw, 1991]. This makes it very complex to determine the flaw size directly from the height of the response signal alone. In the case of an air filled crack in metal, a high reflection of the energy in the wave can be assumed, as there is very little transmitted energy. However, for cracks with a width less than one wavelength there is the risk of partial transmission across the air gap, thus making the defect transparent to the ultrasonic waves and sizing of the crack unrealistic. Real cracks such as gas pores, entrainment defects and stress corrosion cracking can present very complex morphologies, including 'closure' of the crack where the two faces contact. Closure of a crack may also be due to plastic deformation near the crack tip, an oxide particle or corrosion product within the newly formed crack.

Thus a calculated minimum detectable defect size for an inspection system can severely overestimate the minimum size of defect that can actually be detected.

Identification of complex multi-branched defects by the pulse-echo technique is not recommended [Thompson, 1984]. This type of defect will produce much smaller responses than equivalent for their size, however they may be detectable by their wider response signal. It is also a problem that large but badly oriented defects may not be correctly identified. The problem of badly oriented defects in cast material is particularly prevalent, compared to those contained in wrought products, in which the defects are generally oriented parallel to the structural flow directions.

The reflected signal alone cannot be used to establish a defects size, but it is usually compared with responses from defects of a known size. The amplitude of the reflected pulse from the know defects is recorded and set as the threshold for acceptable defect sizes according to the relevant quality standard. The detection and recording of the responses from the defects of known size establishes the desired probe sensitivity and the distance amplitude correction (DAC) curve [Halmshaw, 1991]. This enables defects at different depths in the billet to be detected by essentially determining the loss of response amplitude from the same sized defect at different depths. The DAC is generated by the use of a calibration block, manufactured according the to the quality standard from the same material and geometry as that to be inspected, with pre-determined flat bottom drilled holes to represent defects. The construction of the DAC involves recording the individual response from each drilled hole, shown in Fig. 2-24. The gain of the probe is typically adjusted such that the response from the first, closest to the surface defect achieves around 80% full screen height. These responses can then be used to plot the DAC curve, Fig. 2-24, for that specific quality standard [Halmshaw, 1991; Hislop, 1969]. The DAC permits the assessment of defects at any depth of the sample to be detected and compensates for the attenuation and delay in signal from a defect at any depth in the material.

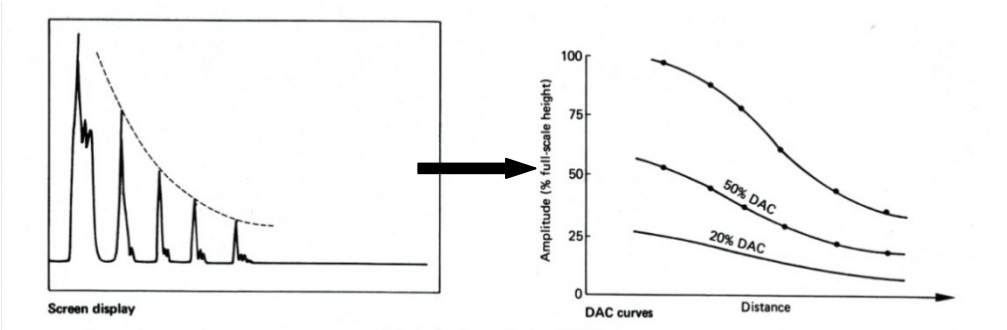

Figure 2-24 Construction of a distance-amplitude correction (DAC) curve [Halmshaw, 1991].

Once the DAC curve has been established, scanning can be carried out and any defect response above the DAC curve threshold is identified as an unacceptably large defect. This is the most effective method of assessing the defect size in a certain material.

Beyond simply identifying a defect that exceeds the standard it is almost impossible to establish the defect size by ultrasonic echo height. Even on comparison with the standard it is difficult to size a defect from the response, since the standard is for flat surfaces lying perpendicular to the ultrasonic beam. In reality no defects are ever shaped in this idealised way, they are convex or concave in shape with rough surfaces which are potentially contacting. It has been demonstrated [Batien, 1968] that changes in the shape of a defect can cause considerable variations in its reflecting properties, to the extent that it is predicted a polished convex surface facing the probe (i.e. wave travelling towards it) would reflect no ultrasonic energy. Bastien continues to state that an evaluation of a defect by its response echo can be made if prior identification of the defect from the indications provided or knowledge of the reflecting properties of the defects likely to be found [Batien, 1968]. This is what the DAC curve attempts to achieve.

Ultrasonic probes often only have limited regions across which they are significantly sensitive enough to detect defects. To overcome the limitations of probe sensitivity it is more desirable to employ a multi-zone transducer [Lutjering, 2007]. A multi-zone transducer is one that involves an array of transducers each focused at a different depth within the volume of the component. Each transducer inspects a

cylindrical sub-element of the volume, in this case a billet, enabling the detection of smaller defects since the probes can operate at a higher sensitivity. This method provides better detection of smaller defects where necessary but requires elaborate equipment.

More detail, such as the size of the reflecting defect can be established by using the time of flight diffraction (TOFD) technique, Fig. 2-25, which relies on the diffraction of ultrasonic waves at the defect tips to give more detail on the defect size and location. However this approach requires separate transmitter and receiver probes that must traverse the sample surface at least twice to acquire sufficient information. The limitations of this inspection method are that confusion between the many different defects contained and the multiple possible vibration modes of the waves can inhibit clear interpretation of the response signals [Halmshaw, 1991]. Additionally in an industrial environment time restraints can also limit the suitability of this method.

Analysis of ultrasonic inspection results can take various forms depending on the method of scanning. It is not uncommon for the user to be required to continually monitor the output on a CRT display, however this can be improved with computer programmes to detect and record the defect locations, often programmed to sound an alarm when the DAC threshold or any other predefined limit is exceeded by the response. Further developments include ultrasonic tomography which produces a 3D model of the inspected volume, however collection of data for ultrasonic reconstructions is significantly more complex than the established X-ray scanning [Jones, 1993]. The time of flight diffraction (TOFD) method, discussed previously is suitable for tomography imaging, enabling a more accurate determination of flaw size, shape and location [Capineri, 1992]. This technique provides the advantage of a reconstructed image rather than raw data by implementing a reconstruction algorithm based on the data acquired with standard ultrasonic instruments.

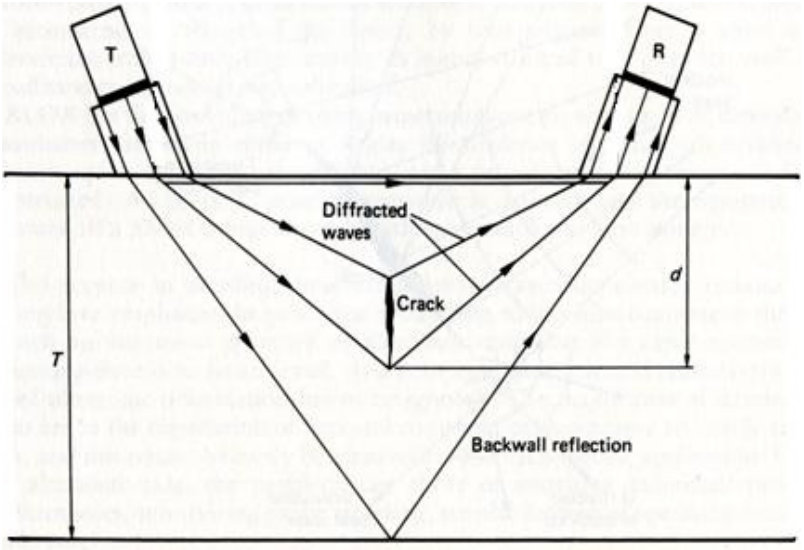

Figure 2-25 Schematic of time-of-flight arrangement (T=transmitter, R=receiver).

Alternative methods to the immersion and hand probe ultrasonic inspection exist such as water column coupled probe (WCCP), partial immersion and electromagnetic transducers (EMAT) ultrasonic inspection. The WCCP technique involves the use of a guided water jet of 30-50 mm in diameter for transmission of the ultrasonic waves between the probe and the specimen. This technique is often used in billet inspection and is capable of through-transmission testing and pulse-echo testing. The WCCP technique is used for billet scanning whereas partial immersion and EMAT are not best suited for this application [Deutsch, 2000].

2.3.3 X-ray Tomography as a Non-Destructive Inspection Technique

The recent increase in available computing power has allowed X-ray tomography imaging techniques to be transformed into a commercial non-destructive inspection technique. The technique was initially developed by Houndsfield in 1979 for medical applications [Halmshaw, 1991]. Recently there have been many advances, but is principally the same technology that is used today in materials science X-ray Computerised Tomography (XCT).

The XCT inspection technique is a non-destructive inspection method capable of generating detailed 3D images of the internal structure of a material. The advantages of tomography over traditional 2D analysis methods are; determination

of the true number of objects per unit volume not just the number predicted from 2D sections, correct phase size distribution determination and the connectivity of phases which is clearly a 3-dimensional parameter [Salvo et al., 2003]. However it is sometimes still necessary to complete 2D analysis, this can still be extracted from the 3D analysis which is extremely useful [Salvo et al., 2003].

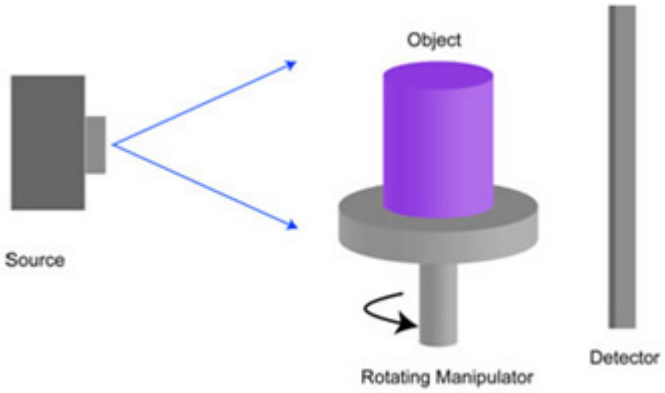

Figure 2-26 Schematic of tomography inspection arrangement

XCT imaging collects data by directing an X-ray beam towards a sample and the transmitted X-rays are recorded on a detector located behind the sample, as in Fig. 2-26, this is considered the scan phase. The detector can then produce an image which is a projection of superimposed information of the internal structure. According to the Beer-Lambert law, the absorption by the material is calculated from the ratio of transmitted to incident X-rays on the detector, which can be directly related to the density, the atomic number and the energy [Hsieh, 2009]. By acquiring a large number of 2D projections while rotating the sample over 180° and use of a suitable reconstruction algorithm an image of the volume scanned can be generated; this is the reconstruction phase. The final stage in XCT inspection is visualisation to allow image analysis, this involves using suitable software to convert the reconstructed matrix of pixels each containing data into a greyscale image [Salvo et al., 2002; Nicoletto et al. 2010; Herman, 1995]. The resulting contrast between voxels in the reconstructed volume is then labelled and visualised as separate phases. This provides a route to locate defects or any inhomogeneity contained within a volume that can be analysed.

Typical XCT inspection systems for materials science applications involve a polychromatic X-ray cone beam in combination with a high speed and high resolution matrix detector, capable of resolutions down to 1 µm [Kastner et al., 2010], followed by reconstruction using a back-projection based technique. Alternative systems utilise a synchrotron radiation source which provides a parallel monochromatic beam to achieve high resolution scanning [Maire et al., 2006].

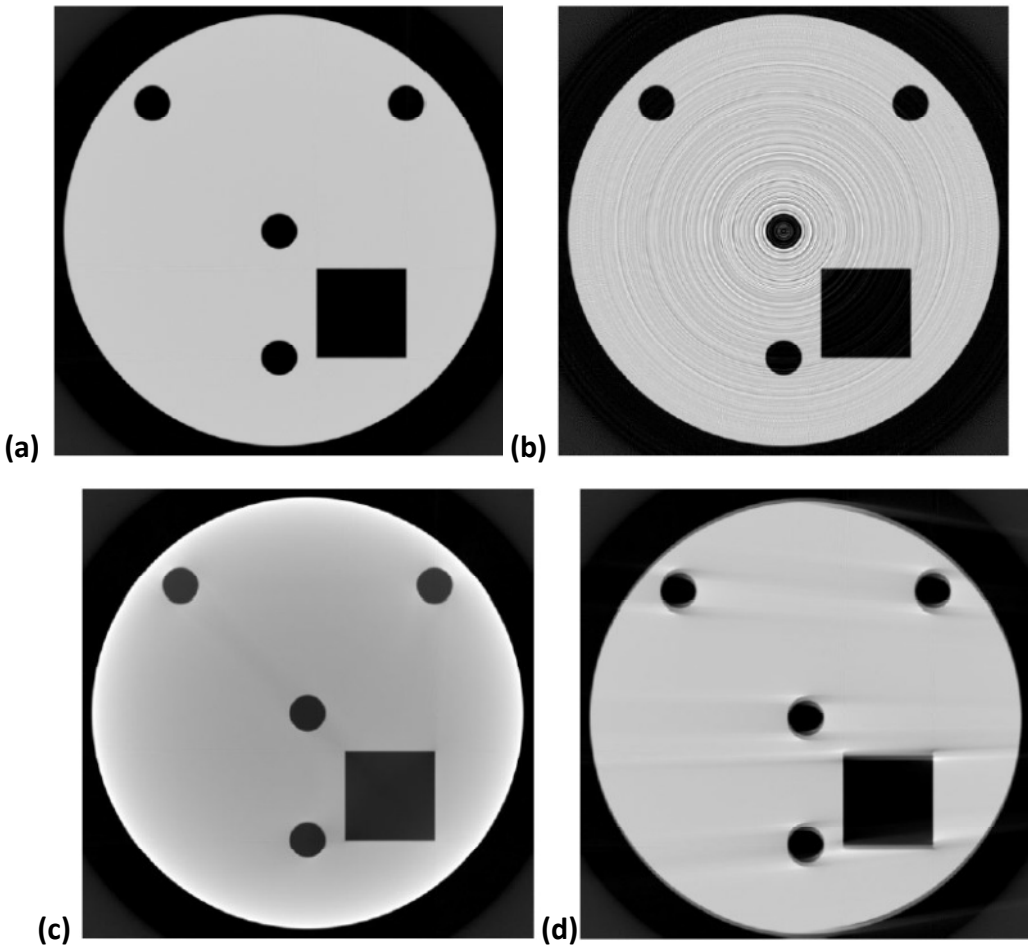

Figure 2-27 Centre slice of a CT scan, (a) perfect reconstruction, (b) reconstruction with ring artefacts, (c) reconstruction with beam hardening and (d) reconstruction showing double edges and streaking due to sample movement [Davis and Elliot, 2006].

A major limitation with XCT is the production of artefacts during the reconstruction of the raw data. Artefacts are defined as structures that are present in the reconstructed data set that are not present in the sample. Artefacts may occur due to a faulty pixel in the detector array which continually glows or continues to be excited even when not exposed to any X-rays, these are typically referred to as a

ring artefact as they are swept around the volume of the reconstructed sample, Fig. 2-26 (b). Beam hardening is a problem associated with polychromatic X-ray sources that can result in cupping and dark streak artefacts. The problem of beam hardening occurs due to a seemingly constantly changing energy distribution and attenuation coefficient resulting in apparent changing density across the volume of a homogeneous material, Fig. 2-26 (c). Polychromatic cone beam X-ray tomography is more prone to this artefact than monochromatic sources [Kastner et al., 2010] since low energy photons are attenuated more than the higher energy photons [Krumm et al., 2008]. Misalignment of the centre of rotation can result in artefacts that appear as double edges in the reconstructed image. This is similar to the effect caused by movement of the sample between imaging the result is double edges and streaking, Fig. 2-26 (d) [Davis and Elliot, 2006].

2.4 Casting Simulation

Computational simulations are a useful tool in the development of alloys, casting processes and equipment. By using simulation software, models can be developed to permit the trial of novel solutions to existing casting problems more rapidly and with less expense than traditional experimental methods.

Two methods of computer modelling and simulation were used in this study, process modelling and microstructural modelling. Process models were used to simulate fluid flow, cooling rate and temperatures during casting. Microstructural models were employed to simulate the microstructural development during solidification, predicting the phases which will form and the nature of these phases.

This section will introduce and review the software relevant to this study and identify how they can be used to achieve the aims.

2.4.1 Casting Flow Simulation

The microstructure of a cast material is known to be affected by the flow of the melt as it enters the mould [Flemings, 1974; Eskin and Katgerman, 2009; Eskin et al., 2004]. A wide range of casting simulation software packages are available commercially, however the use of Alsim for this study was dictated by the availability and compatibility with existing models used by Magnesium Elektron, U.K. Other popular software packages were identified [Thomas and Zhang, 2001] as CFX, Fluent, Magmasoft, Flow 3D, Physica and Phoenics. Casting simulation software enables the simulation of 3D volumes, however these can often require large amounts of computing power and time. Accurately depicting the geometry as a mesh, as is required by the FEA method, often requires a fine mesh size especially to represent curved surfaces, which increases the computing power required. This is essential to reduce error in calculation of fluid flow and heat transfer along mould walls. Simulation of the casting process is a challenging task as it involves a combination of complex phenomena such as multiple free-surfaces, heat transfer in the metal and the mould, phase changes all over different length and time scales.

The process can be over very quickly but all must be considered in order to accurately model the casting process.

Alsim is a simulation code written in Fortran 90 developed by the Institute for Energy Technology, focused on modelling the fluid flow, heat transfer and the development of stresses in DC casting. Alsim is a three dimensional finite element method (FEM) solver for the Navier Stokes equations [Mortensen, 1999] which is common with most other flow simulation software. Capable of simulating combined thermal and mechanical conditions Alsim is able to solve any incompressible fluid flow problems over a prescribed arbitrary geometry [Holmas et al. 2005].

Transfer of the melt before it reaches the mould is one of the most important stages of the casting process. Filtering is often used during the transfer, as discussed in section 2.2.5.2, however subsequent devices to control and direct the flow to the mould are also necessary. It is at this stage, downstream of filtering, that the melt can pick up inclusions and oxides. Modelling of this stage of the process has been completed in previous studies for continuous casting of steel, which is transferable to DC casting of aluminium and magnesium alloys [Zuidema and Katgerman, 2002; Xu et al., 1998; Thomas and Zhang, 2001]. There have also been attempts at using physical modelling using water, as discussed in section 2.2.1, for comparison and validation of the computational models.

As discussed, the flow of the molten alloy into the mould controls the flow pattern within the mould. It has been demonstrated, by computer simulation, that it can be overcome by the use of a distribution bag which diffuses some of the jet and as a result the flow is slower and more stable [Sengupta et al., 2005]. The typical flow pattern in the mould during the DC casting of aluminium, Fig. 2-28, shows clear recirculation for the different types of inlet. Clearly reducing the recirculating flow and the undesirable microstructure that can form as a result. This is a strong indication of the value of computer modelling and how it can inform improvements with minimal cost.

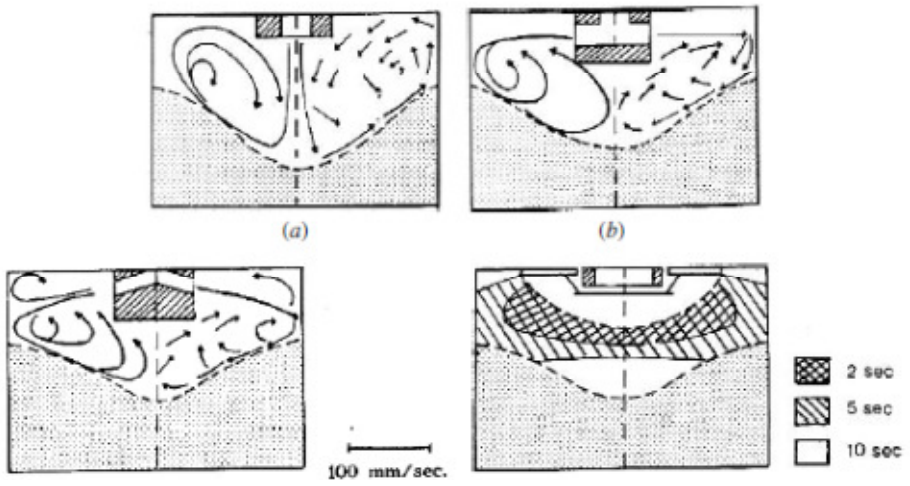

Figure 2-28 Flow patterns left side, velocities right side for different metal entry systems, (a) vertical entry, (b) horizontal entry, (c) oblique entry and (d) through a distribution bag [Sengupta et al., 2005].

2.4.2 Phase Prediction: CALPHAD Approach to Microstructural Characterisation

Computational methods are now available to simulate the phase evolution during solidification of multicomponent alloys. Calculation of Phase Diagrams (CALPHAD) software is well established and used for casting process simulation where it is regarded as an important tool in product and process design. This method of solidification modelling has been demonstrated to be applicable to multi-component alloys by a good correlation with experimental data [Saunders and Miodownik., 1998; Spencer, 2008].

The CALPHAD model relies on a database containing Gibb's energy data for each phase as a function of temperature, pressure and composition. The stable phases at each temperature are identified by a Gibb's energy minimisation process. Excellent prediction of phase formation is achievable by setting constraints in the model to include non-equilibrium conditions, such as the Scheil model [Glicksman and Hills, 2001]. The Scheil solidification model assumes no solute diffusion occurs in the solid phase during solidification and there is complete mixing in the remaining liquid. The CALPHAD model phase predictions can be coupled with semi-empirical models to predict thermal, physical and mechanical properties. JMatPro

is an example of software that takes this approach and is one benefit over using other simulation software [Saunders, 2001, Saunders et al., 2003].

JMatPro can also provide detailed information on phase formation during solidification which is usually not possible by experimental means [Guo et al., 2005]. Predictions give details of the weight fraction and formation temperature for each solid phase, which can be useful in the search to eliminate or promote the growth of certain phases. The power of the prediction software allows accurate simulations to be completed for the AZ80 alloy without the need for experimental confirmation due to the level of confidence that can be placed in the model's accuracy. It has been shown [Guo et al., 2005] that thermo-physical and physical properties of multi-component alloys during solidification can be calculated where there is no current experimental information.

2.4.3 Precipitation Modelling

The ability to accurately predict the growth of Al-Mn compounds may provide a solution to prevent clusters forming and producing cleaner material. Using computer models of the growth process provides significant savings in cost and time compared to experimental efforts.

Early work carried out by Langer and Schwartz [Langer and Schwartz, 1980], proposed equations to describe concurrent nucleation and growth of droplets in near critical fluids. This work was developed by others including Kampmann and Wagner [Wagner and Kampmann, 1991] for prediction of solid state precipitation in numerous other alloy system microstructures, including light alloys [Robson and Prangnell, 2001; Robson, 2004].

The Kampmann and Wagner Numerical (KWN) model is most widely used for predicting precipitation in the solid state, although the general framework is equally suited to prediction of condensation from vapour or formation of solid precipitating (of low total volume fraction) in liquid.

Prediction of the evolution of a second phase in magnesium alloys can be achieved using a modified version of the KWN precipitation model.

The KWN model attempts to predict the evolution of the precipitate size distribution. It employs the classical theory of nucleation and growth with the particle size evolution evolved under the natural action of these processes.

The essential features of the KWN model are;

(1) The continuous time evolution of the particle distribution is considered in terms of discrete time steps.

(2) The continuous size distribution of the particles is discretised into a large number of size classes.

(3) The number of new particles in each time step is calculated using classical nucleation theory. The exchange of particles between size classes is calculated assuming solute diffusion is the rate limiting process and a spherical growth morphology. The Gibbs – Thomson relationship is used to calculate the modified interfacial compositions for each size class at each time step.

(4) The change in matrix solute level due to precipitate formation or dissolution is calculated at each time step using the mean field approximation.

With these features the model is able to predict nucleation, growth and coarsening, without any artificial constraints, irrespective of the order in which they occur [Robson, 2004].

As stated the model is coupled with the classical nucleation theory which gives the equation for time dependent, homogeneous nucleation as

$$I = NvZ\beta^* \times \exp[-4\pi\gamma r^{*2} / 3kT] \exp(-\tau/t)$$

Where Nv is the number of nucleation sites per unit volume, Z is the Zeldovich factor considering the decay of cluster above the critical radius size, γ is the interfacial energy of the nucleus, r* is the critical radius size and τ is the incubation time for nucleation, k and T have their usual meanings.

For nucleation to occur the energy barrier must be overcome such that it is favourable for the newly formed nucleus to grow. The energy balance is that between the cost of creating a new interface with the surrounding matrix and that released due to the creation of the particle volume, Fig. 2-29.

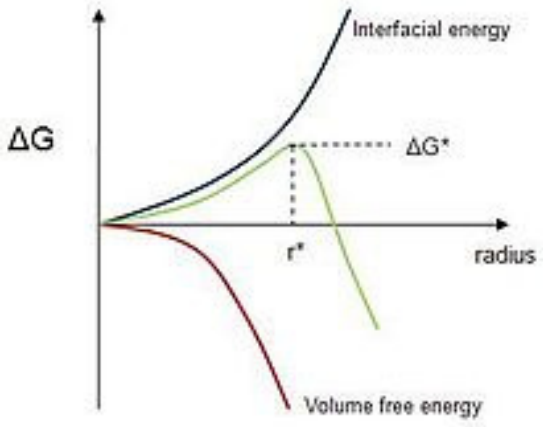

Figure 2-29 Critical radius and free energy barrier for nucleation.

The critical radius is calculated at each time step and used to calculate the nucleation rate. The nucleation is assumed to occur anywhere in the liquid and the radius of the newly formed particles is assumed to be 10% larger than r*, Fig. 2-29, to enable them to grow.

The growth of successfully nucleated particles often depends on the rate of diffusion of solute to the particle interface. This is known as diffusion controlled growth, Fig. 2-30(a). However often growth is not restricted by the diffusion rate and is limited by the interfacial energy barrier that must be overcome for atoms to join onto the particle surface. This case is known as interface controlled growth, Fig. 2-30(b). A third scenario may occur where both mechanisms affects the growth rate, this is known as mixed mode growth, Fig. 2-30(c).

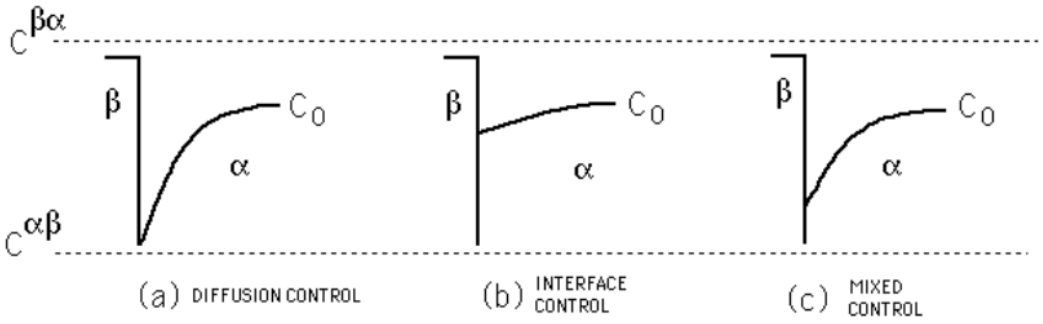

Figure 2-30 Concentration profile at the interface between a precipitate (β) and a matrix (α) under different rate controlling processes.

Coupled with the classical nucleation and growth theories, the formation of a second phase in a solidifying alloy can be predicted using the KWN model. Considering the nucleation stage to occur by the random formation of clusters of atoms above the calculated critical radius size for the solidifying conditions. Growth of these clusters through the absorption of atoms from the liquid phase onto the solid is followed by a period of coarsening, which involves the dissolution of small particles at the expense of larger ones, driven by an overall reduction in interfacial energy [Robson, 2004]. The outcomes from such a model are the particle size distribution, the volume fraction, the mean particle size and the concentration of the matrix [Nicolas et al., 2003].

2.5 Summary and Potential for Current Study

In summary there has been much research carried out into the casting and inspection of magnesium alloys. However, there has been little work completed using the combination of ultrasonic inspection and X-ray tomography imaging techniques to assist in characterising defects produced during casting. Specifically the study of entrained oxide defects in cast material and the growth of the intermetallic phase, is one which has been the focus of recent research and is still on going.

The problem, at the core of this research, arises due to the combination of the industrial setting and the requirement for high quality products. Achieving this involves sophisticated techniques only currently available in research laboratories, in combination with more traditional methods and the support of industrial expertise. This research will draw on the information available from a range of techniques and approach the study using the appropriate scientific knowledge in producing recommendations to achieve the objectives. This combination of an industrially relevant problem solved using scientific principles presents the opportunity for an interesting research project, producing useful outcomes for both the organisation and the relevant field of enquiry. Combining techniques plus support from computer modelling predictions of the relevant processes will result in a solution to increase the quality of the final cast product produced by Magnesium Elektron, U.K.

It is intended that the defects will be detected using the immersion ultrasonic inspection equipment as used for industrial castings and then characterised using laboratory based XCT imaging techniques. This will establish a better understanding of the type of defect found in the DC castings. Once confirmed computer simulation and modelling techniques will be employed to assist in identifying a possible formation mechanism of the defects which will indicate methods by which they can be prevented. With the end result of modifying the casting and inspection such that high quality casting can reliably be produced.

3 Experimental and Analysis Techniques

In order to characterise and investigate the defects in DC cast alloys, AZ80 alloy was prioritised, following the suggestion of Magnesium Elektron, U.K. Magnesium alloy ZW3 was also characterised by some of the same methods used for the AZ80 alloy. These two alloys are examples of important medium strength forging alloys which were the focus of this study as they were both troubled by high defect levels. The alloys, once cast, all followed the same process to allow the maximum amount of information to be gained from each sample. The alloy billets were fully inspected by ultrasonic immersion inspection to locate the defect along the billet length. A slice sectioned from the established location was then inspected by a hand operated ultrasonic probe to locate the defect in the slice. A sample was then sectioned from the billet slice and imaged by XCT methods. The samples were then imaged by a serial imaging process using both optical and scanning electron microscopy methods.

Many other techniques were used for characterisation, such as energy dispersive X-ray analysis to determine compositions, FIB and fractography of tensile fracture surfaces. Each of the techniques used are explained in this chapter.

3.1 Sample Preparation

The material used in this study was as-cast and homogenised AZ80 alloy supplied by Magnesium Elektron, UK. AZ80 alloy is based on the Mg-Al binary alloy system with the additional main alloying elements of zinc and manganese. This material is a high strength alloy typically used for extrusions and forgings of simple designs used in the automotive and communications industries. The nominal composition of the alloy is given in Table 2 below.

An additional alloy system was investigated to extend this study and to observe similar defects in a zirconium containing alloy. The alloy was received and prepared in exactly the same as the AZ80 and the nominal composition also listed in Table 2.

Alloy	Al (wt.%)	Zn (wt.%)	Mn (wt.%)	Zr (wt.%)	Mg(wt.%)
AZ80	**8.5**	**0.5**	**0.12 min.**	**-**	Balance
ZW3	-	**3.0**	**-**	**0.6**	Balance

Table 2 Alloy composition [Datasheet: 441, Magnesium Elektron, U.K.].

The AZ80 alloy samples were received either as a complete slice of a billet or a smaller sample (4 x 4 x 4 cm) from within a slice. All materials provided were in the homogenised condition, sectioned from locations indicated to contain defects by ultrasonic inspection. The surface of the billet had been machined to remove the rough casting surface, as was standard practice during production. Numerous samples were obtained by this method and will be referred to as necessary throughout the work.

Each sample was cut from identified locations in the billet slices using a band saw and a Struers minitom fitted with a silicon carbide cutting disk. The samples were cut into 10 x 10 x 10 mm specimens to be prepared for optical microscopy, scanning electron microscopy (SEM) and energy dispersive X-ray spectroscopy (EDX) for compositional analysis. The cut samples were mounted in epoxy resin and ground using water lubricated 180, 320, 600 and 1200 grade SiC grinding papers, following

conventional metallographic preparation techniques. This was followed by polishing for 1 minute on each of a 3 µm and 1 µm diamond polishing wheel lubricated with oil based solution. A final polishing step was carried out using an oxide particle suspension (OPS) to create as suitable surface for inspection. Thorough washing and drying of samples was performed after each grinding and polishing stage using methanol and an air dryer.

Selected samples were etched after being prepared in the same way as described above followed by submerging them in Picral etchant for 8 seconds in order to reveal the grain boundaries. The recipe for the Picral etchant is listed in Table 3 below.

Ingredient	Quantity
Picric acid	4.2g
Acetic acid	10ml
Ethanol	70ml
Water	10ml

Table 3 Picral Etchant recipe.

3.2 Optical Microscopy

Optical microscopy was carried out using an Olympus BH2 microscope with a Zeiss Axiophot camera to examine the etched and unetched microstructures. The samples were examined and images captured using the camera at magnifications of 10, 50 and 100 times objective magnification with a resolution of 2080 x 1540 pixels.

3.3 Scanning Electron Microscopy

SEM was carried out on the alloy samples to characterise both the microstructure of the AZ80 alloy and any defects revealed by the standard metallographic preparation as described above. A Zeiss Evo 60 SEM was used to image, connected to Inca software for EDX analysis. The samples were prepared in the same way as

above for optical inspection but were finally mounted onto a metal stub and a conductive path created using DAG silver paint. Images were captured using back scattered electron (BSE) and secondary electron mode at different magnifications and the same used for EDX. Both imaging and EDX was carried out using an accelerating voltage of 20 kV and a spot size of 300.

3.4 Focused Ion Beam Milling

Focused ion beam milling in combination with SEM imaging was completed using an FEI Quanta 3D dual beam FIB. This serial imaging technique was used to characterise the internal structure of the defects fully. The samples were prepared following the same metallographic preparation stages as described above and mounted on a metal stub. This technique involved capturing 150 images of the internal surface revealed by the FIB milling, covering a length of 2 µm along the defect. All imaging was carried out at an accelerating voltage of 5 kV.

3.5 Microstructure Analysis

3.5.1 Grain Size Analysis

The size of the grains in the samples prepared for optical microscopy were determined using the linear intercept method. This technique involves drawing lines in a grid across the image, using ImageJ [Abrmoff et al., 2004], and counting the number of times the lines of the grid crosses a grain boundary. Dividing the line length by the number of grain boundaries crossed results in the average grain size being calculated. A minimum of five different images were used in the determination of the average grain size for each location, each covering around 35 grains and an area of 2.6mm^2 which gave a representative grain size for the sample. The standard deviation of the average grain size was calculated by,

$$\text{S. D.} = \left(\frac{\sum(x_i - \bar{x})^2}{n_t - 1}\right)^{1/2}$$

where x_i is the average grain size in image i, and $\bar{x}$ is the average grain size calculated from all images for the location of interest and n_t is the number of images considered.

3.5.2 Particle Analysis

The measurement of second phase particles was assessed both in terms of size (equivalent circular diameter) and area fraction. The analysis was carried out on both optical micrographs or back scattered electron images, which provided good contrast between the particle and the matrix. At least ten images were used for each location at which the particle sizes were to be measured. To measure the particle content and their sizes ImageJ was used to convert the image to a binary image containing only the particles of interest, where the particles are black and the rest of the image is white. The measuring was completed automatically by ImageJ and the outputs were individual particle size and area fraction. Manipulation of this data provided the average and maximum particle size and the average area fraction. The same technique was used for the cooling rate experiment samples where back scattered electron images only were used.

3.5.3 Particle Clustering

A tessellation approach was used to describe clustering of the intermetallic particles. The tessellation technique involves the growth of a region surrounding a particle until this region impinges on a neighbours region. The region is grown from the edge of each particle and continues in all directions at the same rate until each boundary comes into contact with all of its neighbouring cells. This method is more appropriate for this situation instead of treating each particle as a point as discussed by Murphy for the analysis of metal matrix composites [Murphy et al., 1997; Lewandowski et al., 1989]. The average region size was measured and used as a relative comparison between the normal and defect containing regions of the microstructure. The tessellation was carried out using binary images in ImageJ software and from the results the average region size calculated. Images used were captured using an optical microscope of second phase particles from random locations in the microstructure and of those that form part of a defect.

3.6 Ultrasonic Inspection

3.6.1 Automated Ultrasonic Inspection

Automated ultrasonic inspection is completed as part of the billet production process at Magnesium Elektron, UK. The same procedure was used during this study as the samples were obtained from production stock. The inspection process uses the GE Inspection custom immersion tank, Fig. 3-1, fitted with an immersion type 19 mm diameter, 5 MHz probe. The software used for this inspection was K-Scan imaging software and ultra-PROOF chart, in combination with a USIP 40 High Performance Flaw Detector.

Figure 3-1 GE Inspection custom ultrasonic immersion tank.

Calibration of the automated ultrasonic inspection equipment was completed both before and after each scan was carried out. The quality standard used for inspection of AZ80 castings is SAE-AMS-STD-2154 [AMS-STD-2154, 1998], used for all samples in this study. Calibration was achieved using a calibration block, manufactured according to the standard for A level qualification, from a previously inspected section of AZ80 billet produced by the same process. The standard calibration block must replicate the material that the equipment is being set up to scan, i.e. round billet, same diameter, same grain size, same probe to surface distance and same surface finish. The calibration block contains a series of flat bottom holes drilled at prescribed depths to establish the response threshold

between defect that is within standard and one that is outwith, accounting for the depth of the defect within the billet. By locating each of the flat bottom holes and recording their response the probe was set up to ensure the correct sensitivity. This generated the distance amplitude correction (DAC) curve, Fig. 3-2. The probe sensitivity was increased by a further 9 dB in order to compensate for the increase in sensitivity required to achieve AA level quality, as no AA standard calibration block was available.

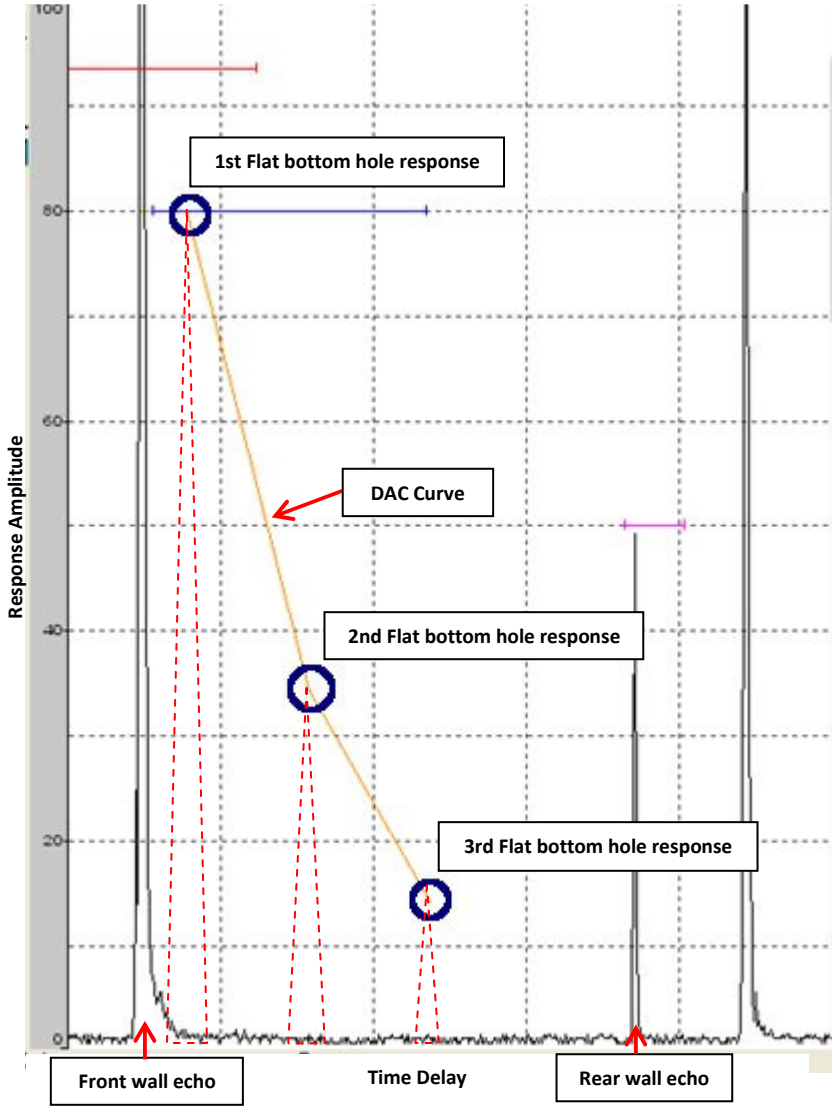

Figure 3-2 DAC curve generated during calibration of ultrasonic probe to standard probe SAE-AMS-STD-2154. Flat bottom holes detection indicated by blue circles and response peaks superimposed, red dashed line.

Ultrasonic scans were completed of the entire billet surface area to ensure any defects contained within the material that area out with the standard are

identified. Only half of the billet diameter was scanned at any time. This is to ensure the volume being scanned is within the optimum range for the probe.

Any defect to give a response signal above the established DAC was identified as a defect by the computer and marked on the output map of responses.

The scan axis parameters were set as shown in Table 4, in combination with the probe used at a frequency of 5 MHz. The automated equipment was able to achieve a theoretical resolution of 500 pulses/mm in the radial/through thickness direction, 1625 pulses/mm along the length of the billet and 21 pulses/degree on rotation.

Axis Parameter	Setting
Image steps (rotational)	0.1°
Turning speed	50 °/second
Image steps (longitudinal)	0.1mm
Traversing speed	55.4mm/second

Table 4 Scan axis parameters used for automated ultrasonic billet scanning

3.6.2 Ultrasonic Hand probe Inspection

The ultrasonic hand probe inspection procedure was completed using a ¾" dual crystal hand probe with a gel coupling on the billet slices. The probe was calibrated using a SAE-AMS-STD-2154 flat-plate calibration block, manufactured by the same method as discussed previously, for A level quality. Again the probe sensitivity was increased by a further 9 dB in order to compensate for the increase in sensitivity required to achieve AA level quality, as no AA standard calibration bock was available.

The probe was passed across the full billet slice face and the responses monitored manually on a CRT display. Any defect response was marked by hand and cut out for further inspection, as in Fig. 3-3 below, leaving 2 cm of material around the defect location, using a band saw and a SiC cutting wheel.

Figure 3-3 AZ80 billet slice marked for sample cutting.

3.7 X-ray Tomography Methods

X-ray computed tomography (XCT) inspection was carried out to visualise defects contained within the samples located by ultrasonic inspection. The samples were cut directly from the billet slices, as described previously, and had received no further preparation.

XCT was completed using the Nikon Custom Bay and the Metris X-Tek XT H 225 equipment. The tomography equipment consists of a tungsten X-ray source, samples were mounted on a putty or foam base to elevate them from the sample holder and manipulator for clarity during imaging. The detector consisted of a 2000 x 2000 pixel array. The result is a collection of between 1500-2000 projections which were reconstructed using a Feldkamp-Davis-Kress (FDK) algorithm for cone beam geometry [Feldkamp et al. 1984] into a 3D volume. The reconstructed volume contained voxels each assigned a grey-scale value which corresponds to the X-ray attenuation at the respective location in the sample. The X-ray attenuation coefficient is a function of the density and atomic number of the elements present in that volume in the sample. Thus, contrast was achieved between the regions of higher and lower density within the sample and the different phases present in the sample identified. Full details of this technique are presented elsewhere [Maire et al,. 2001; Salvo et al., 2003; Kastner et al., 2010; Salvo et al., 2010(b); Scarfe and Farman, 2008]. The reconstruction algorithm was applied using CTPro reconstruction software and then visualised using Avizo and Avizo Fire visualisation software.

A range of accelerating voltages and currents were trialled in order to achieve maximum contrast, definition and magnification.

Additional micro X-ray tomography was carried out using the Xradia Micro-XCT machine with the setting of 100 KeV, 10 w and 4.1 x magnification. This was only possible with small samples around 6 mm^3 at maximum volume that were prepared from the larger samples cut from the billet slice. The inspection involved a full 360° scan and acquired 723 projections. Data obtained by this technique was reconstructed using XM Reconstructer software and also visualised in Avizo visualisation software.

3.8 Tensile Testing

Tensile testing was conducted on a limited number of samples in order to determine the impact of defects on the mechanical properties of the material.

The dumbbell geometry tensile samples were machined from known defect containing region of the AZ80 alloy billet samples according to ASTM E8 standard [ASTM E8-11, 2011]. The samples were machines with a gauge diameter of 5 mm and a gauge length of 25 mm and tested on an Instron 5569, fitted with a 10 kN load cell and a cross-head speed of 1 $mm.min^{-1}$. The specimen was also fitted with a MTS extensometer with a gauge length of 10 mm for greater accuracy measuring strain during testing, preventing any equipment induced errors. The fracture surfaces were examined after failure to determine the presence of an inclusions using both optical and SEM microscopy.

3.9 Cooling Rate Experiments

To investigate the impact of cooling rate on intermetallic particle growth in AZ80, experimental castings solidified with different cooling rates were produced. The molten alloy, from an AZ80 production melt at Magnesium Elektron, U.K., was transferred using a ladle into a steel mould placed on a copper chill plate, a monolite ceramic block with a circular cavity and a sand mould with a circular cavity fitted with a BiMex sleeve. A control sample was taken at the same location as the

other samples and cast in the same steel mould as previously. Three different mould designs were used each constructed of different materials in order to achieve different cooling rates. The cooling rates were recorded using K-type thermocouples fitted to Almeno 2590 data loggers, recording the temperature every 1 second. Figure 3-4 shows the three moulds that were used for the experiment, each mould with a capacity of around 150 cm^3 – the capacity of the steel block being less.

The difference in size and geometry of casting was not important since the use of thermocouples gives a comparable cooling rate irrelevant of sample size. Two thermocouples were fixed in each mould as they were filled with molten alloy, one at the centre and one at the edge of the mould.

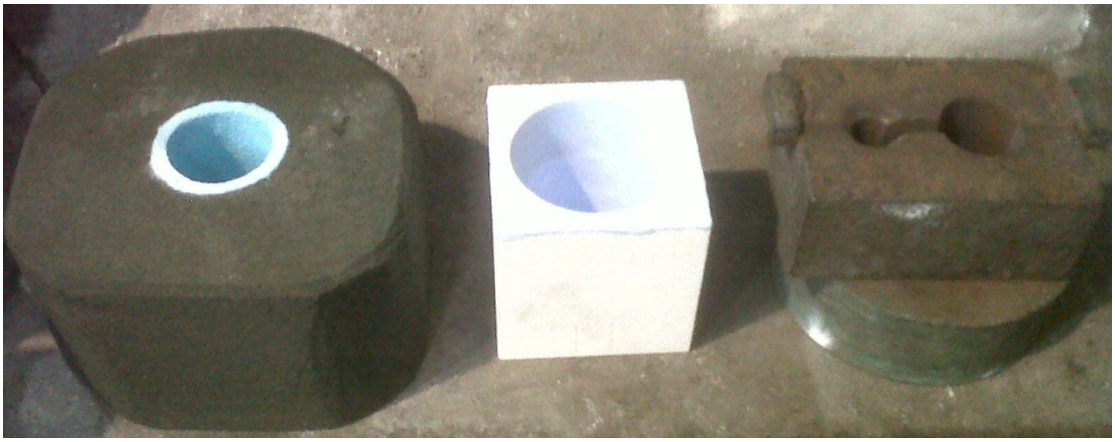

Figure 3-4 Photograph of moulds used for experimental castings; (left) sand, (middle) ceramic, (right) steel chill on copper block.

Samples were taken from a standard production melt as already solidified material would contain the intermetallic Al-Mn phase particles which might not be fully dissolved on reheating. Undissolved intermetallic particles would only coarsen further during solidification. The use of the industrially prepared casting melt provided the melt in the same condition as it would be when entering the mould.

The cast samples were sectioned and prepared for SEM inspection and analysis of the intermetallic particle size as described in section 3.5.2.

3.10 Melt Transfer Study

Samples of the melt during casting AZ80 alloy were extracted to assess the intermetallic particle content at various stages during the transfer of the melt from the crucible to the mould. Analysis of the intermetallic particle content in the different samples was completed to identify the change in particle levels during transfer. The transfer involved pouring the melt from the crucible into the launder in which it flowed with a free surface through filtering stages and weirs. The launder, with a T-shape geometry had two outlets, transported the melt approximately 2 meters at which point it fed the two DC casters. The flow was estimated to take 35 seconds to travel through the launder.

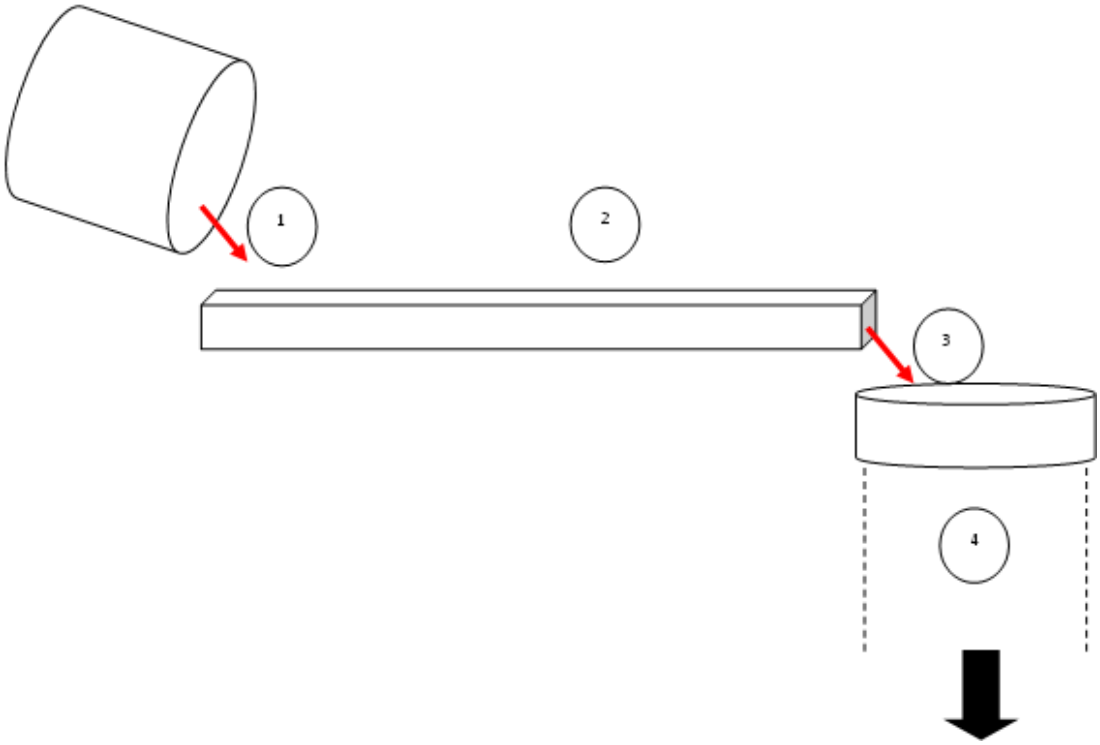

Figure 3-5 Schematic of casting arrangement showing crucible, transfer table (launder) and mould.

Samples were taken from four locations during the casting process, as shown in Fig. 3-5; position (1) the crucible containing the molten melt, (2) mid-way along the launder after the inline filter (approximately 1 meter from crucible), (3) immediately as the melt then enters the mould and (4) in the solidified material.

The samples, a 32 cm^3 volume of molten AZ80 alloy, were obtained using a ladle and cast in a steel mould on a copper base, apart from (4) where it was sectioned from the cast material. Once collected they were then prepared for optical microscopy and the particle content analysed as described in section 3.5.2.

3.11 Summary

A range of techniques both experimental and analytical were employed in order to accurately locate and characterise the material and defects produced during casting, plus techniques to enable an understanding how they form. The combination of established and novel techniques provided a suitable method for the needs of this study.

The defects positions in the billet were established using automated ultrasonic inspection which enabled the defect containing region to be removed. The slices then underwent full ultrasonic hand probe inspection and the identified areas removed from the slice. These samples were non-destructively inspected by XCT imaging and then mechanically prepared for optical and electron microscopy. A range of additional characterisation techniques were also used such as FIB, EDX and a range of analysis techniques.

Experimental castings were also produced under a range of conditions and analysed to enable the formation process of the defects to be studied.

4 Modelling and Simulation Methods

A range of computer modelling and simulation techniques have been used during this study. This section will introduce the techniques and software that were used to achieve this.

Computer modelling is increasingly being used as a cost and time effective approach to alloy and process development. A great range of software is available for these purposes and a number were employed in this study. This chapter will describe how JMatPro, Alsim and Matlab were used to provide the data and predictions for this study.

4.1 Thermodynamic Modelling

JMatPro 4.0 was used in the simulation of phase formation in AZ80 for both Scheil solidification and equilibrium cooling calculations. The Scheil simulation assumes that there is no diffusion in the solid, so that once a solid region has formed its composition does not undergo further change. Perfect mixing of solute in the liquid is also assumed. This approximation has been demonstrated to give a reasonably accurate representation of the real solidification behaviour during direct chill casting of light alloys.

The simulations were from a temperature of 700°C down to 100°C, with a step size of 5°C. The data extracted included the fraction solid, density, viscosity, phases present, composition of each phase and the composition of the liquid during solidification. This data was used in various applications including the microstructural analysis, fluid modelling and precipitation modelling.

4.2 Particle Nucleation and Growth Modelling

The precipitation of an Al-Mn intermetallic phase within AZ80 alloys is an important microstructural feature as they constitute part of the defects. Modelling the precipitation of the second phase was completed in this study in attempt to understand the formation of defects.

The formation of a second phase occurs in three distinct steps including nucleation, growth and coarsening during the solidification of the alloy. These three stages are thought to occur in AZ alloys when in the liquid state, prior to solidification commencing [Tamura et al., 2003]. This is as suggested by the phase diagram Fig. 2-5 and has been shown experimentally by producing rapidly solidified melt-spun ribbon in which the composition of the particles were all within the range Al_8Mn_5 [Thorvaldsen and Aliravci, 1992]. The formation proceeds until the material is completely solid at which point the elements needed to continue growing are locked into solid solution within the matrix, in this case primary α phase magnesium grains. Modelling of this process can indicate at which stage during solidification

most nucleation and growth of the second phase occurs, presenting useful data on how to prevent particle clustering and particles becoming associated with the defects to create large defects.

The Kampmann and Wagner numerical model (KWN), as discussed in section 2.4.3, provides a suitable technique to model and predict the evolution of the intermetallic phase particles during the solidification of an alloy.

For this study the required growth model was the interface controlled growth of spherical particles, assumed to be dispersed sufficiently as to be considered isolated in a perfectly mixed liquid, the growth rate, V, is given by [Kirkpatrick, 1975]

$$V = \Delta H_f \, d \, \Delta T / kT^2 \, 2r_c$$

Where ΔH_f is the driving force, ΔT is the undercooling, d is the particle diameter, k and T take their usual designation and r_c is the critical radius size.

The interfacial energy of the Al_8Mn_5 particles with the melt is unknown and is the only adjustable parameter in the model. This was determined by finding the best fit between the predicted and experimental results, as will be presented in the results section 6.1.1.

Modifications to the standard KWN model were made, as detailed above, to enable prediction for the AZ80 alloys system solidifying at different cooling rates. The modifications were made to the model code, written in MATLAB, such that the growth could occur during a specific cooling rate, the growth was of a solid in a liquid, i.e. interface controlled growth not diffusion controlled, and the necessary material constants for AZ80 alloy and the constituent elements were used, Table 5. The model was calibrated for the AZ80 alloy system by fitting with experimental data, the calibration process is discussed in section 6.1.1.

Material Constant	Value
Density of liquid AZ80	1790 kg/m^3
Concentration of Mn in Al_8Mn_5	0.38
Atomic weight Mg	24.31
Atomic weight Mn	54.94
Atomic weight Al	26.98
Initial Solute (Mn) content	0.12 wt%
Pre-exponential factor for Mn in liquid Mg*	$1.93x10^{-7}$ m^2/s
Activation energy for Mn in liquid Mg*	31 kJ/mol

*No data available for Mg, however Mg and Al have similar melting points therefore value for Mn in liquid Al used as data expected to be similar [Yong Du et al., 2003]

Table 5 Values used in KWN model for the AZ80 alloy system.

The model required to be modified to stop the simulation when all liquid present had solidified. This was achieved using the JMatPro predicted temperature at which complete solidification was achieved. JMatPro was also used as the source for data on the concentration of manganese in the liquid during solidification, Fig. 4-1.

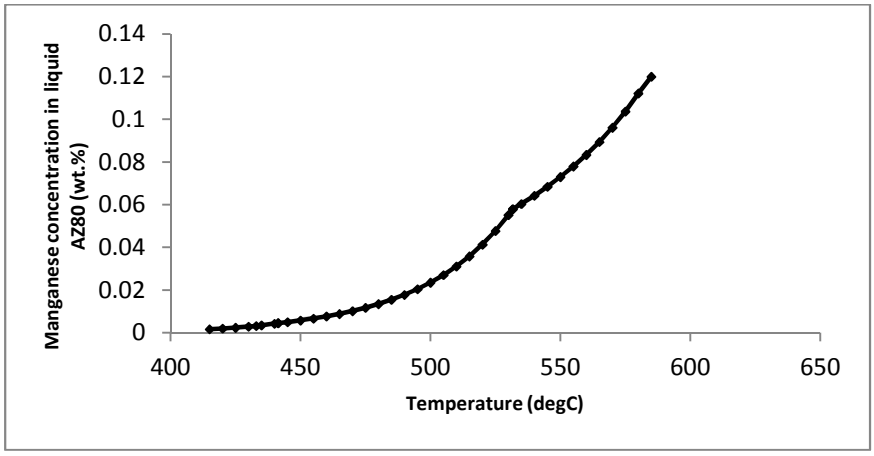

Figure 4-1 Manganese concentration in Liquid AZ80 during solidification [JMatPro].

4.3 Flow Modelling

A model to simulate the molten alloy flow during the transfer from the crucible to the mould was developed during this study using Alsim commercial software to improve the understanding of the flow regime within the casting equipment. The flow regime was the suspected cause of oxide formation influenced by insufficient filling and turbulence in the equipment due to changes in flow rates and equipment (launder) design. The Alsim software was employed as it had previously been used to model the solidification and casting process downstream, by Magnesium Elektron, U.K., with the intention to link to two models together for a complete picture of the casting process.

The Alsim models heat and fluid flow based on the continuum-mixture model for solid-liquid material [Bennon and Incropera, 1987]. It also uses the Boussinesq approximation to model the thermal convection occurring in the melt influencing the velocity of the melt [Mortensen, 1999]. The heat and fluid conservation laws are solved with a finite-element method and a fractional step approach (projection method) to solve the Navier-Stokes equations [Mortensen, 1999].

Model Parameter	Value
Casting speed (melt inlet velocity)	0.029 m/s
Latent Heat of Fusion	268 KJ/Kg
Casting Temperature	650°C

Table 6 Example casting parameters used in the Alsim fluid flow model.

For this study, a 2-dimensional model was developed with symmetry around the central vertical axis of the downpipe of the launder, Fig. 4-2(a). The model incorporated only a section of the launder and the downpipe with the moveable pin

at the top to control the flow rate. The boundary conditions applied to the fluid were free surface at the top, contained by the fixed walls of the launder (yellow Fig. 4-2(a)) and the pin (green Fig. 4-2(a)) and a constant inlet flow. No-slip boundary conditions were also applied to the solid walls in contact with the fluid. The flow was introduced immediately and the simulation was progressed until the flow had reached steady state, which was usually achieved within the first two seconds. The velocity of the flow was calculated from the inlet flow rate and the effect of falling under gravity. ALSIM assumes a fixed volume during simulation of the flow and hence free surfaces during filling and steady state flow can not be simulated. This however could be achieved using alternative software packages such as Flow3D.

The physical properties of the AZ80 alloy including the density, specific heat, thermal conductivity and fraction solid were entered into the model based on the values predicted by thermodynamic simulations using JMatPro over a range of temperature (150 – 700 °C), values given in Appendix 2. Additionally the casting parameters such as speed and temperature were also input into the model, values given in Table 6.

The mesh was built using PATRAN software, Fig. 4-2(b). The model typically took around 30 minutes to complete each simulation and the results were analysed in Ceetron, GLView Inova viewer.

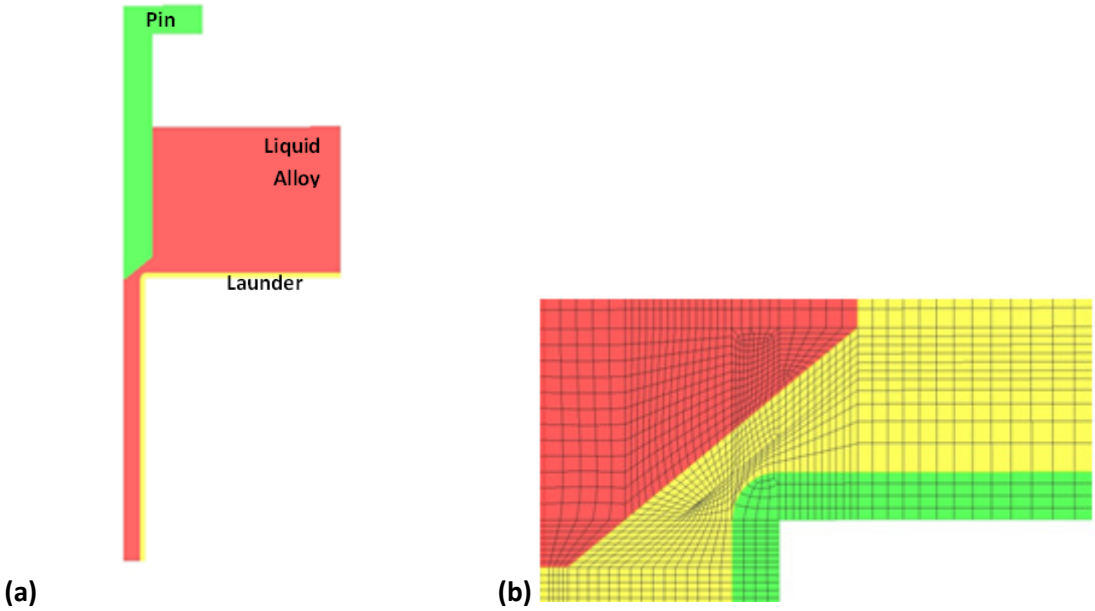

Figure 4-2 Mesh used to model flow through casting equipment, (a) showing components of model, (b) Demonstrating the mesh used in the region of interest.

4.4 Summary

Computational modelling and simulation techniques were used to develop a greater understanding of the processes involved in creating the defects in AZ80 alloy. Through the use of thermodynamic modelling, the precipitation kinetics controlling the growth of intermetallic phase particle can be better understood and how this process contributes to the overall defect formation. Flow modelling can provide an understanding of how the oxide film is generated and entrained, as fluid flow effects are known to be one of the main causes of oxide film entrainment [Campbell, 2006]. Fluid flow can also indicate the mechanism by which the two inclusion types, second phase particles and oxide films, become associated in the molten alloy and result in large defects in the cast product.

5 Defect Location and Characterisation

This chapter will discuss the results obtained during the characterisation of the AZ80 alloy and defects, including a defect in a zirconium containing magnesium alloy. Knowledge of the typical alloy microstructure is essential to enable identification of the defects present.

A range of techniques were employed to characterise the microstructure and the defects including, optical microscopy, SEM, FIB, ultrasonic inspection and XCT. The outputs from these techniques were a comprehensive understanding of the microstructure and the defects contained. Additionally this work has provided information on the suitability of the novel use of XCT for this type of study.

5.1 Characterisation of Initial Microstructure

Alloy samples were sectioned from a large DC cast AZ80 billet in the homogenised condition. The billets, 480 mm diameter and 4 m in length, had been homogenised at 400°C after casting to remove the effects of segregation and then scalped to remove any surface defects. The homogenisation treatment would dissolve any low melting point eutectics present but would not have any effect on the Al_8Mn_5 intermetallic particles present in the alloy.

The grain size and intermetallic particles across the billet diameter were characterised by taking four samples across the billet radius, Fig. 5-1. The four samples (a) – (b) were taken at a distance of 1.5 cm, 6 cm, 9.5 cm and 15 cm from the billet surface respectively, and correspond with the four micrographs in Fig. 5-2. The typical as received microstructure is shown in Fig. 5-2(a), consists of primary α-Mg grains and a eutectic structure of α-Mg and β-$Mg_{17}Al_{12}$, the eutectic structure shown more clearly in Fig 5-3. Particles of an intermetallic phase, Al_8Mn_5 are also present in the microstructure, these are observed as dark spots in the microstructure, Fig. 5-2.

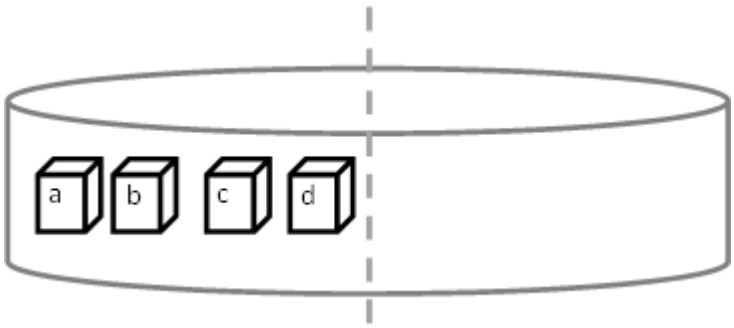

Figure 5-1 Schematic of sample positions across billet section.

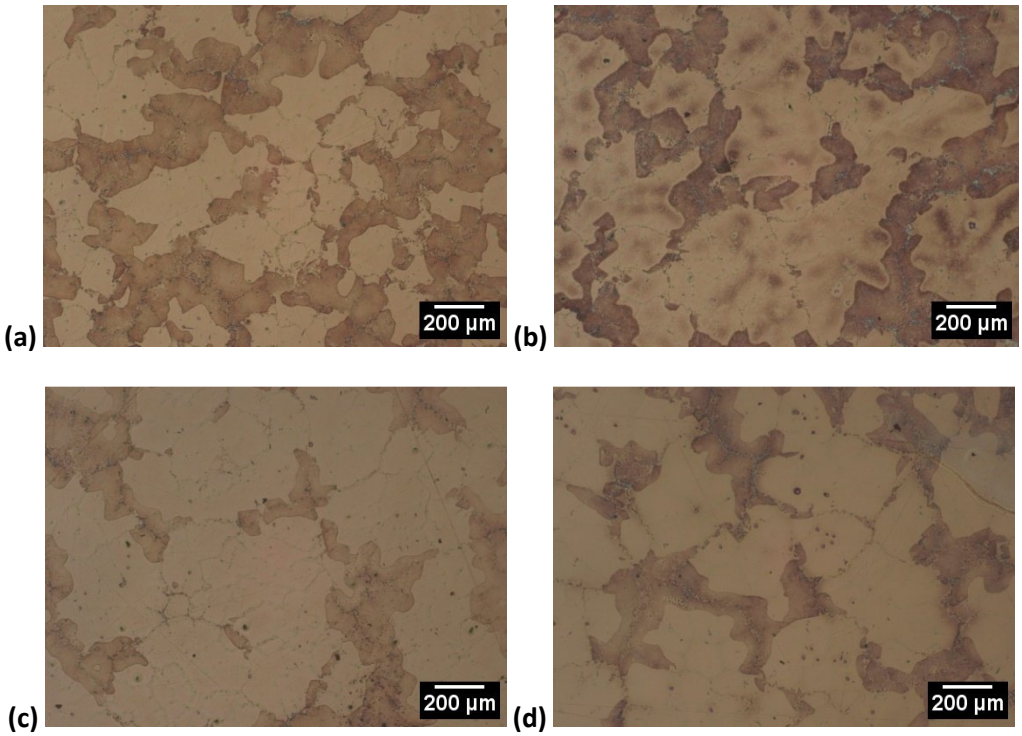

Figure 5-2 Homogenised AZ80 etched microstructure across billet. Images captured at (a) 1.5 cm, (b) 6 cm, (c) 9.5 cm and (d) 15 cm, from billet surface.

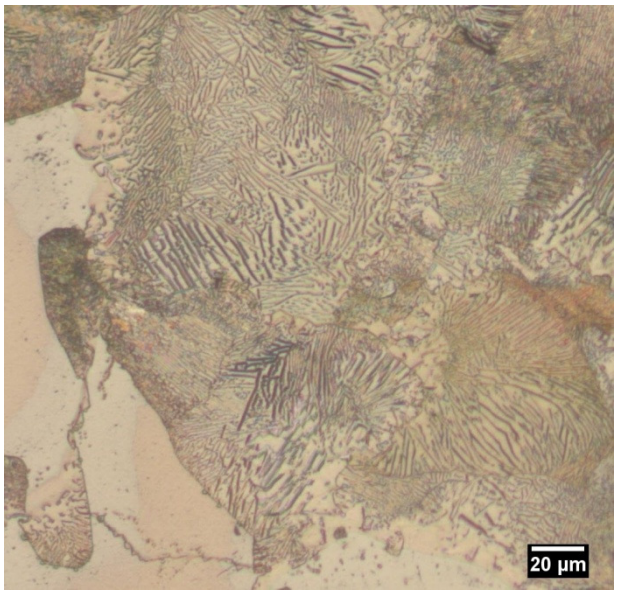

Figure 5-3 High magnification optical micrograph of eutectic structure observed in AZ80 alloy.

5.1.1 Grain Size

Optical micrographs, Fig. 5-2, show the presence of equiaxed grains at all sampled locations within the billet. There is an increase in grain size from the billet surface towards the centre, Table 7.

	Grain Size(μm)	Standard Deviation
Sample 1 (surface)	137	60
Sample 2	126	34
Sample 3	171	48
Sample 4 (centre)	168	55

Table 7 Grain size across billet radius.

The grain size generally increases towards the centre of the billet, however a small reduction in grain size was measured between the billet surface and positions immediately next to it. These grains are thought to be due to the effect of the secondary cooling where the water jet hits the billet as it emerges from the mould, this creates large amounts of heat extraction [Eskin et al., 2004].

The measured grain size trend reported in this work corresponds with the reported grain size across a typical DC cast aluminium alloy billet, Fig. 5-4 [Eskin et al., 2004]. The presence of smaller grains immediately next to the surface is also present, however the grain size only varies by a small amount across the entire billet radius.

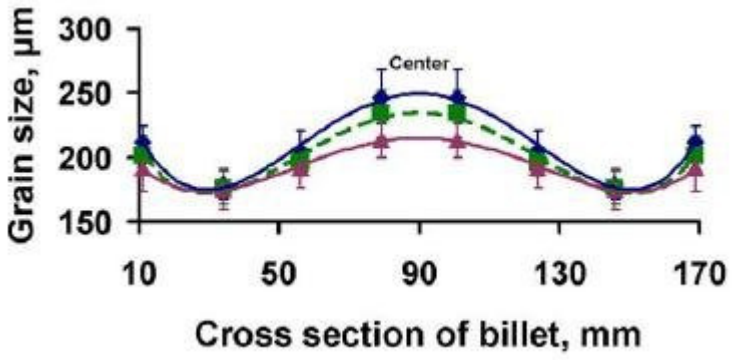

Figure 5-4 Distribution of grain size across the diameter of a DC cast billet for different casting speeds [Eskin et al., 2004].

5.1.2 Particle Size and Distribution

Figure 5-5 shows the change in intermetallic particle size, measured as equivalent circular diameter, and Table 8 shows the increase in the number of particles across the billet radius. This trend is evident in the micrographs, Fig. 5-2; there is an increase in particle size and number of particles towards the centre.

Sample Number	Number of Particles per mm^2	Area Fraction Particle
1	86	0.00118
2	77	0.00187
3	96	0.00179
4	119	0.00342

Table 8 Number of intermetallic Al_8Mn_5 particles present per mm^2 and area fraction across the billet radius.

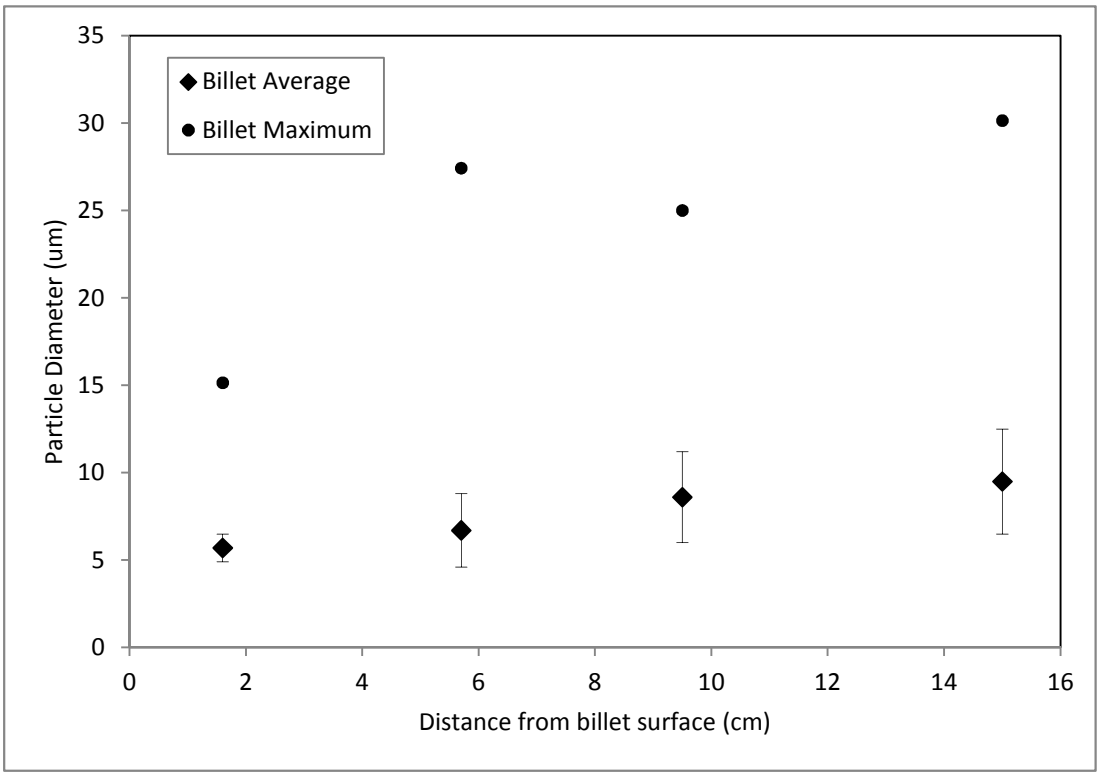

Figure 5-5 Particle (Al_8Mn_5) size measured across billet radius.

The intermetallic particles are present both within grains and at the grain boundaries throughout the microstructure. The maximum particle size at the centre of the billet is double that measured at the edge, Fig. 5-5. The composition of this phase was determined by EDX analysis, Fig. 5-6, assuming no magnesium in the particle, as is expected from the phase diagram. All particles analysed were of similar composition Al_8Mn_5. This is the expected stoichiometic composition for the manganese phase in this alloy [Sin et al., 2007]. Some of the particles were found to contain iron, which directly replaces the manganese in the particle. The intermetallic particles observed in this study were consistent with those reported for the AZ80 alloy system [Ye et al., 200; Fan et al., 2010, Fan et al., 2009, Shukla and Pelton, 2008, Sin et al., 2006].

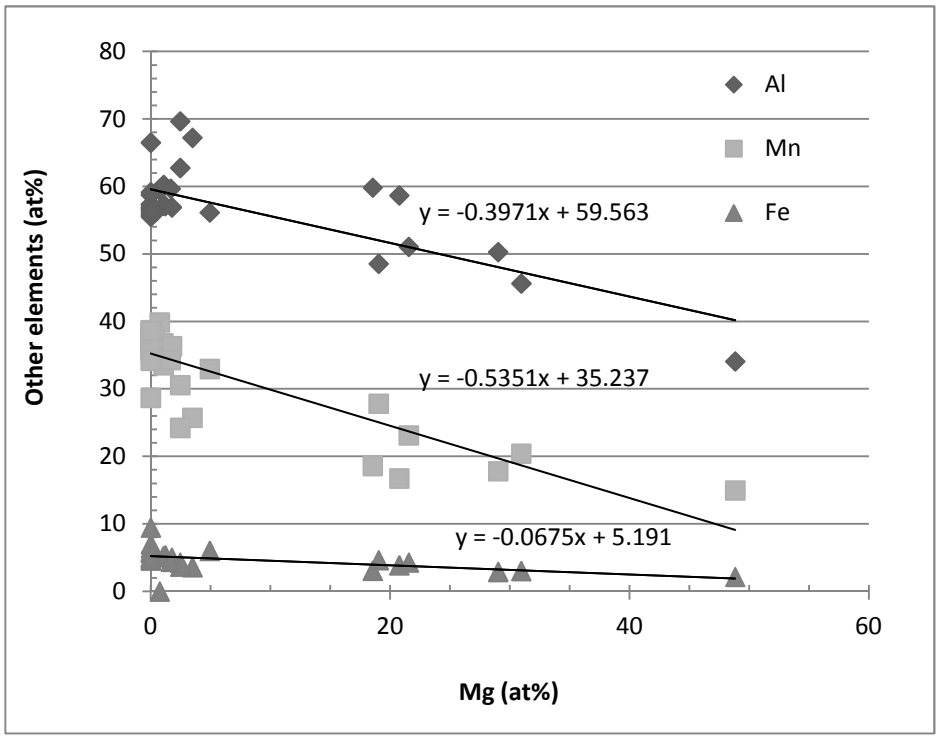

Figure 5-6 EDX results of intermetallic phase, normalised against magnesium content.

The morphology of the particles was observed to be either spherical or needle like, which is consistent with published observations [Sin et al., 2006]. The range of particle sizes was measured to be between 0.1 – 30.5 µm in equivalent circle diameter. The particles were observed to be touching which may suggest sintering between smaller particles, Fig. 5-7, particles in contact were more prevalent towards the centre of the billet where the particles are also more rounded.

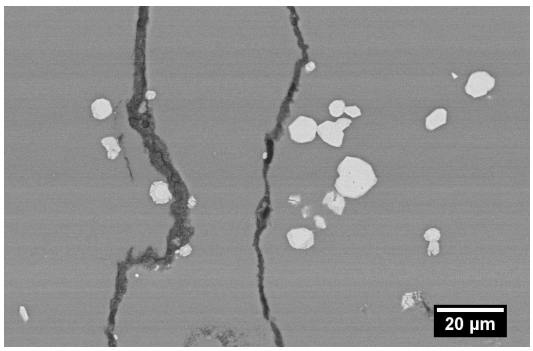

Figure 5-7 SEM of defect in AZ80 showing section of entrained oxide film and associated intermetallic particles (Al_8Mn_5).

Validation of the measured intermetallic particle composition was achieved by thermodynamic modelling of AZ80 system using JMatPro for the solidifying alloy. The simulation was based on the Scheil assumptions, most accurately replicating

the solidification process of DC cast AZ80. These simulations predicted the presence of Al_8Mn_5, Al_4Mn and $Al_{11}Mn_4$ phases, Fig. 5-8. Only the Al_8Mn_5 phase was detected as being present in the AZ80 alloy used in this study.

The distribution of the intermetallic phase particles was analysed using the Voronoi Tessellation Technique [Murphy et al., 1997]. The analysis was carried out on the homogenised microstructure of the AZ80 alloy, from ten random locations within three different samples. The analysis provided the average area of cell size grown around a particle for the distribution observed in the microstructure. The average cell size was found to be 0.04 mm^2. This data is to be used later in the study to compare with the average cell size calculated for a defect containing sample to highlight the presence of clustering. However, this technique will not provide a true measure of clustering and is highly dependent on the images used in the analysis.

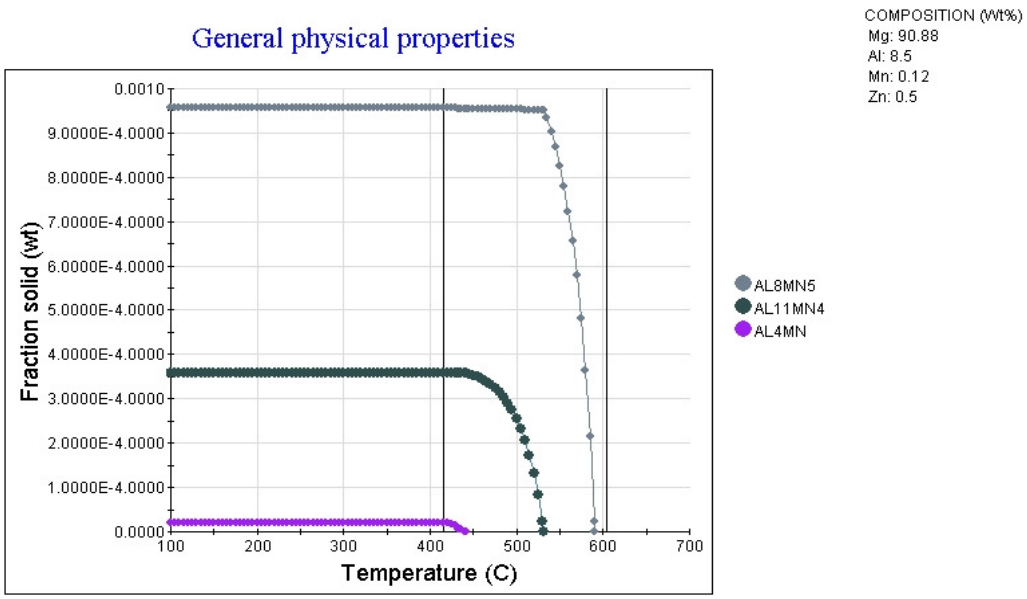

Figure 5-8 Predicted volume fraction of phases present in AZ80 alloy, after Sheil solidification process (produced by JMatPro).

5.2 Ultrasonic Defect Location

In an industrial setting the quality of a cast billet is assessed by the employment of immersion ultrasonic inspection, typically an automated process coupled with software to record the responses. This technique is suitable for the detection and location of defects however provides limited information on the properties of the defect.

This section will present the findings of this study which aimed to locate defects in the billet using ultrasonic methods and to assess the suitability of this technique for this application. It was also intended to enable optimisation of the current practice and increase the level of confidence in the scan results reducing the amount of sub-standard material entering the retail stock or being rejected. A final objective was to characterise the defects located by the equipment, and identify what information can be interpreted from the responses received.

5.2.1 Ultrasonic Equipment Calibration

Ultrasonic inspection probes and detectors require calibration before use. This involves the use of a calibration block, as described in section 3.3.1; manufactured as prescribed by the relevant standard. By doing so the probe parameters, in terms of the power and frequency of ultrasonic pulses along with the gain, are established for maximum accuracy. The established parameters are then applied when inspection of a billet is carried out. The current configuration was deemed to be an area of ambiguity and a poor understanding of the process existed limiting the quality and confidence in the results produced.

The transfer difference parameter enables the user to enter a value that will modify the gain setting to account for small variations between the calibration block and the billets that are to be inspected. Variation can occur due to different surface roughness, grain size and structure and small differences in billet diameter between the calibration block and the billet; these all impact on the probes performance. The inspection equipment software enables the user to enter the transfer difference before scanning or to be entered manually as an adjustment to the gain

setting. By completing a repeat scan of the same billet the impact of entering the value by the two methods was assessed.

Additionally the inspection software also enables the user to apply post scan filters to the data from each scan. The addition or reduction of gain could be applied to the scan results. The effect of this operation was unknown and was identified as having a similar effect to the transfer difference. Changing the gain levels by this post scan method until no defects were visible was thought to demonstrate the proximity of a defect to being acceptable.

A scan completed with a transfer difference of 3dB, Fig. 5-9 (a), detected two defects above acceptable values and required a further reduction of 3dB by the post scan gain filter to remove all defects. The same level of filtering was required to be applied for the scan without any transfer difference entered to remove all defects, Fig, 5-9(b). This indicated the two methods of achieving a transfer difference are not acceptable alternatives and the transfer difference must be entered correctly.

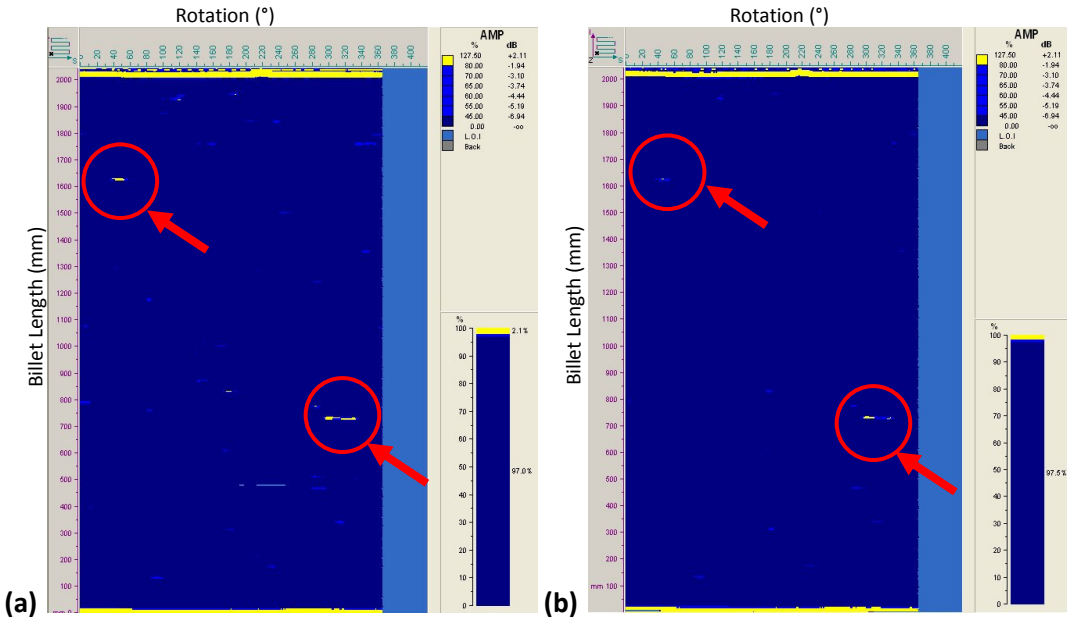

Figure 5-9 Comparison of transfer difference used for ultrasonic inspection, (a) with 3dB transfer difference, (b) No transfer difference used.

The use of the post scan gain filter can be applied to remove the defects to such a level that none were visible. However this also removed the response from the machined holes (significantly larger features) at the billet end, Fig. 5-10(c). This test

established that the post scan gain filter should not be used and was not a reliable method to assess the defect with regard to the acceptable level or to establish its size.

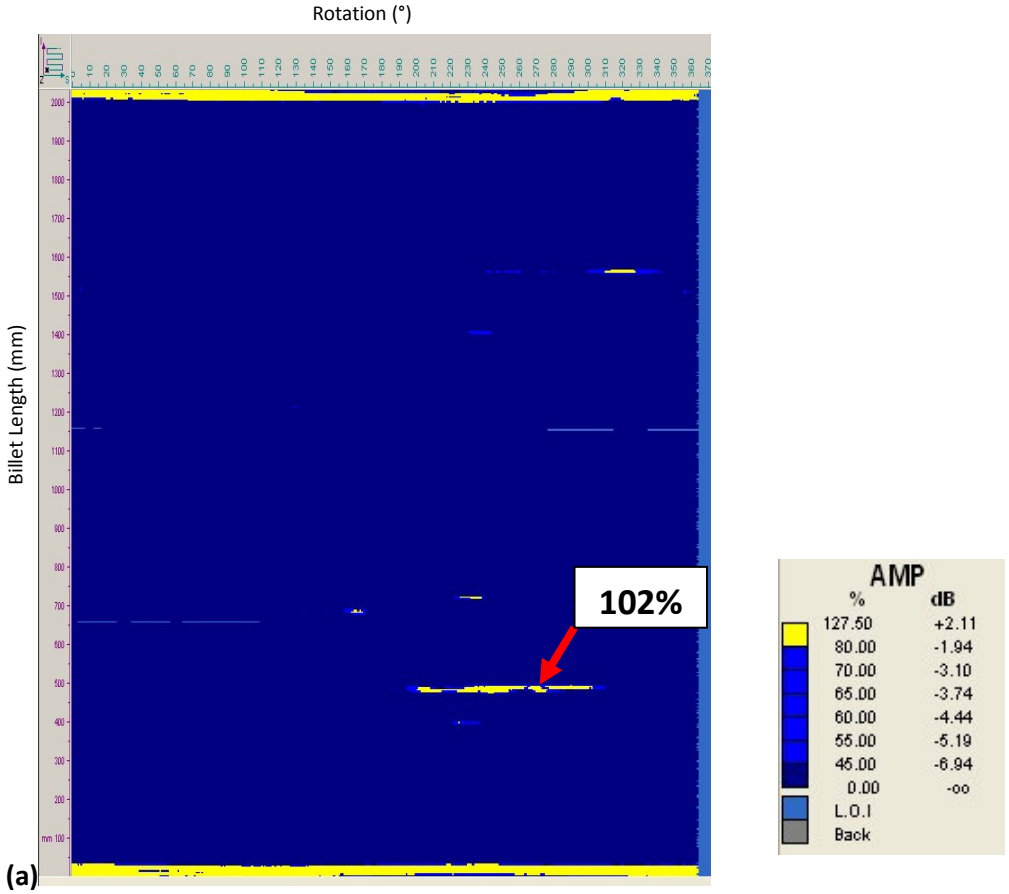

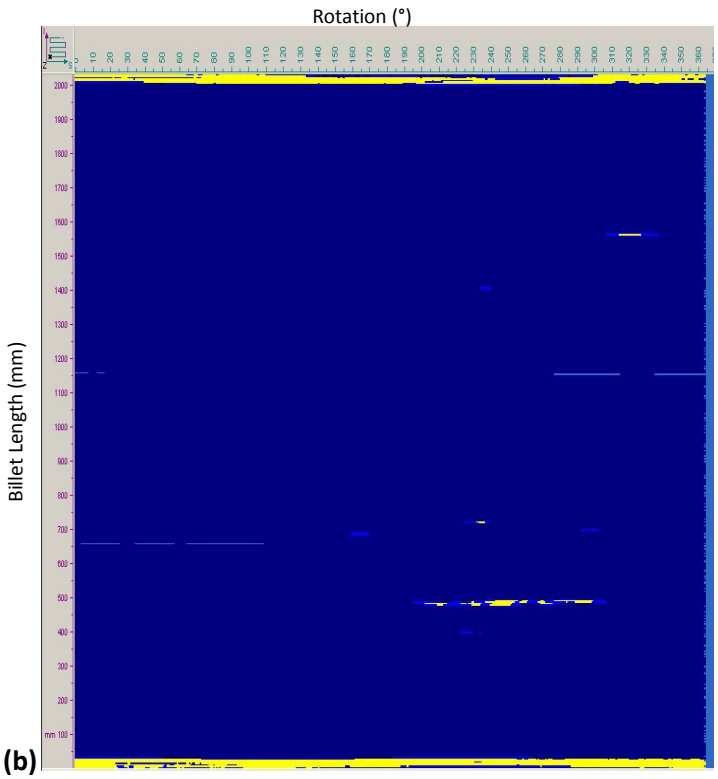

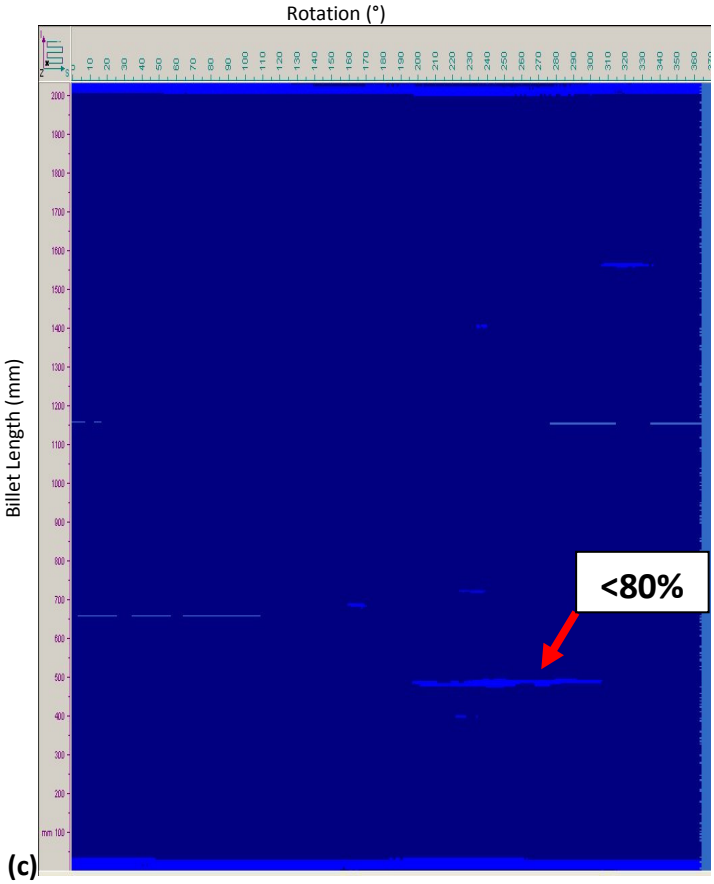

Figure 5-10 Ultrasonic response maps with various post scan gain filtering applied, (a) no gain reduction, (b) -2.0dB gain reduction, (c) -2.5dB gain reduction resulting in unacceptable size defects including machining holes (N.B. Legend in (a) applies to all plots

This work has shown that the impact of the transfer difference and post scan gain filtering are different and cannot be used interchangeably. Correct choice of transfer difference is the proper method of adjusting gain to account for variations between the calibration block and the DC cast billet and that the post scan gain filtering is not a suitable method to assess defect size. With the correct configuration the automated ultrasonic inspection method can be considered a reliable inspection method.

5.2.2 Automated Inspection

Ultrasonic inspection provided the location of defects in terms of the position along the length of the billet and respective location on surface in terms of the degree of rotation from a location indicated by a yellow marker, Fig. 5-11. There is no information on the depth of the defect from the billet surface or the defect size.

The typical response was a horizontal line across the response map, yellow in Fig. 5-11. The response indicates that a defect was detected at each of these locations on the billet surface, however this is known to represent continued detection of the same defect as the billet is rotated in front of the probe. The length of the response line was shown to bear no resemblance to the size of the defect from which the response signal was produced. It is thought that longer horizontal response lines indicated a defect further from the billet surface as this would result in the defect residing in region of inspection for longer, those closer to the surface would pass across the inspection region quicker.

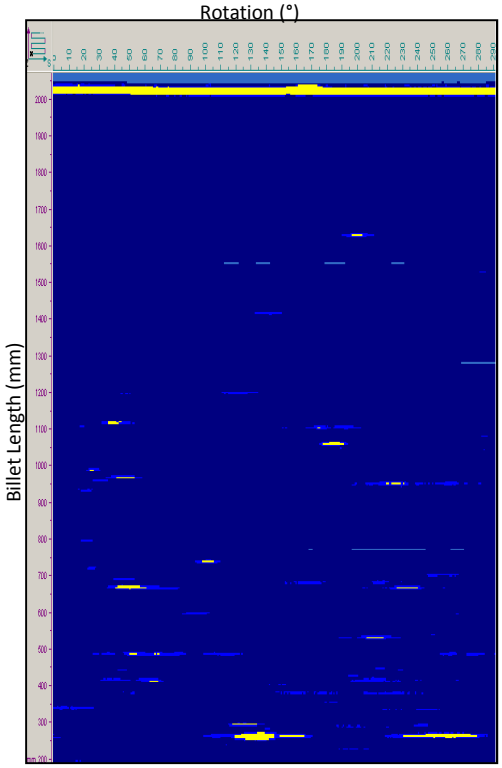

Figure 5-11 Map of ultrasonic responses across entire billet surface. (Yellow indicates critical sized defects in internal structure, X-axis – billet rotation, Y-axis – billet length).

The defect depth was interpreted from the response when the probe was repositioned over the defect. This depth was compared with that measured in the actual billet, Fig. 5-12. The measured and interpreted depth matched exactly and did so when repeated for a number of defects. The inspection software does not automatically generate this data, however doing so does enable much more accurate defect location. This method does not permit interpretation of the defect

size due to the complex nature of the defects; sizing would only be possible if sufficient prior knowledge of the defect existed.

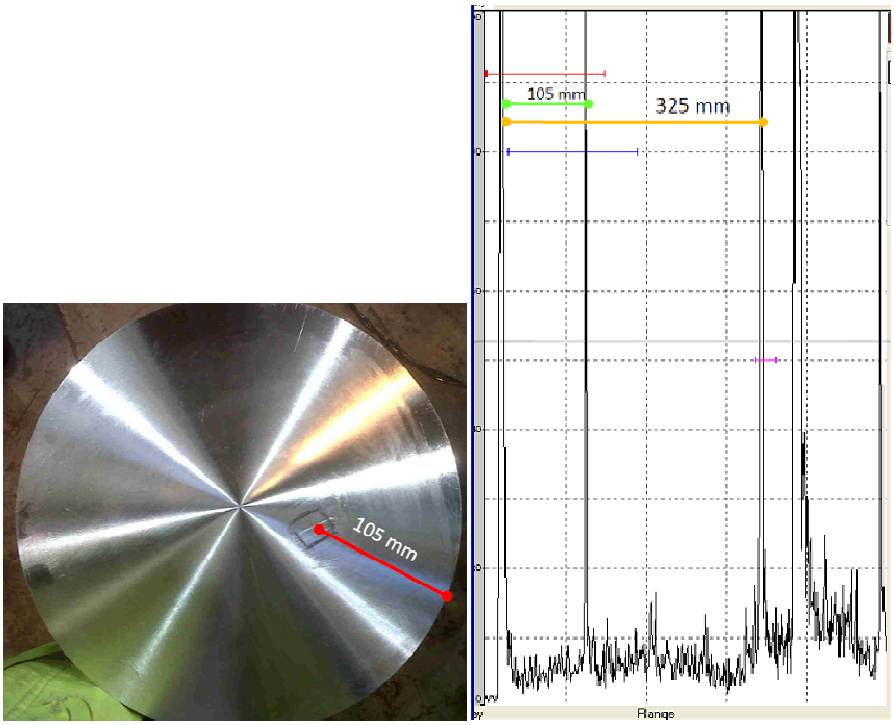

Figure 5-12 Matching of interpreted defect depth from ultrasonic data to that measured in billet.

Defects can be more effectively removed from a billet when the depth is known. Collating the depth of defects in a number of billets, Fig. 5-13, demonstrated a strong trend in their locations. All defects were found to be present in a central region, within a distance of half the radius from the centre. Samples from out with this region indicated to contain a defect by the ultrasonic hand probe were inspected with the same rigour as those from within this region and were all shown to be void of any defect. The occurrence of erroneously identified defect locations was due entirely to the ultrasonic hand probe and only occurred when it located more than one defect site on a billet slice, thus full confidence in the automated ultrasonic inspection was maintained. This trend in defect location begins to indicate the mechanisms that are resulting in defects in the casting, which will be discussed further in section 6.3.

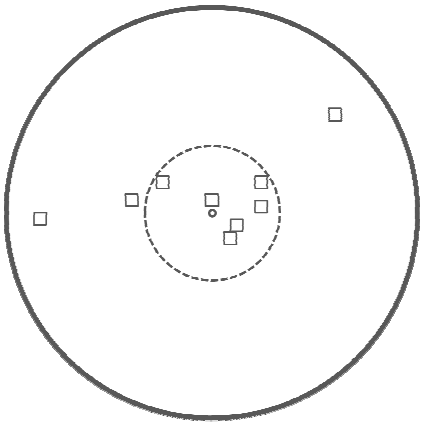

Figure 5-13 Schematic of billet with multiple defect positions superimposed, only those samples within the dashed circle contained defects.

Ultrasonic response data provides the producers with quantitative information on the cleanliness of the billets being produced by the current casting methods. This can be computed for the individual billet or averaged over a production schedule. Figure 5-14 shows the scan data for an individual billet inspected to the equivalent AA standard [SAE AMS-STD-2154].

The dark blue fraction represents the percentage of the material scanned which was acceptable, the lighter blue indicating a small response was detected, below the pre-set threshold, and the yellow indicating the percentage of material which generated a response above the acceptable limit. From the scan, Fig. 5-11, around 5% of the material was identified to contain a defect above the acceptable limit. This does not indicate the amount of usable sections or the account for the ends of the billet which contains machining holes and stampings, known defects. The value of this overview of the billet quality level suggested that one billet was always cleaner than the other, when cast in pairs. This observation indicated the cause of the defects was due to the handling of the individual flows as they enter the mould, as discussed in detail later.

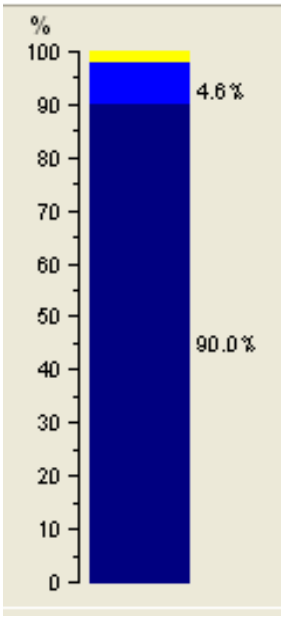

Figure 5-14 Quantitative analysis of cleanliness of a billet, direct output from inspection software.

5.3 X-ray Computed Tomography Imaging

Ultrasonic inspection only indicated the presence of defects in the casting providing no information on their size, composition, morphology or orientation. X-ray Computed Tomography (XCT) provided a non-destructive, higher resolution imaging solution and was employed in this study to better characterise the defects. This section focuses on the ability of the XCT technique to characterise these defects and the outcome of the characterisation attempts.

5.3.1 X-ray Computed Tomography Capabilities

Initial attempts were made to better understand the ability and limits of the XCT equipment to image AZ magnesium alloy samples. An entire AZ80 billet section 32 cm diameter and 4 cm thick was imaged using the Nikon Custom Bay at the University of Manchester, Fig. 5-15. High power X-rays, 320kV, were required to ensure penetration of the complete sample and sufficient levels of detection by the detector. The use of high power X-rays resulted in a small signal to noise ratio preventing the detection of any internal detail. An attempt was made to reduce this effect by the use of a 3.6 mm thick copper plate to filter the X-ray beam, which had little impact. Also limiting, was the very low magnification achieved, necessary to ensure imaging of the entire sample was achieved. Magnification was reduced to such a level that the defects present fall below the resolution of the scan (1 mm) and thus were not imaged.

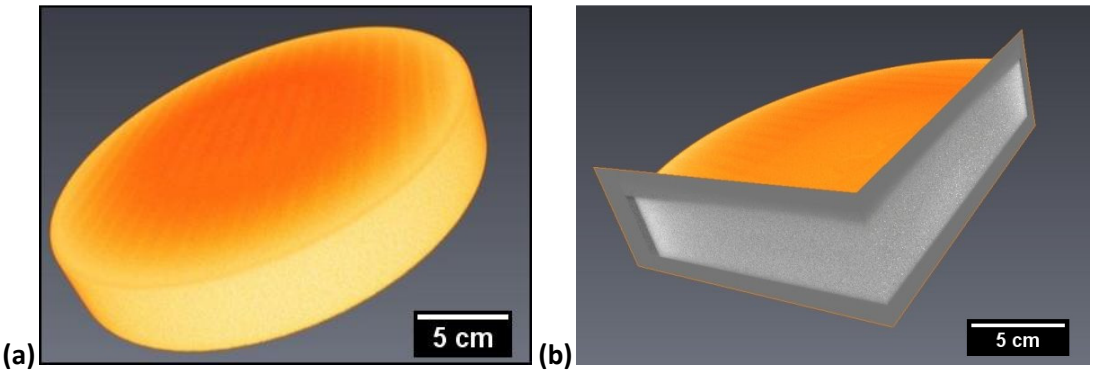

Figure 5-15 Reconstructed XCT image of complete billet section, (a) complete slice, (b) orthoslice applied revealing internal structure.

The results of this scan informed the future imaging methods by XCT for this study and indicated that smaller samples must be used for the XCT imaging to be successful.

A second attempt was made to use the XCT technique to image a smaller, 2 x 2 x 2 cm, sample of the same material, Fig. 5-16(a). It was possible to identify the intermetallic particles based on the contrasting greyscale values allocated to the voxels and the surrounding matrix in the reconstructed 3D volume. The resulting images successfully showed the presence of the intermetallic phase particles, Fig. 5-16(b), the resolution of 5.76 µm was achieved, indicating that all samples to be imaged in the future must be of a similar size or smaller.

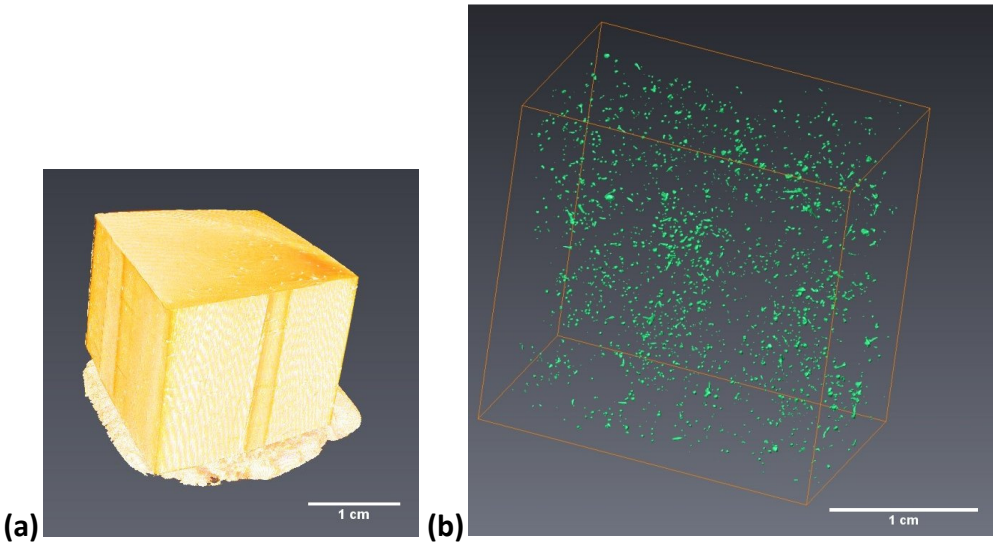

Figure 5-16 XCT imaging of AZ80 sample (a) complete AZ80 cube sample (on mounting putty), (b) AZ80 cube sample with matrix removed to show intermetallic particles.

A third scan was carried out of an AZ80 sample known to contain a defect, as indicated by ultrasonic inspection. Figure 5-17 shows a single reconstructed 2D orthoslice extracted from the reconstructed scan image. The intermetallic particles are visible as small rounded white regions, indicating their higher relative density, the entrained oxide film visible as a dark region, demonstrating the lower relative density and the grey magnesium matrix background. The defect size and morphology is also determinable by this method. This demonstrated that a defect could be successfully imaged, that sufficient contrast and acceptable resolution can be achieved.

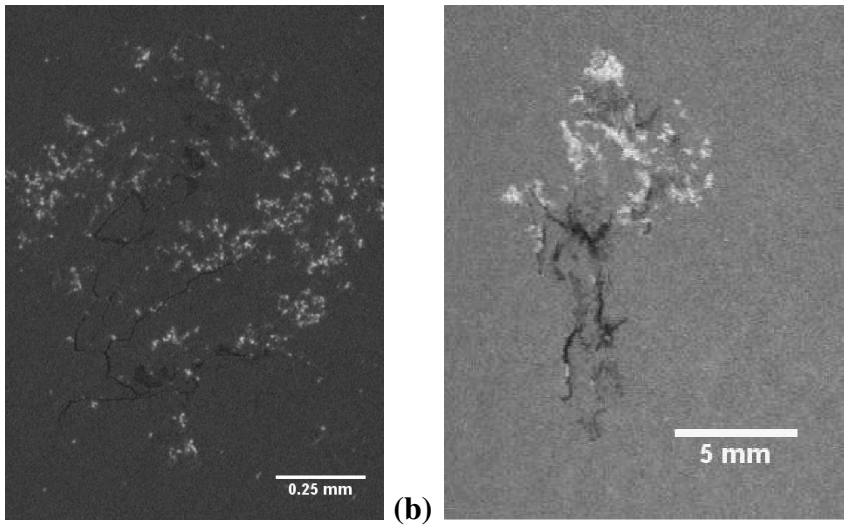

Figure 5-17 Reconstructed slice through a defect containing AZ80 sample.

The initial XCT scans identified this as a suitable complimentary technique to ultrasonic inspection. They also demonstrated that XCT would provide further information on the defects to assist in characterising them fully, in a non-destructive manner. The rest of the results in the section were informed by the findings of these three scans.

5.3.2 X-ray Computed Tomography Defect Imaging

XCT imaging demonstrated that the crack like phase, as observed in 2D, Fig. 5-17, was actually a continuous defect throughout the volume of the sample imaged. Observed isolated regions of intermetallic particles, as imaged by SEM or optical microscopy, were seen to be connected by the continuous film like defect, often very branched and complex in shape. This represents an improvement in terms of characterising the defects, revealing the true morphology and relationship between the two phases which comprise them.

The entrained oxide films are large and are often observed to be fragmented at various locations across the 2D image, Fig. 5-17. This may be a direct reflection of the defect's structure but may also be due to the limited resolution of the XCT imaging technique. This size, morphology and fragmented nature of the defect were more apparent when the 3D surface was "grown" using the analysis software, Fig. 5-18. The imaging software automatically grows the connected regions by grouping neighbouring voxels with similar greyscale values, within a defined range,

into a complete surface. The result is a large film like inclusion, which is often planar or folded into a more compact defect. This is suggestive of the entrained oxide films which have experienced furling and unfurling as suggested by Campbell [Campbell, 2006].

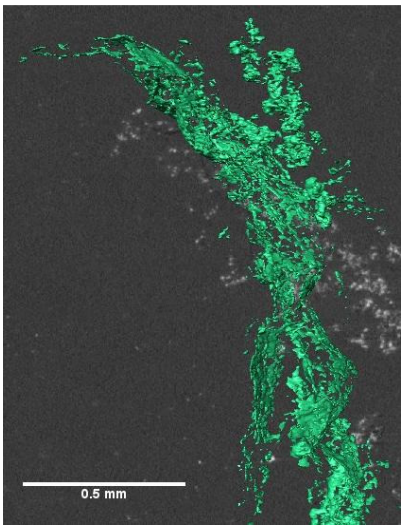

Figure 5-18 3D Surface of entrained oxide film created in Avizo visualisation software.

The presence of fragmented films can be the result of both limited resolution and contrast between the defect and the matrix. However entrained films can fragment as they experience turbulence [Campbell, 2006] in the flow of the molten alloy. The problem of resolution cannot always be overcome as the geometric magnification requires that the field of view is large enough to capture the entire defect. These defects were observed to be very large, often 0.5-5 mm in length, yet some of the features were as small as 2 µm.

The presence of the entrained film was observed as a filled crack, which exhibits a much lower contrast between defect and matrix than an air filled crack. When combined with the limited resolution, regions of the entrained film were not imaged, resulting in a fragmented film not representative of the actual defect.

Growing the 3D region of the intermetallic particles follows the same method as that used for the entrained film. Segmenting the particles was significantly simpler due to the large contrast between the surrounding Mg matrix and the particle greyscale values and simpler morphologies, resulting in better interface definition,

Fig. 5-19. The only limitation was for very small particles, which suffered from the same problems due to the resolution.

Although sintering was observed by the optical microscopy and SEM techniques, an excessive abundance of this type of agglomeration was observed in the XCT images. This suggests the growing of the 3D regions merged many of the particles erroneously. Small artefact particles can also be created during the segmenting process as a result of noise in the original data.

The result of the XCT imaging was to enable the visualisation of the entire defect in 3D, Fig. 5-19. Both phases are visible, exhibiting clearly their relationship to each other. It is also possible to characterise their size, morphology and abundance, due to the non-destructive manner by which imaging was achieved.

Clustering of the intermetallic particles can be observed to be prevalent in a typical defect found in AZ80 alloy. This was true for all defects found by the methods followed in this study. The clusters were observed to be next to the entrained film, Fig. 5-20, but very few were in contact. More noticeable was the observation that in the material immediately neighbouring the defect the particle distribution returns to that measured in any other region of the billet. This suggests that there is an association between the clustering of the particles and the presence of the entrained oxide film.

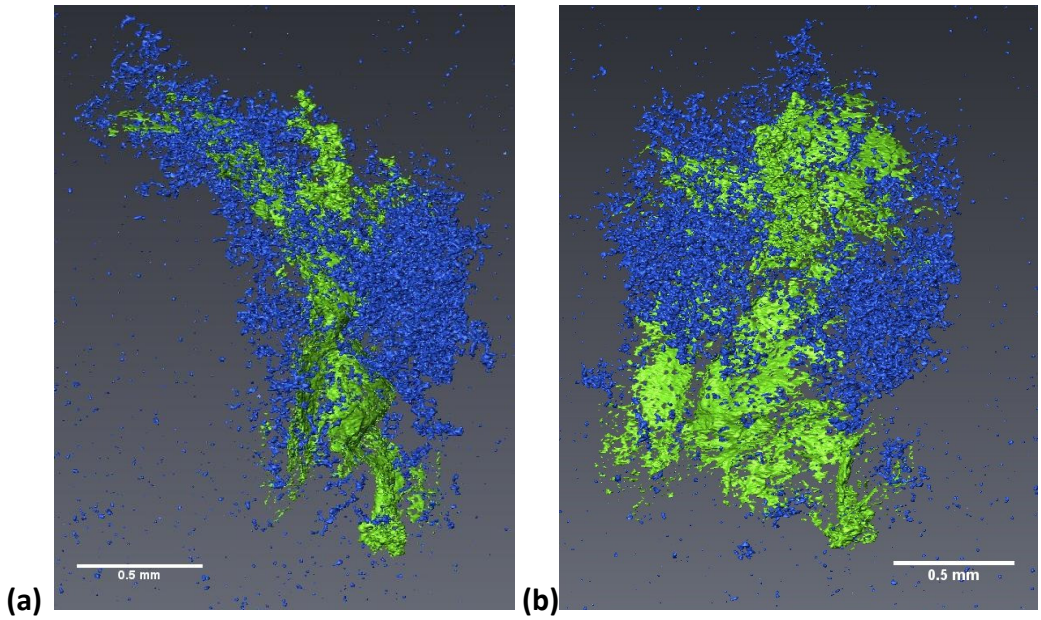

Figure 5-19 3D visualisation of defect (green – entrained oxide film, blue – intermetallic particles) with Mg-matrix removed for clarity, (a) XZ plane, (b) YZ plane.

XCT imaging also enables the size of the defects to be determined accurately. 2 dimensional techniques limit this analysis since the third dimension could not be assessed. Defects of this type found in AZ80 alloy ranged in size (longest characteristic length) from 0.5 – 5 mm. The aspect ratio could also be determined, which influences the stress concentration effect that a defect may exhibit and thus its influence on fracture toughness. The aspect ratio of some defects (focusing on the entrained oxide film) was 2:5000, demonstrating the morphology of these defects (long and thin) is potentially very damaging to the mechanical properties since depending on the orientation with respect to the loading direction such defects could induce a high level of stress concentration [Sajuri et al., 2006].

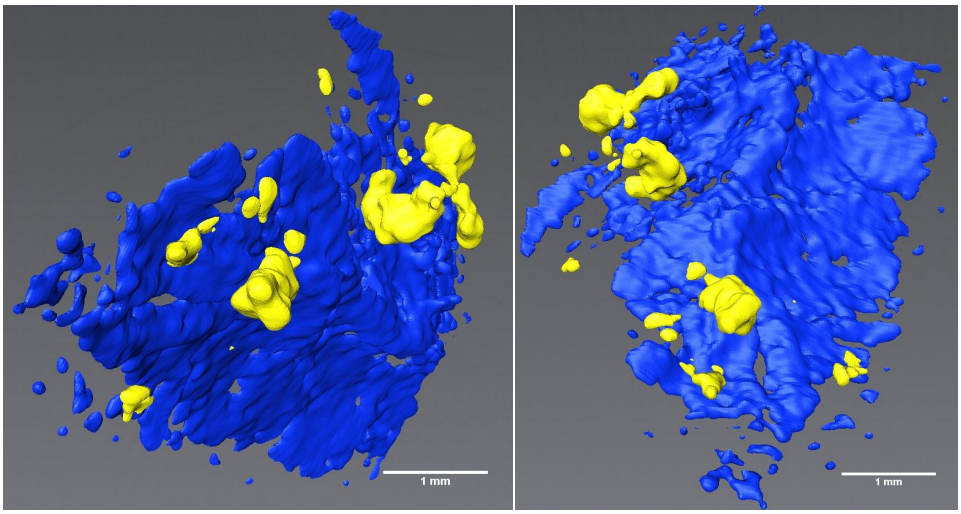

Figure 5-20 Enlarged 3D defect XCT images.

The observation from the XCT images confirms that the particles are only near or on the surface of the oxide film and not did not demonstrate wetting along the particle/oxide interface, confirming the observations made by 2D imaging. However, any voxel can only be allocate a single grey scale value thus those at the interface will only represent a single phase which is not accurate. Therefore, this aspect was studied in greater detail using SEM imaging.

A number of the samples contained not a single defect as indicated by the ultrasonic response but a small grouping of oxide fragments, Fig. 5-21. The group of films were not connected and were actually separated by a distance similar to their own size. This fragmented group of entrained films does not have the same volume of intermetallic particles associated with them, however small clustering of the particles can still be observed within the vicinity. Each fragment was smaller than the films that were observed as complete, however it appears that they were once one large film which has since been broken up. It is highly unusual for such a strong grouping of entrained films and was not observed anywhere else. The response generated from the ultrasonic inspection demonstrated that even this type of defect is detectable, however it could not be discerned from a single larger defect on this response alone.

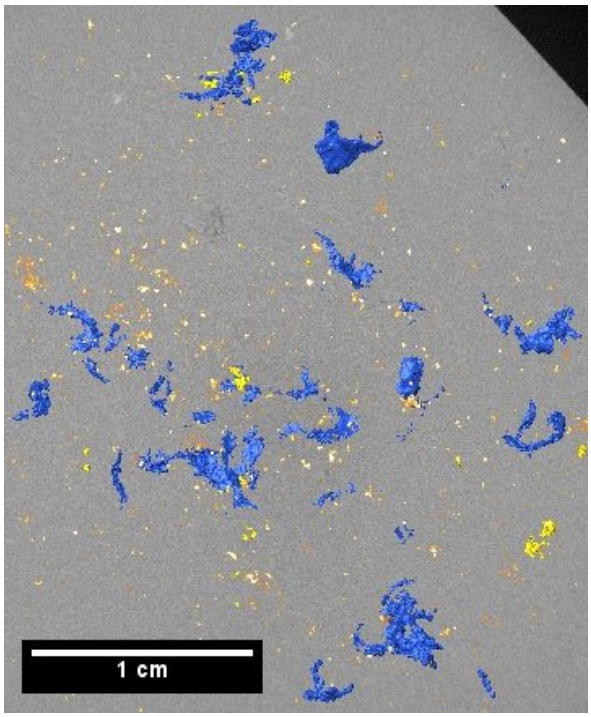

Figure 5-21 XCT image of group of entrained oxide films and particles.

5.4 2-Dimensional Inspection

5.4.1 Serial Imaging

Complimentary to the XCT imaging, a destructive technique was employed to inspect the volume of the sample. This method involved careful grinding away of material to a prescribed depth, as described in section 3.1. Use of this technique enabled direct comparison and verification of the XCT images and was carried out for a number of samples as part of this study.

Figure 5-22 shows the matching of 2D images obtained by optical, Fig. 5-22(a), and XCT imaging, Fig. 5-22(b), through the same defect. These two images demonstrate very good matching and many of the same features of the defect are visible. This was completed for the entire sample with images captured at intervals of 0.15 mm. Validation of the use of XCT to image the defects in AZ80 alloy and confirmation of its accuracy is one of the most valuable outcomes of this research.

Completing the XCT imaging for the sample shown in Fig. 5-22 demonstrated that the two defects visible in the optical micrograph are in fact connected. This conclusion may not have been realised if 2D imaging only was relied upon.

The serial imaging method also highlighted the limitations of the XCT imaging with regard to the limit of the resolution and lack of contrast. Features in the optically imaged defects are not present in the XCT 2D image, such as the fine branches which reach towards the particle clusters. However, the isolated cluster of particles visible in the upper left region of the optical micrograph, Fig. 5-22(a), may not have been associated with the main defect present if only imaged in 2D.

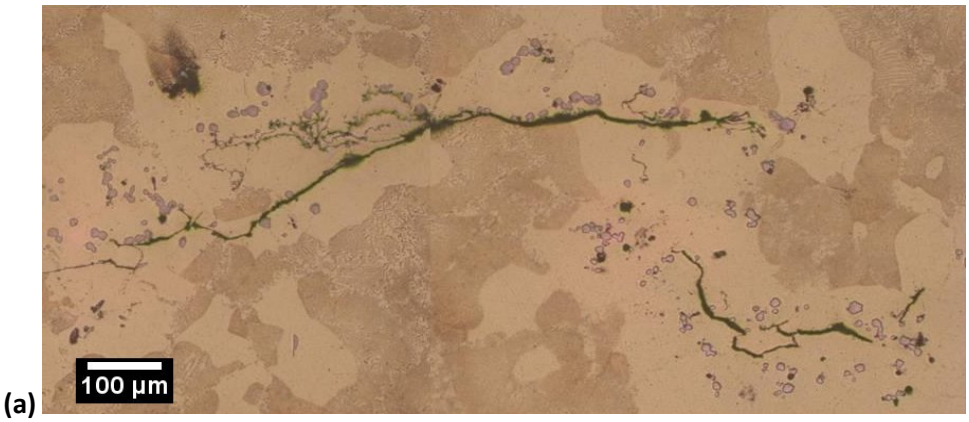

(a)

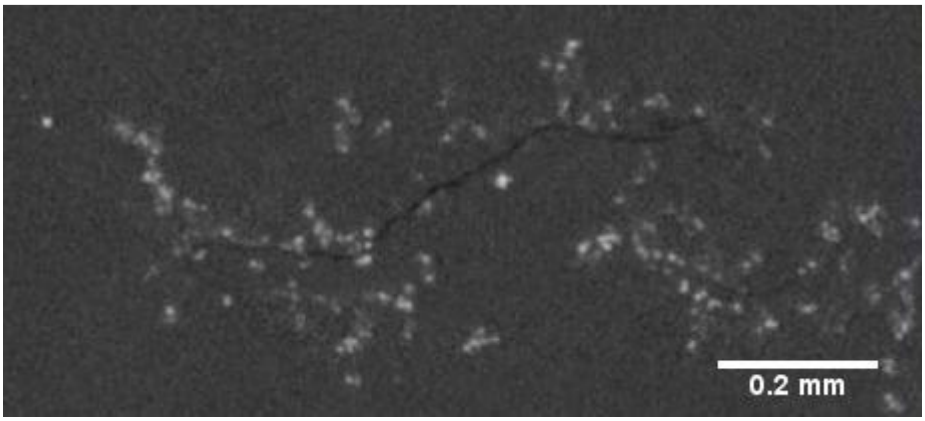

(b)

Figure 5-22 Image matching of serial sectioning images, (a) optical micrograph, (b) XCT orthoslice.

The location of a defect with respect to the grain structure could not be determined by the XCT imaging technique, as grain boundaries were not visible. This was only possible when a prepared and etched surface was imaged by optical microscopy or by SEM, Fig. 5-22(a). The defect is observed to be present both through and around grains of the primary α-Mg phase. This is true for both the entrained oxide film and the intermetallic particles that comprise the defect. Knowledge of the location of the defect in the microstructure is important as it can indicate at what stage during solidification that it formed.

The defect, specifically the entrained oxide film, was observed to separate regions of primary α-Mg and eutectic microstructure. This suggests that the entrained oxide film blocked the growth of the eutectic structure within the alloy, Fig. 5-23.

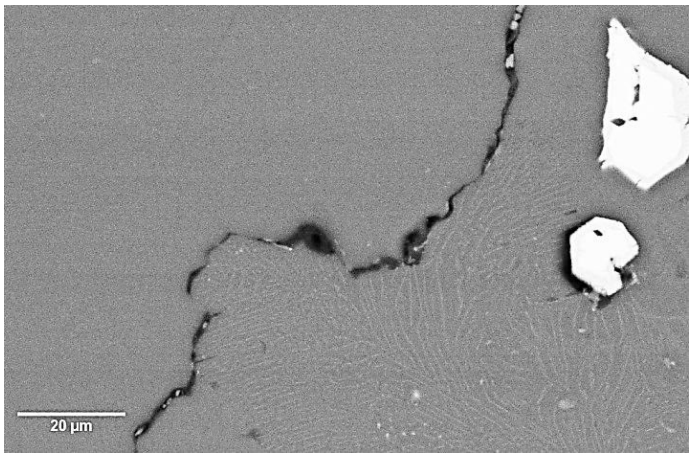

Figure 5-23 SEM micrograph of defect, entrained oxide film separating α-Mg grain and eutectic microstructure.

A substantial number of other defects were imaged by optical microscopy. The observed defects are shown at various magnification levels and in both unetched, Fig. 5-24(a)-(c), and etched microstructures, Fig. 5-24(d). The complex and branched morphology of the defects are clearly visible. The association with particles is strong in some regions, however there are large regions where there are no particles present. By carrying out the same Voronoi tessellation technique as for the clean material the resulting average cell size was 0.00045mm^2, a reduction in cell size of 100 times, a clear indication of the clustering that is observed. The variation in the entrained oxide film is also visible, as some regions are as wide/thick as 30 µm compared to others which are only 2 µm wide.

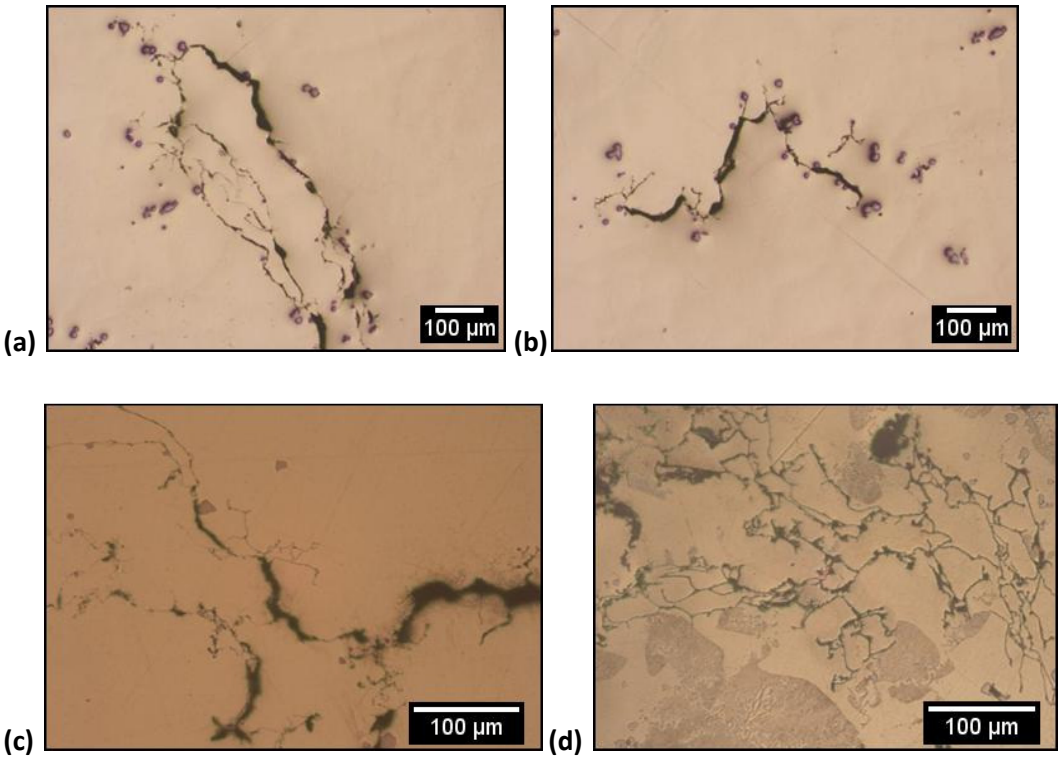

Figure 5-24 Optical micrograph of defects in AZ80 alloy, at various magnifications. Samples (a)-(c) non-etched, sample (d) etched to reveal microstructures.

Serial imaging was also carried out on a number of ZW3 samples thought to contain a similar casting defect. Once located and prepared following the same method as for the AZ80 alloy samples optical microscopy was carried out. The defects appeared almost identical to those presented above as shown in Fig. 5-25.

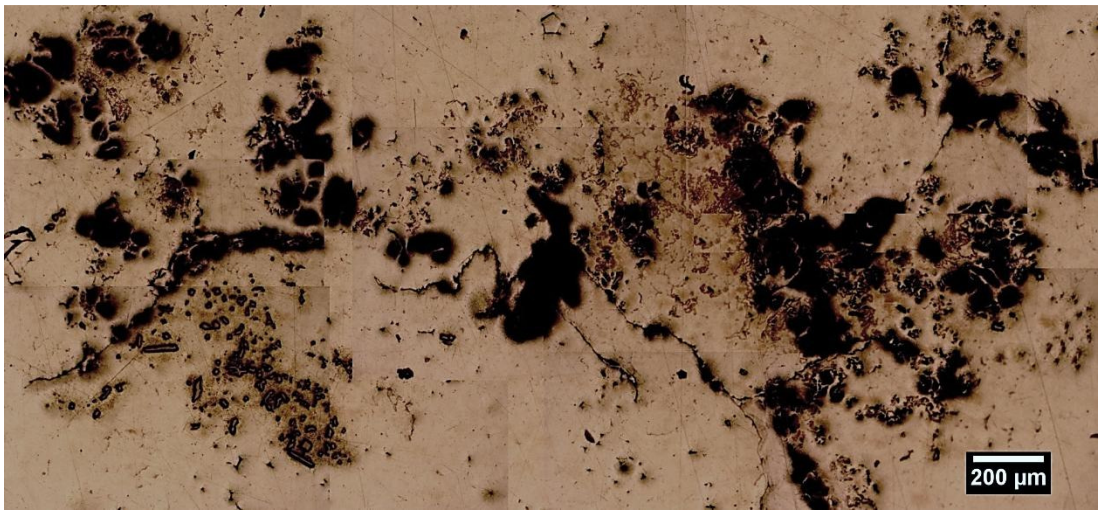

Figure 5-25 Optical micrograph of defect in ZW3 alloy.

The presence of particle and entrained oxide film both folded and stretched can be observed. However the main difference is the particles associated with this type of defect, which are not of an intermetallic composition but shown by EDX to mainly consist of Zr. Also the particles in ZW3 have a cube-like morphology and significantly larger size than those observed in both the AZ80 alloy and the normal defect free ZW3 microstructure. These large particles can be identified as unmelted Zr particles from the alloying stage and more specifically from the Zirmax hardener that is used.

5.4.2 FIB Study

Additional characterisation of the defects was achieved using the FIB milling technique in combination with SEM. This technique provided a series of 2D images, Fig. 5-26, through the defect providing information on the internal structure of the defect.

Serial sectioning was carried out on samples with defects at known locations in the microstructure and those that were visible on the prepared surfaces.

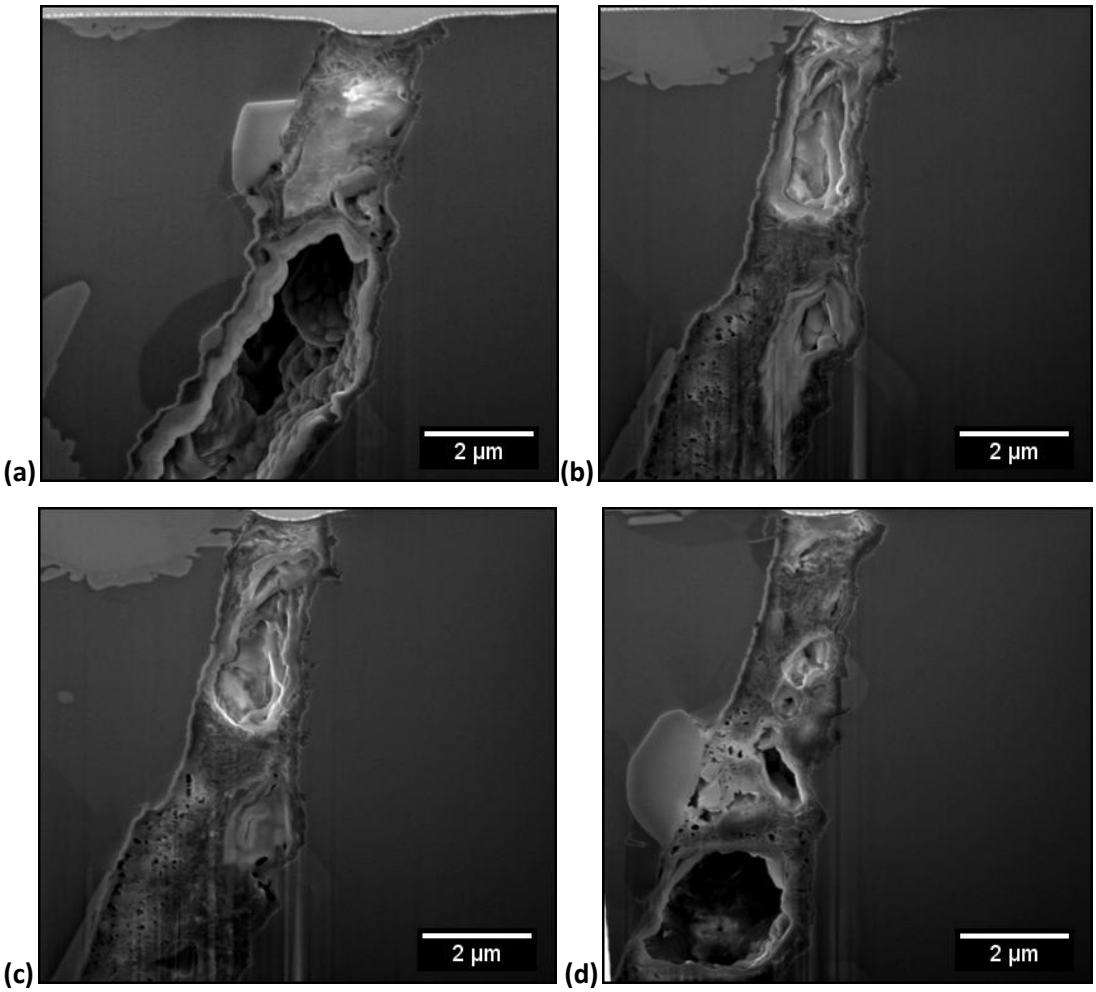

Figure 5-26 SEM images of cross-section of defect, images (a) – (d) passing through the defect. Serial imaging achieved by FIB milling.

Images of the internal structure of the defect reveal the presence of the entrained film, lining the edges of the crack like defect, Fig. 5-26(a). The entrained film is clearly visible due to the contrast with the matrix, which is much darker. The entrained film is also folded within the defect and encloses pores, some of which are large and connected by a complex arrangement of folds and breaks in the film, Fig. 5-26(d). Within the porosity the smooth or bobbled surface suggests the formation of such a defect occurred at high temperatures as it does not reflect the characteristic breaking or tearing that would occur at low temperatures. The lack of any free surface suggests that the surrounding α-Mg matrix formed around the film and thus it can be concluded that it solidified after the film formed, as expected. This indicates that the film became entrained when the alloy was molten.

Particles can be seen to be present on the side of the entrained film. This demonstrates the affinity that may exist between the particles and the film. The nucleation in this case may be due to the presence of smaller particles trapped in the folded oxide film. In general there is a lack of evidence for a particle nucleating on the entrained oxide film, only a very small number of the particles are observed to be in contact with the film.

From these images it can be seen why defects of this type are a difficult to detect when using ultrasonic or X-ray methods. The presence of an entrained film within the crack like defect will act to transmit any signal across the defect, similar to a filled crack.

The observation that porosity is contained within the majority of the entrained oxide film indicates that this will make them more visible to the imaging techniques. Connectivity of defect clusters by entrained oxide films is still observed by the XCT method when there is no porosity present and the branches are very fine. The suitability of the XCT imaging technique to this application is highlighted by the fact that it can detect each of the defect phases, the entrained film, porosity and intermetallic particles adequately to characterise the defect.

5.5 Tensile Testing

5.5.1 Impact on Strength

The damaging effect of the defects found in this study was characterised by carrying out tensile testing. To demonstrate the effect of the defect on the tensile strength clean material was tested followed by defect containing samples, XCT was used to identify material that contained defects.

The results, Fig. 5-27, demonstrated the expected results of a reduction in elongation to failure and a reduction in ultimate tensile strength (UTS). The reduction in elongation to failure showed a large reduction from 4% down to 2%, this is a direct result of the presence of the defect and the brittle nature that it exhibits, in comparison with the Mg matrix, as reported by Griffiths and Lai [Griffiths and Lai, 2007]. The ultimate tensile strength is also reduced from 180 MPa down to 150 MPa.

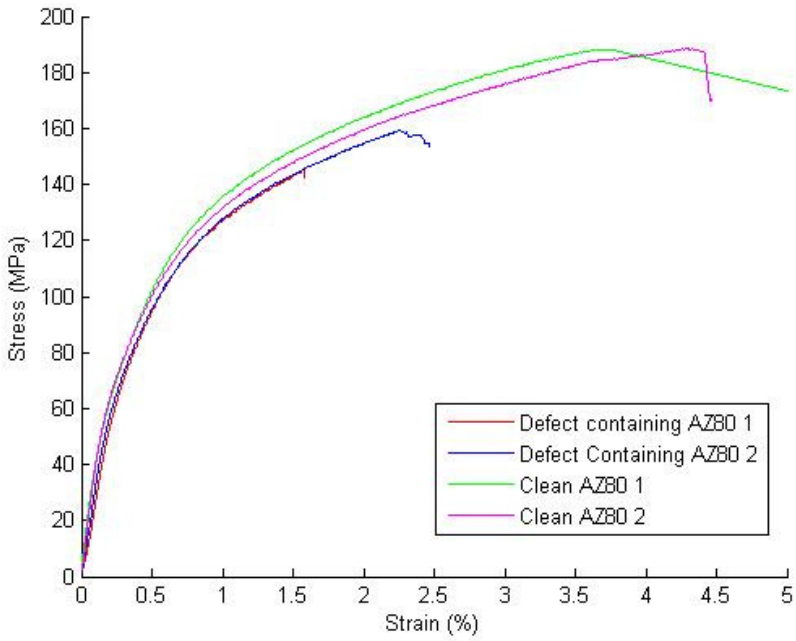

Figure 5-27 Tensile data for clean and defect containing AZ80 alloy.

Inspection of the fracture surfaces reveals that the tensile samples failed at defect sites, Fig. 5-28. The presence of a tarnished oxide film is clearly visible on both fracture surfaces, these mirror each other suggesting that the entrained film was a

bi-film, as proposed by Campbell [Campbell, 2006; Wang et al., 2009]. The failure at this location is not surprising as the entrained oxide bi-film is known to contain pores. There is also the presence of particles observed within the revealed oxide film, which are more clearly observed by SEM, Fig. 5-29, confirming that it was a defect similar to those imaged as part of this study. Electron imaging also shows the difference between the entrained film surface and the normal tearing of the specimen, Fig. 5-30.

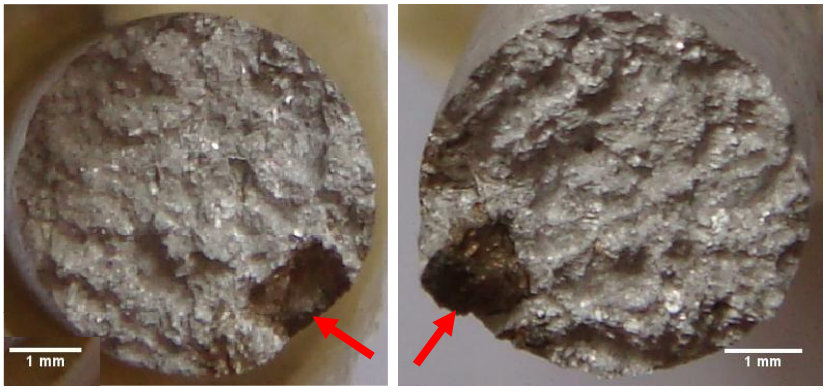

Figure 5-28 Fracture surfaces of defect containing AZ80 tensile specimens, showing oxide bi-film (tarnished region) on surface.

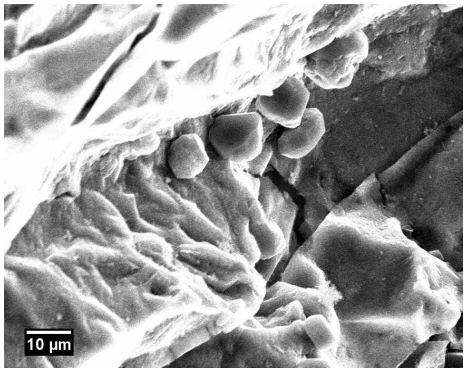

Figure 5-29 Intermetallic particles present on the entrained oxide film visible on the fracture surface.

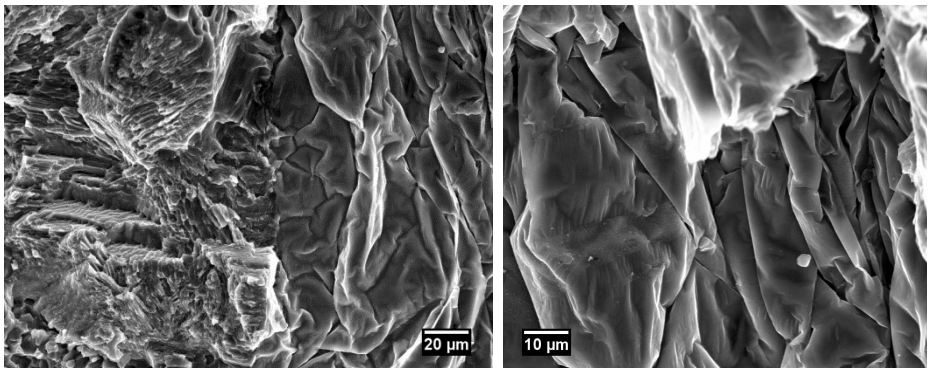

Figure 5-30 SEM image of oxide film on fracture surface, exhibiting the folding that is a distinct feature of this defect.

5.6 Discussion of the Characterised Defects and their Location

Prior to this study the origin and type of defect that was located in the AZ80 by the ultrasonic inspection process was unknown. The results of the characterisation have shown that the defect is an entrained oxide film with intermetallic phase particles entangled within it. This type of casting defect has been observed in other alloy systems [Aihua et al., 2008; Cao and Campbell, 2005] but this is the first time it has been reported for AZ magnesium alloys.

The defects observed imitate almost exactly the entrained oxide bifilms reported by Campbell [Campbell, 2006]. This type of defect is clearly the direct result of turbulent handling of the alloy when in the molten state due to the thinness of the film [Cao and Campbell, 2005; Campbell, 2006]. The bifilms observed in this study, as part of a defect, all possessed a level of porosity as would be expected [Fox and Campbell, 2000] and EDX analysis indicated high levels of oxygen as would be expected. The bifilm was observed on two opposing faces of a fracture surface and exhibited the butterfly-like symmetry as would be expected of a defect of this type, Fig. 5-28.

The intermetallic phase particles of stoichiometric composition Al_8Mn_5 were identified by EDX match with those previously reported for this alloy system [Sin et al., 2007; Ye and Liu, 2006]. The distribution of particles involved in a defect was shown to be much larger than the normal distribution by Voronoi tessellation analysis which resulted in a reduction in the average cell size from 0.04 mm^2 within the defect free microstructure to 0.00045 mm^2 surrounding the defect. This clearly shows the level of clustering that exists associated with defects.

Location of the defects by ultrasonic inspection proved to be reliable as the indicated regions all contained defects. Gaining any further information on the defect was not possible and the ultrasonic response size was no indication of the defect size. Of the many defects found in this study there was no relationship determinable for the ultrasonic response it generated to its actual size. This was demonstrated by the fact that a number of the defects studied which produced a single response peak when inspected by the ultrasonic method were shown to

consist of several separate oxide fragments by XCT, section 5.3.2, which might have been torn by shrinkage or dendrite action [Wang et al., 2009]. However it was shown that it was possible to establish the depth of the defect from the billet surface from the response signal, Fig. 5-12. Once this was established no further attempt was made to infer the defect size from the signal as limitations of interpreting this sort of information from the response signal are known [Thomson, 1984].

Informed by the results of the FIB study the defects clearly contained porosity and regions where the oxide film closed over itself, section 5.4.2. From this an insight is gained into the possible causes of transmission of signal in both the ultrasonic and XCT imaging techniques which will reduce visibility. These images also demonstrated that the associated intermetallic particles are in contact with the oxide film and appear to have nucleated on a particle trapped into the folded film. The presence of particles in the film or trapped within the folds is also apparent on observation of the fracture surfaces. Particles can be seen to be revealed as a result of the opening of the film on fracture, Fig. 5.29. The main conclusion from this is that particles do not exhibit wetting of the film and it can therefore be concluded that they do not favour nucleation on the film. This counters suggestions that oxide may be a favoured nucleation site for the intermetallic phase Al_8Mn_5 [Fan et al., 2009]. The cause for this discrepancy may be the different forms of the oxide present in each study. Fan et al. identified oxide particles, not entire films, as potent nuclei for Al_8Mn_5. It must also be stated that the observation of oxide particles within the intermetallic phase was not observed in this study. There is also the case where oxide particles become engulfed by the growing grains or particles, which in this case would not be possible due to the contrasting sizes of the two phases in consideration.

Many similarities can be drawn between the defects observed in the AZ80 alloy and the ZW3 alloy. However, the one difference is the particles which are present in the defects. Those associated with the ZW3 defect are not of a precipitated intermetallic phase but were present in the original feedstock for casting meaning that association of particles and oxides must be a mechanical coming together and

entanglement. The particles observed are possibly Zr particles remaining from the grain refining master alloying addition, Fig. 5-25, however this was not confirmed during this study.

5.7 Summary

A range of inspection techniques were used in order to characterise the defects found in the AZ80 DC cast alloy. The different techniques were employed for a range of purposes such as to provide cross-validation, inspect different aspects of the defect structure, or to better image certain characteristics. The set of techniques used in this study provided a large amount of information on the defects, more than was possible by each alone or had been achieved previously.

The serial imaging was extremely useful in validating the XCT images, while the FIB and SEM imaging revealed more detail of the defects, beyond the ability of both the XCT and ultrasonic inspection methods.

The analysis of the data produced by each inspection enabled a fuller characterisation than has been achieved previously and identified the essential features of the defects that occur in DC cast AZ magnesium alloy. This study also provides clues as to the origins and formation of the defects, which will be discussed in more detail in chapter 6.

In summary the findings of this section are that the defects comprise of two phases the intermetallic particle (Al_8Mn_5) clusters and the entrained oxide film. The two phases are always found to be present together within a defect. There is also porosity associated with the defects. The combination of entrained oxide and porosity was demonstrated to be very damaging to the materials mechanical properties, in particular the elongation to failure, which is approximately half that of clean material when a defect is present. The defects are typically found within a central region of the billet and can be very large in size, up to 5 mm in the longest characteristic length.

6 Defect Formation Processes, Analysis and Modelling

Understanding the defect formation process can suggest suitable measures to improve the quality of the cast material. The formation process can be indicated through knowledge provided by the detailed characterisation already achieved in this study. However, a detailed study of the mechanisms which influence the cause of the defects, their size and location is still required.

This section will discuss the findings of the study into the possible defect formation methods, using experimental and computer modelling approaches. For this analysis the intermetallic particles and the entrained oxide film were studied separately; consideration of the combined defect is made at the end. The aim was to identify the mechanisms which control the formation of a defect during casting.

6.1 Precipitation Study

Growth of the intermetallic phase Al_8Mn_5 particles, found to be present in the defects, was studied using a modified Kampmann and Wagner Numerical (KWN) model. The KWN model was adopted and subsequently modified to accurately simulate the precipitation process, as discussed in section 4.2. The modified KWN model required calibration before any useful predictions could be generated. With a fully calibrated model the growth process and the effect of any change on the casting conditions could be studied. This section will discuss the calibration process and the results generated by the KWN model.

6.1.1 Calibration

Calibration of the KWN model was achieved using data obtained from analysis of experimental castings each with a different cooling rate. The experimental castings were produced as described in section 3.6.

The required parameters for accurate calibration of the model were the interfacial energy, between the particle and the matrix - in this case the liquid AZ80 alloy, and the nucleation site density efficiency.

The cooling rates achieved during the experimental castings were recorded by the use of thermocouples and are plotted in Fig. 6-1. The cooling rate used for modelling purposes, interpreted from the gradient of the cooling curve over the temperature range that solidification occurs (600 – 450°C) are presented in Table 9. The resulting particle size in each casting was then measured as described in section 3.5.2 and the results also included in Table 9.

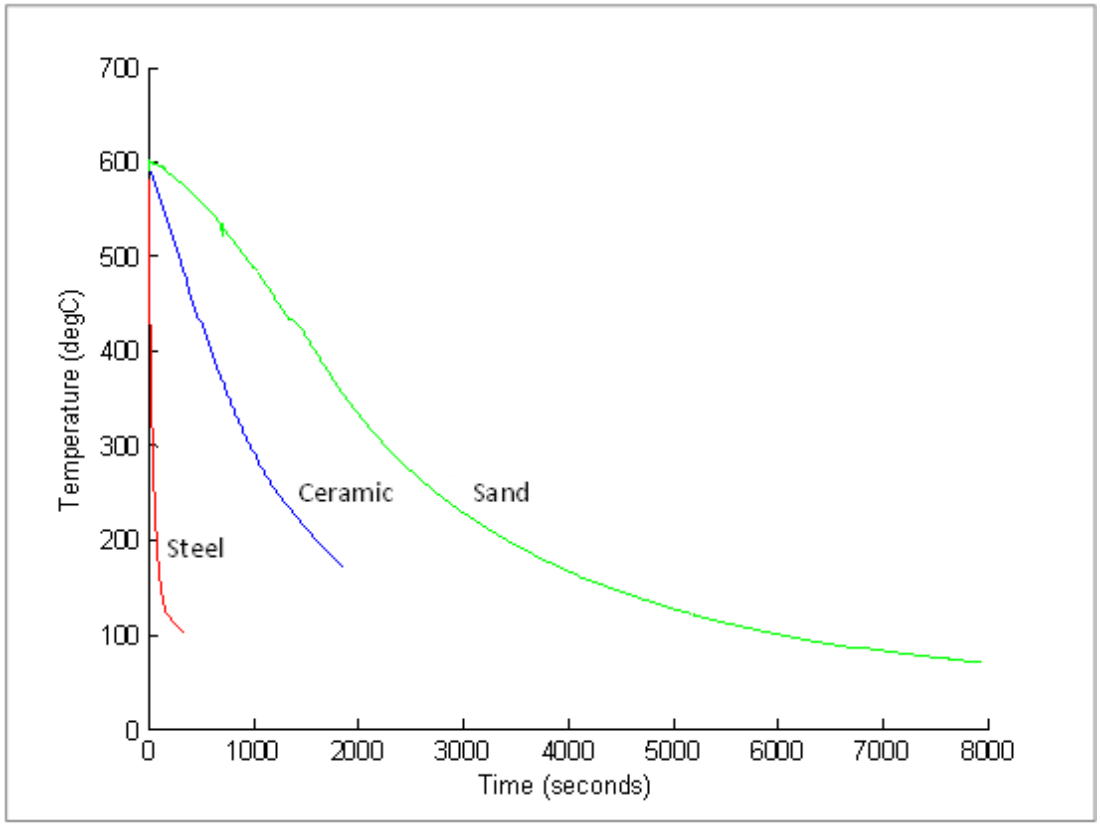

Figure 6-1 Cooling rates recorded for each experimental casting.

Casting mould material	Cooling Rate (degC/sec)	Average Particle Radius (µm) (Standard deviation)
Sand	7.7	0.80 (3.09)
Ceramic	0.32	2.06 (1.97)
Steel	0.15	2.70 (0.92)

Table 9 Cooling rate recorded and corresponding particle size measured for each experimental casting type.

The cooling rate can be seen to have an effect on the resulting particle size; that is the lower the cooling rate the larger the particles grow. The chill sample contained many more, smaller particles in the resulting microstructure whereas the sand and ceramic mould castings possessed a similar number of particles only those in the sand casting were significantly larger than in the ceramic, this can be observed in the SEM micrographs, Fig. 6-2.

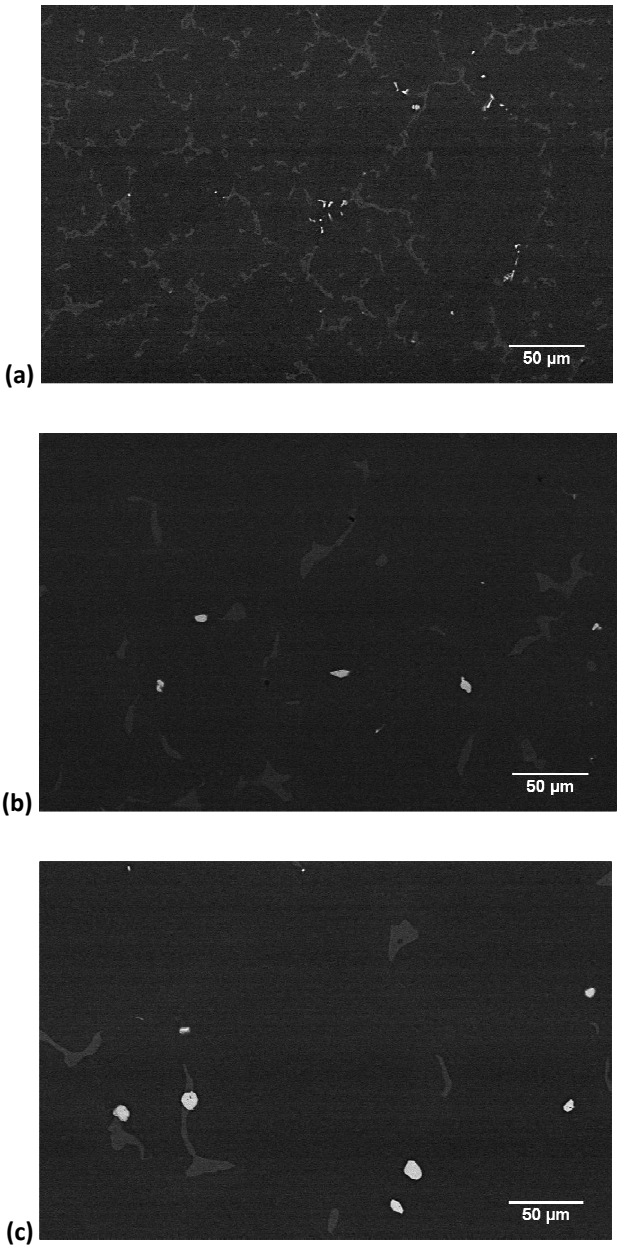

Figure 6-2 SEM micrographs of experimental castings in (a) chill mould (b) ceramic mould (c) sand mould all at same magnification.

Once the cooling rate and corresponding resultant particle size was established by experimental methods, the optimum parameters for the KWN model were identified to ensure the predictions of the model replicated those obtained experimentally. The results of the model predictions are shown in Fig. 6-3, and can be seen to agree with the respective measured particle size in the experimental castings.

It was found that the correct parameters to be used for this precipitation and growth process were an interfacial energy value of 0.012 J/m^2 and a nucleation site density efficiency of 0.00048. With these parameters established it was possible to simulate particle growth for a range of cooling rates including those that were to be expected during the production of a billet by DC casting.

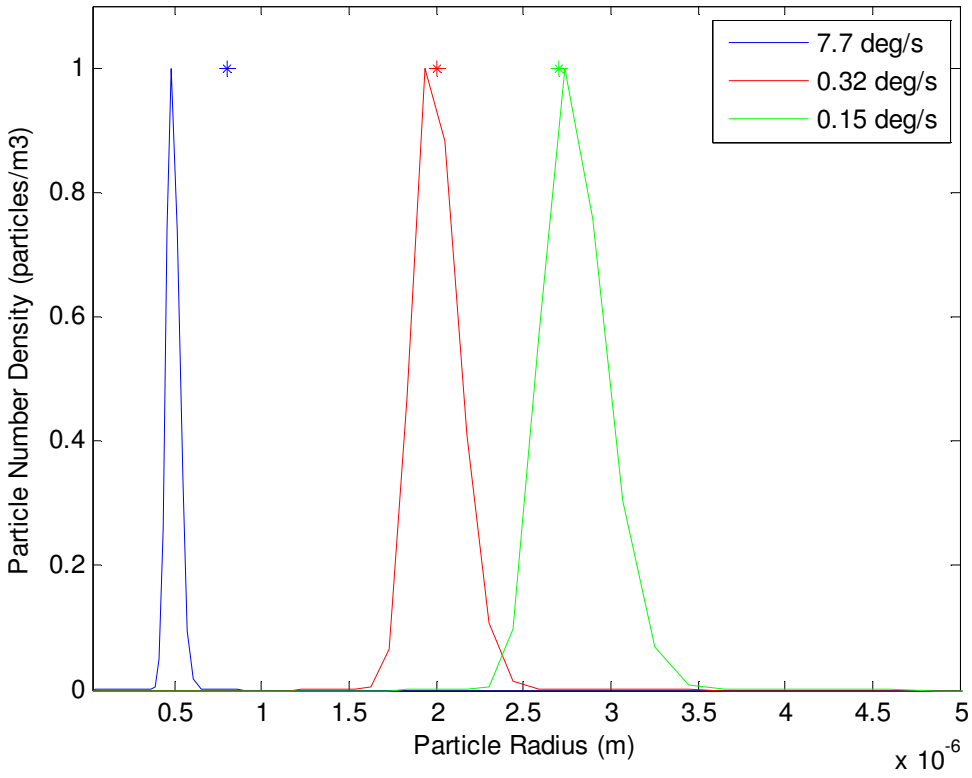

Figure 6-3 resultant particle sizes for each experimental casting mould type, with the experimentally measured mean values marked (*) in the respective colours.

There is a small discrepancy between the simulated and experimentally measured particle size. The difference between the two values is within the experimental error for the measured particles thus the model parameters can be considered accurate.

Additionally there is a larger spread of particle sizes in the modelled results for the sand mould casting and less so for the other two casting types. This trend agrees with the standard deviation for each of the experimentally measured particle sizes and as would be expected; the spread of resulting particle sizes for the slower cooling rate is larger.

The accuracy with which the model was now able to predict the resulting particle size for different cooling rates for the AZ80 alloy system demonstrated that it was calibrated. This enabled a relationship to be developed between the resulting particle size and the cooling rate they experienced for a range of cooling rates and also to estimate the cooling rate a particle must have experienced during growth.

6.1.2 Cooling Rate – Particle Size Relationship

A relationship was established between the cooling rate and resultant particle size for a complete range of cooling rates using the calibrated KWN model. This relationship was determined for a range of cooling rates that included those predicted to occur during DC casting, Fig. 6-4, from 0 – 7.5 °C/sec.

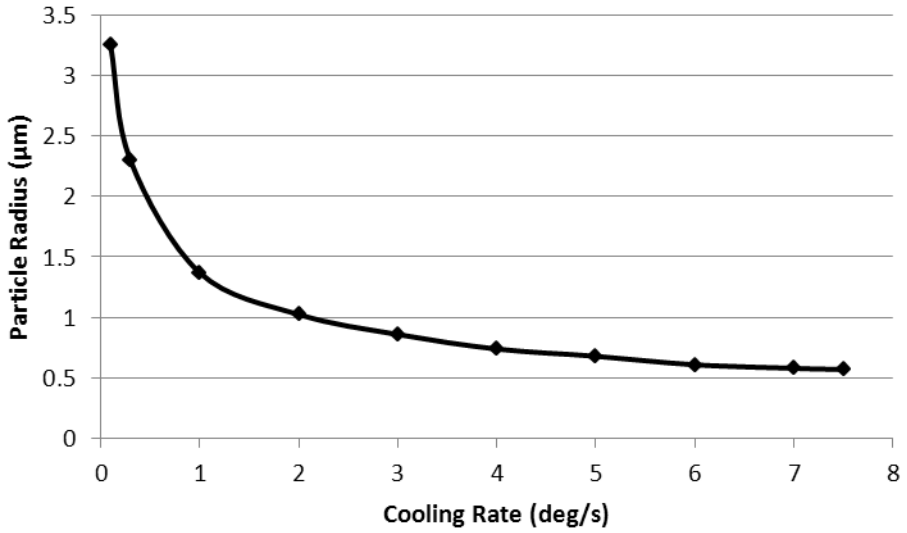

Figure 6-4 Cooling rate and particle size relationship produced by modified KWN model.

The relationship between the cooling rate and the resultant particles size predicted by the KWN model for the AZ80 alloy system shows the general trend of a reduced resultant particle size with higher cooling rates. At very low cooling rates the resulting particle size is large and at the highest cooling rates predicted the resulting particle size appears to be less sensitive to cooling rate, plateauing at a minimum equivalent radius of 0.5 µm.

Establishing this relationship enabled the accurate prediction of the size of particles at any intermediate cooling rate that may be realised during DC casting of AZ80

alloy. This approach assumed that the cooling rate was the dominating influence on the resulting size of the particles in the casting and that at each location in the mould the features present experienced a constant cooling rate. The cooling rates during casting were predicted by a model developed by Magnesium Elektron, U.K. using Alsim software, Fig. 6-5(a).

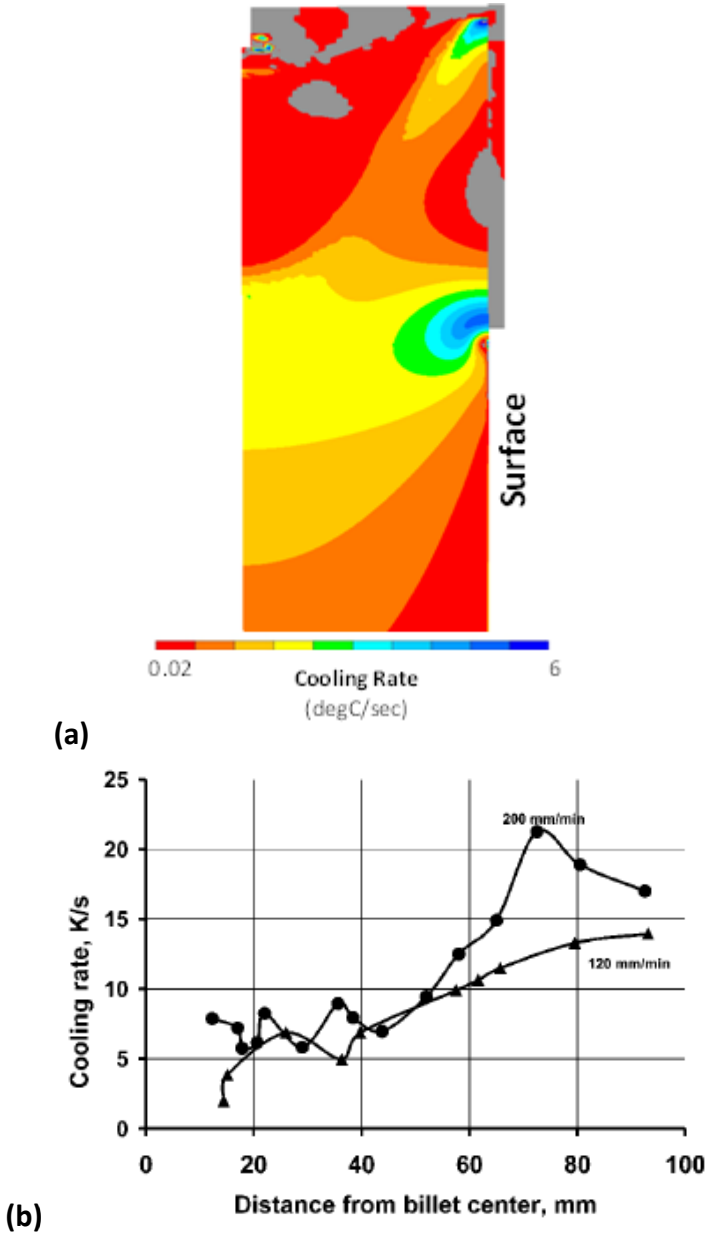

Figure 6-5 (a) Cooling rates during DC casting of AZ80 billet, simulation from Alsim. [Provided by Magnesium Elektron, U.K.], (b) Distribution of cooling rates estimated from computed streamlines for two casting speeds: 200 mm round billet is considered [Eskin and

Analysis of the cooling rates predicted to be realised during DC casting suggested that at the centre of the billet the cooling rate is significantly lower than at the billet

surface. The liquid sump in the centre of the billet is predicted to cool at a rate of around 0.02 °C/sec or less. This can be compared to the billet surface, which is predicted to cool at 6 °C/sec, at the point of solidification. The measured particle size across the radius of the DC cast billet did correctly reflect this trend in cooling rates, Fig. 6-6. This trend is more clearly observed when looking at the maximum particle size measured at each location across the billet radius, with the largest being present at the centre of the billet at 15 µm in radius and the smallest being present at the billet surface with a radius of 7 µm.

Using the relationship predicted by the KWN model, the resultant particle size should be very small at the billet surface. The cooling rate at the point of solidification at this location can be interpreted as nearing 6°C/sec. According to Fig. 6-4 the resultant average particle size should be 0.61 µm in radius, however they have been measured to be 2.8 µm in radius, Fig. 6-6. The measured value is significantly larger than those predicted, suggesting that other factors may be influencing the particle growth and the final size. The same is true for the other locations across the billet radius, at the billet centre the predicted low cooling rate of 0.02°C/sec would be expected to result in particles with an equivalent radius of 3.25 µm. However particles at this location were measured as having an equivalent radius of 4.75 µm, Fig. 6-6, again significantly larger than that predicted or expected from the experimental castings.

The same analysis using the cooling rates predicted by Eskin and Katgerman [Eskin and Katgerman, 2009] demonstrates a similar lack of correlation with the experimentally measured particle size in a billet. Much higher cooling rates are predicted, Fig. 6-5 (b) [Eskin and Katgerman, 2009], according to the KWN model developed in this study, to result in particles with a radius of 0.5 µm at the centre. This mismatch between predicted and measured microstructural features was shown to be the case for grain size too [Eskin and Katgerman, 2009]. It is suggested to be a result of the particular thermal history of the grain or particle being considered which does not correspond to the predicted or recorded thermal history for the location it is observed. This is a result of fluid flow effects; the final position of a particle or grain in the microstructure does not provide information about its

thermal history as it develops in the liquid. The thermal history of the feature of interest is actually likely to be much longer than the actual solidification time (cooling rate) suggested at the location it is recorded. To determine the role of this effect, analysis of the flow patterns in the sump was required to reveal the flow trajectories of the individual particles or grains from which their individual thermal histories may be determined.

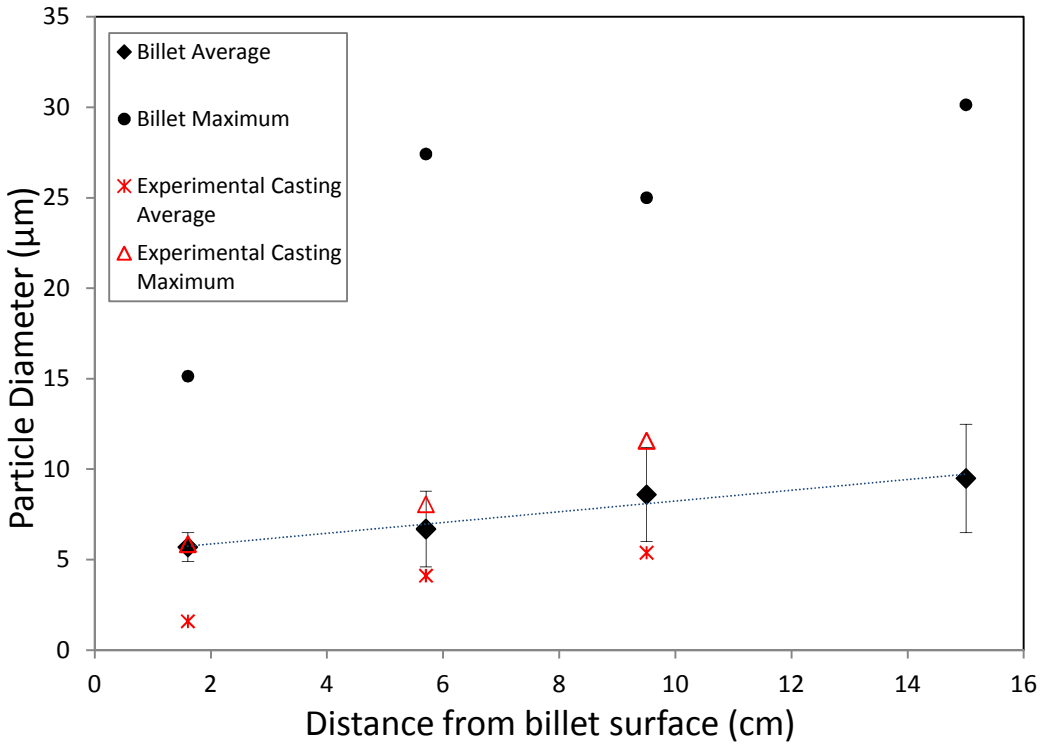

Figure 6-6 Measured particle size across a DC cast billet radius and measured particle size in experimental castings (red).

Since the model predictions and the measured values did not agree by a large margin, it would indicate that using the average cooling rate at a particular location is not sufficient to represent the true thermal history seen by a particle as it develops in the melt. This is especially the case when the particles are a constituent phase of a defect, in which the situation is even more complex. Suggestion of the importance of the thermal history as influenced by the flow in the sump [Eskin and Katgerman, 2009] indicates that knowledge of the flow regime within a mould may assist in identifying a defect formation mechanism.

6.1.3 Precipitation Rate Prediction

To better understand how particles will evolve in liquid as a function of temperature the KWN model was used to provide a better insight into the kinetics of precipitation. Knowledge of the precipitation behaviour such as rate and effect of temperature can be gained by producing a precipitation-time-temperature (PTT) diagram from the KWN model data.

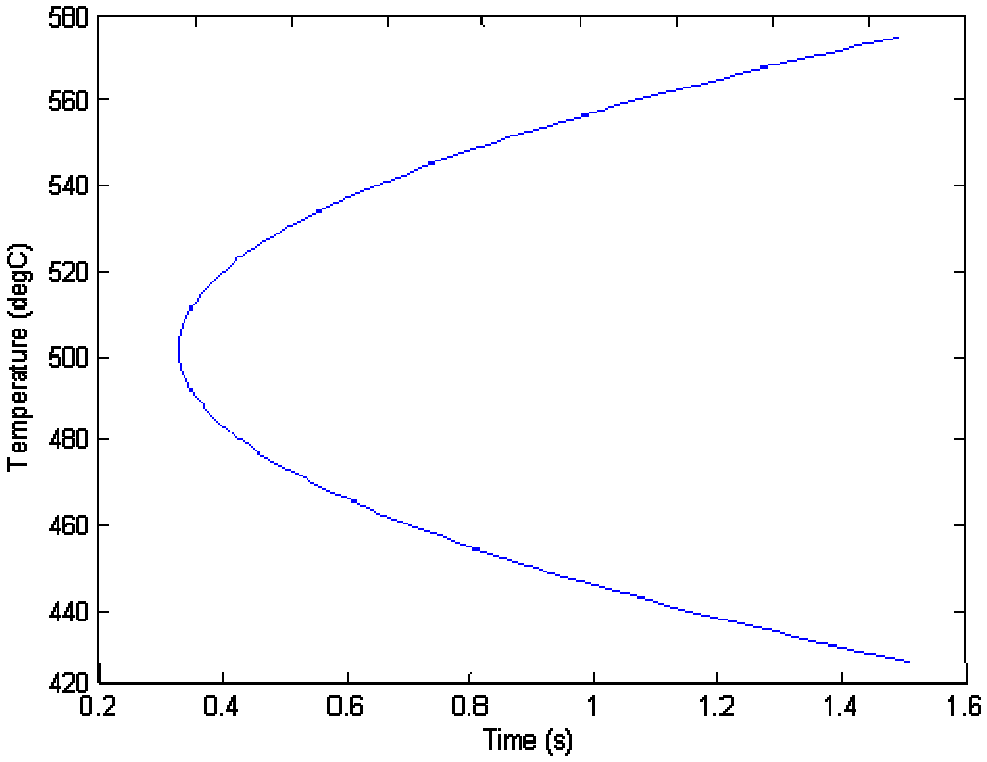

Figure 6-7 Precipitation-Time-Temperature (PTT) diagram for 50% volume fraction of Al_8Mn_5 in AZ80 alloy system.

The predicted PTT diagram for 50% the maximum possible volume fraction precipitation of Al_8Mn_5 intermetallic particles in the AZ80 alloy, Fig. 6-7, was established from the calibrated KWN model developed in this study. It can be seen that the most rapid precipitation is predicted to occur at around 500 °C for the AZ80 alloy. This demonstrates that the precipitation is most likely to occur towards the end of the casting process and not during transfer of the melt as the melt is known to enter the mould at above 650 °C.

These results suggest that the growth of particles occurs mostly during its residence time in the mould. However, the particles are known to form at much higher temperatures (>600°C) than those predicted and would be expected to form before entering the mould. The cooling rate predicted at the centre of the mould is very slow, around 5°C/s, this would represent a flat line in Fig. 6-7. It is therefore very unlikely that the rate of growth, as indicated in Fig. 6-7, would ever be realised. What can be expected is that the particles would grow most rapidly when they experience temperatures around 500°C.

6.2 Melt Flow Study

It was established that the cooling rate must not be the only influencing parameter on the final intermetallic particle size the cast billet. It was recognised that the industrial production of any alloy involves the interaction of many different processes which will influence the defect content in the final product. This section will attempt to establish a mechanism by which the entrained oxide films are generated for the casting equipment employed to produce the billets used in this study.

The subsequent two sections will return to consider the intermetallic particles and the combination of both intermetallic and oxide seen in the typical defects observed in an attempt to establish an accurate defect formation mechanism using the results of the two individual studies.

6.2.1 Filter Inspection

This study identified three stages of the casting process as likely to impact on the defect content. These included, pouring from the crucible into the launder, filtering and the flow control at the mould inlet pipe region. This section will report the results of the filter inspection carried out to understand the effectiveness of the filtering currently employed.

The filter was imaged after a typical casting process, Fig. 6-8, then sectioned and prepared for optical microscopy following the same preparation route as for standard samples described in section 3.1. The resulting micrographs, Fig. 6-9, show the cross section through the steel mesh filter with solidified material surrounding it.

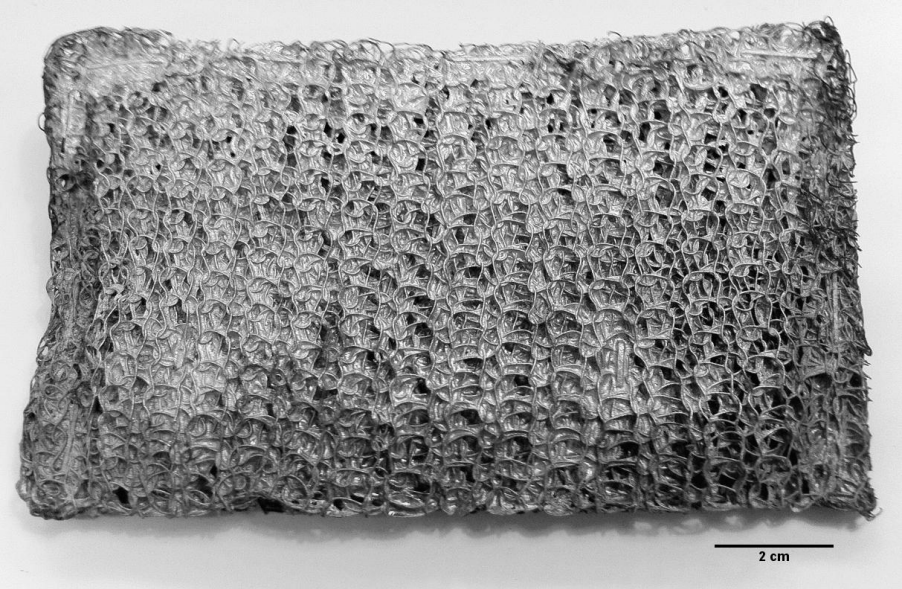

Figure 6-8 mesh filter removed after casting of AZ80 alloy, upstream face visible.

On inspection of the complete filter it is clear that no caking has occurred and the filtering mechanism active is depth filtration. The reason for this is that the apertures in the filter are typically much larger than the inclusion that it is intended to filter from the melt. Entrained oxide films are observed to be collected by the filter, Fig. 6-9, and have become wrapped around the filter mesh. The coarse apertures in this filter are suited to this application as they do not restrict flow as would be expected if the filter operated by cake filtration.

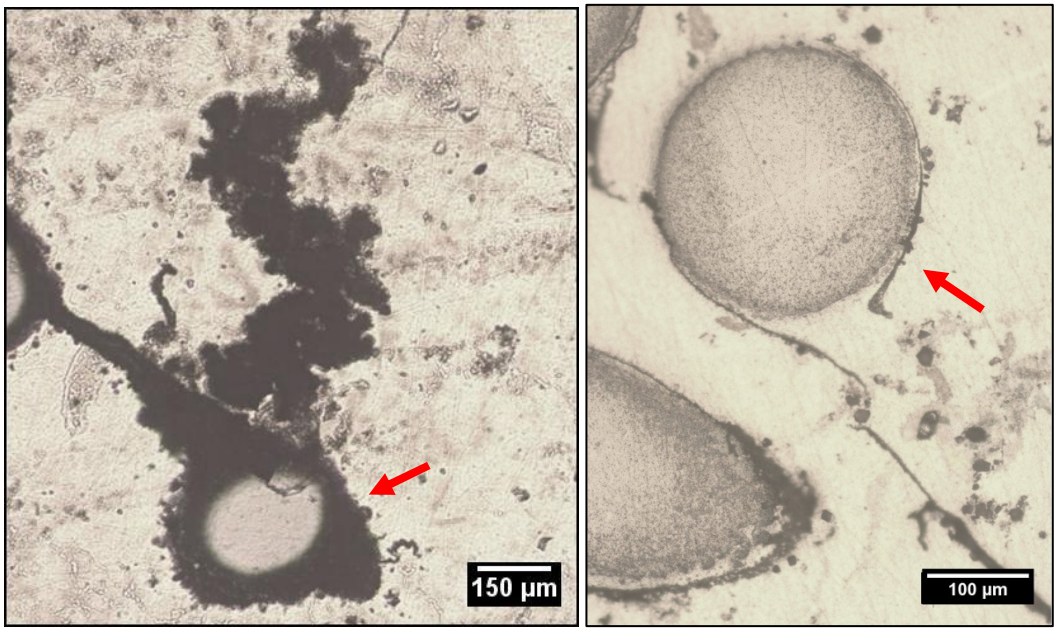

Figure 6-9 Optical micrograph of used steel mesh filter with oxide film entangled around mesh wire.

The mesh filter which is located within the upper section of the launder clearly is effective at removing entrained oxide films from the melt. Inspection of the filter failed to show any real effectiveness at removing intermetallic particles from the melt, only very few can be observed in the micrographs of the filter, Fig. 6-9. Additionally there is not the same association between the entrained oxide film and few intermetallic particles as observed in the final cast product, Fig. 6-10. With the knowledge of the predicted PTT curve derived in section 6.1.3 and that the melt enters the mould at above 600°C, it can be assumed that the conditions at the filter are not conducive to the nucleation and growth of the intermetallic phase particles.

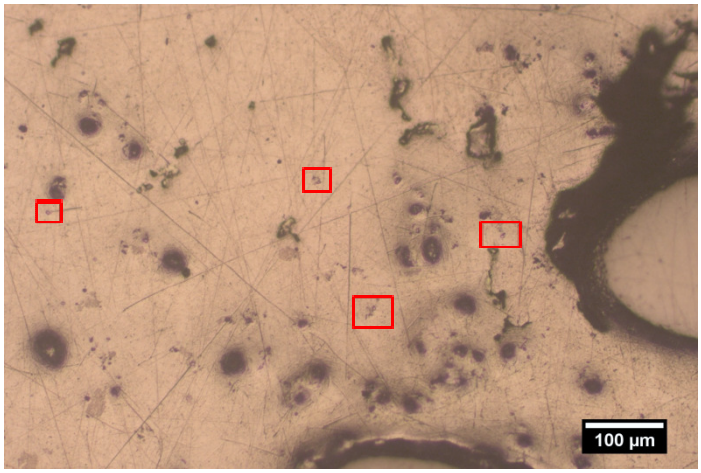

Figure 6-10 Micrograph of used casting filter with the only intermetallic particles present highlighted.

These results also indicate that oxide films, beyond those that are generated by the presence of the filter itself, are present upstream of the filter. This would indicate that the entrained films are present within the melt in the crucible or generated as it is poured from the crucible to the launder. The filter is observed to be effective at removing some of the entrained oxide films generated upstream however, it may also be the case that it permits some to pass through. It was observed that downstream of the filter the melt is relatively clean and for the volume of entrained oxide film to be present, as was observed in this study, in the casting, oxide film must also become entrained further downstream during the casting process. This was demonstrated by the samples taken during casting as described in section 3.10. Inspection of the sample taken downstream of the filter by optical microscopy, Fig.

6-11, shows the absence of entrained oxide film, however it is acknowledged that the sampled volume only represents a very small volume of the melt.

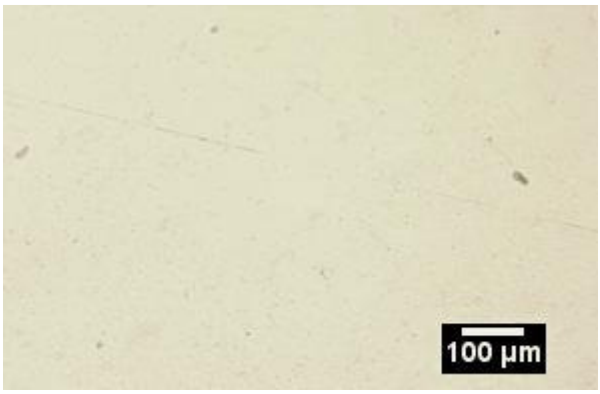

Figure 6-11 Micrograph of AZ80 melt sample taken after filter during casting.

6.2.2 Inlet Pipe Simulation

Since the quality of the melt in the upstream stages of the alloy transfer during casting had been assessed the focus then moved to the inlet into the mould and within the mould. Transfer of molten alloy into the mould during DC casting is achieved by the use of a submerged entry nozzle at the base of the inlet pipe. The flow rate into the mould is regulated by an operator controlled moveable pin at the top of the inlet pipe. This stage of the casting process was identified as a potential cause of entrained oxide films. The flow of molten AZ80 alloy down the inlet pipe was simulated as described in section 4.3 to assess the potential for oxide entrainment at this stage of casting.

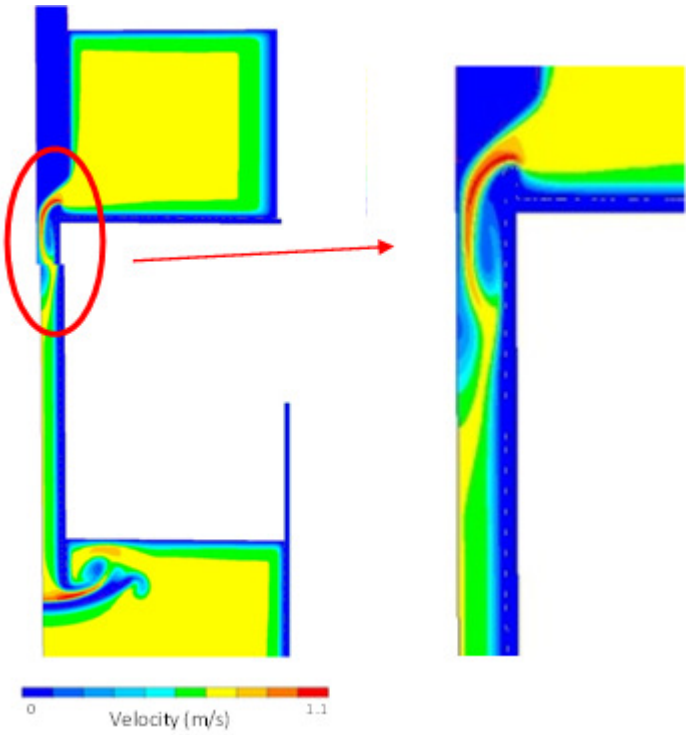

Figure 6-12 Simulation of molten alloy flow velocity from launder, down inlet pipe into mould via submerged entry nozzle.

The results of this simulation indicated that the inlet pipe is not entirely filled during steady state casting, Fig. 6-12, and that there is a degree of recirculation occurring back up along the walls of the inlet pipe. The incomplete filling of the pipe is indicated by the very low velocity regions, Fig. 6-12, which suggests no flow in these regions. This region could alternatively represent the presence of stagnant melt, which may be periodically released with the passing flow. It is also possible to observe the occurrence of jetting, the high velocity flow of melt as it exists the restricted volume, at the entrance to the inlet pipe, Fig. 6-13 has only positive downward velocity shown to show clearly the occurrence of jetting, any recirculation or stagnation is not represented.

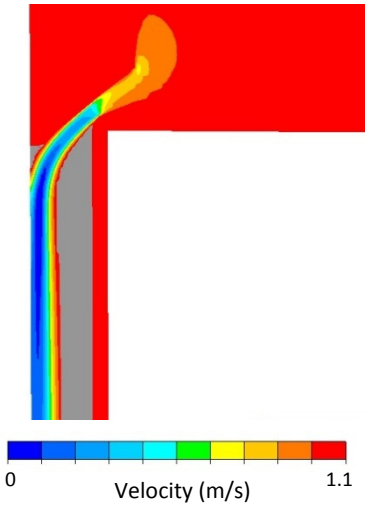

Figure 6-13 Velocity simulation of fluid flow from launder into inlet pipe. (Threshold applied to highlight regions with positive downward velocity only).

The incomplete filling of the inlet pipe will result in an oxide film forming on the free surface of the falling stream, as discussed in section 2.2.3.2. The surface oxide film will be stable as the molten alloy continues to flow within at a constant flow rate. The oxide film will break free if the flow rate is changed or disrupted in any way as suggested by Campbell [Campbell, 2003]. The complete collapse of this type of surface oxide film will result in the presence of a large defect in the final casting.

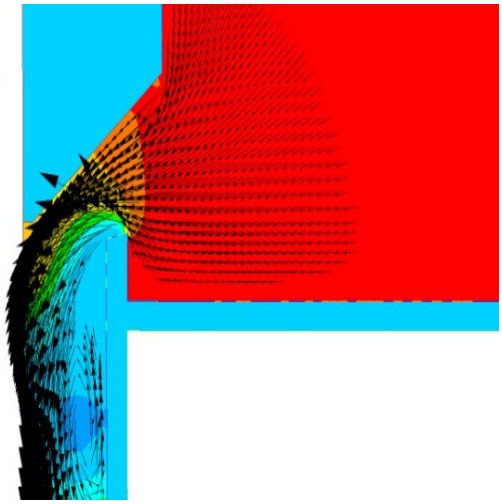

Figure 6-14 Simulated velocity and pressure of the molten alloy flow at the inlet pipe entrance, recirculation pattern given by velocity vectors, contours of pressure (blue – low, red – high).

The jetting at the entrance to the inlet pipe, Fig. 6-14, was observed to be increased by the presence of the small lip. The velocity vectors displayed on Fig. 6-14 shows there is a degree of upward motion required to pass over the lip. This lip is present

in the launder design to prevent inclusions, which have settled to the bottom of the melt, from entering into the final cast product, however this appears to contribute to the presence of the defects seen in this study.

The simulated flow over an equivalent entrance geometry to the inlet pipe, this time without the lip was completed, is shown in Fig. 6-15. It can be observed that jetting still occurs and the velocity is still of the same magnitude, as the same clearance gap is maintained.

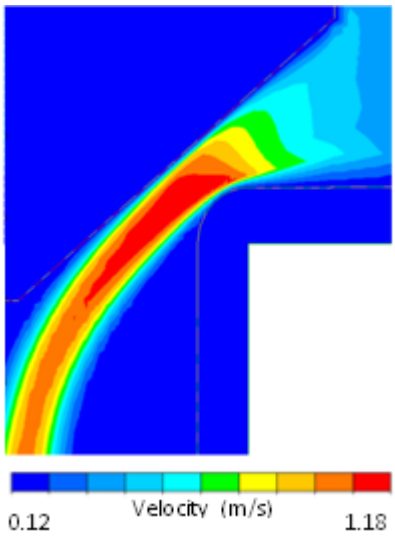

Figure 6-15 Simulated melt flow over modified launder – inlet pipe geometry with lip removed.

In summary the fluid flow simulation highlighted the nature of the flow through the current casting equipment. The occurrence of jetting and the incomplete filling of the inlet pipe suggesting that an oxide film will form on the free surface of the falling stream. This oxide film is likely to fall into the molten alloy if disturbed and become entrained in the molten alloy. The production of AZ80 billets requires frequent adjustment of the flow rate into the mould in order to maintain the melt level in the mould. This is a likely mechanism by which the oxide films are generated and occurs downstream of the filter and thus enter unrestricted into the final cast material.

6.2.3 Viscosity Study

The presence of the defects in this study was initially thought to occur exclusively in AZ80 alloy. However, very similar defects have also been identified in ZW3 alloy.

Initially it was identified that AZ80 castings were particularly susceptible to entrainment defects and inclusions. This was thought to be due to the viscosity of the melt and how it behaved during casting. Simulation of the solidification process by JMatPro provided viscosity data on the AZ80 and for comparison other alloys, offered by Magnesium Elektron, U.K. were simulated, Table 10. The viscosity was simulated at two temperatures, 690 and 660 °C as this is the temperature that the melt will leave the crucible and enter the mould respectively. This transition was the focus of this study as it was thought that at this point of the casting was where the defects were generated.

Alloy	Temperature (°C)	Viscosity (mPa s)
AZ80	690	1.26
	660	1.35
AZ31	690	1.26
	660	1.36
AZM	690	1.26
	660	1.36
ZW3	690	1.29
	660	1.38
ZK60	690	1.31
	660	1.41
WE43	690	1.34
	660	1.44

Table 10 Simulated viscosity for a range of magnesium alloy as predicted by JMatPro.

The result of this analysis demonstrated that AZ80 alloy was not predicted to be significantly different to other alloys manufactured by the same process and thus the viscosity was unlikely to be the origin of the defect formation.

An additional observation was that the drop in temperature during the melt transfer process was not of the scale expected to cause nucleation of particles of the intermetallic phase during melt transfer, as was previously thought. The intermetallic particles are most likely to precipitate after the liquid has entered the mould as discussed previously (section 6.1.3).

6.3 Particle Clustering

Characterisation of a number of the defects found in the AZ80 castings consisted of apparent clusters of particles entangled with an entrained oxide film. An understanding of the clustering process would enable measures to be taken to eliminate this problem. Any solution proposed must account for the observation that most the defects are present within a central region of the cast billet. An attempt was made to identify and isolate a region in the billet which is most susceptible to defects during casting and identify suitable methods to prevent it.

The approaches used to analyse this occurrence were derived from those used in the production of metal matrix composites (MMCs). A significant amount of work has been done to understand the clustering of the reinforcing phase in MMCs in attempt to produce a more homogenous microstructure.

6.3.1 In Mould Flows

Research [Eskin and Katgerman, 2009; Eskin et al., 2004] has shown that flow of the melt in the mould can have a significant impact on the resulting microstructure. This was investigated by simulation of the fluid flow regimes within the DC casting mould during the casting of an AZ80 billet for this study.

The flow regimes predicted by the Alsim software, Fig. 6-16(a), demonstrate that recirculation occurs within the mould. This flow pattern matches those that have been reported experimentally in DC casting of aluminium [Sengupta et al., 2005; Eskin and Katgerman, 2009] clearly exhibiting two recirculating flow paths, Fig. 6-16(b). The first is a smaller loop which joins with the larger circulating flow which is mainly driven by convection at the centre of the sump.

This flow is initially a very fast and narrow stream, resembling the jetting reported [Sengupta et al., 2005] from the submerged entry nozzle. As it approaches the mould wall it is deflected downwards where it is also rapidly cooled and a solidifying front is formed at which point it is deflected along the solidifying front and downwards towards the centre. The melt slows as it approaches the centre of

the mould, which is the hottest part of the mould, and it rises assisted by the effect of heat convection.

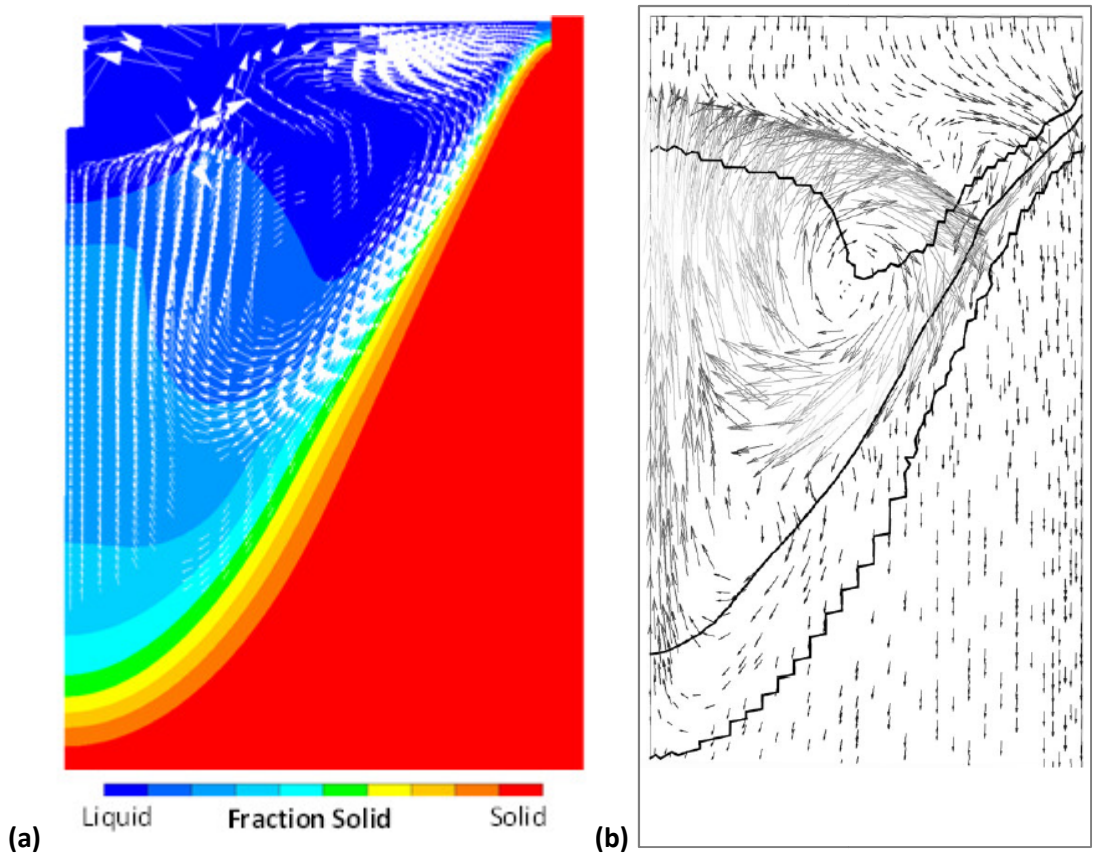

Figure 6-16 (a) Predicted flow pattern during DC casting of AZ80 alloy, generated using Alsim software, (b) Flow pattern given by flow velocity vectors in sump of 200mm diam. DC cast billet, isotherms of liquidus, coherency [Eskin and Katgerman, 2009].

The circulation is initiated by the distributor plate at the bottom of the inlet pipe, top left of Fig. 6-16 (a), and the jetting which results. The speed of the molten alloy flow is much higher as it enters the mould compared to the recirculating speed at the centre. This would suggest that the particles carried by the flow are more likely to be dropped by the flow at the centre. The flow at the very centre of the mould is vertical in direction and thus there is not the cross-flow present to transport the particles and they will therefore tend to settle out. The slowing of the flow and the vertical rise at the centre of the mould is also observed in the reported flow simulation [Eskin and Katgerman, 2009].

The contrast in melt flow velocities and directions across the billet diameter reinforces the free-floating dendrite theory [Vreeman and Incropera, 2000] and the

importance of individual thermal histories of particles irrespective of location [Eskin and Katgerman, 2009]. It is clear that fragments and inclusions may be picked up and carried by the high velocity flow at certain mould region and deposited elsewhere, most probably in the central region. However particles may become trapped at any point along the solidifying front if the flow brings them into contact with this interface [Yuan and Thomas, 2005].

Defects made up of an entrained oxide film and a number of the free floating intermetallic particles would also be likely to be carried and settle in the central region. The difference when it comes to entrained oxide films is that they 'trawl' through the melt collecting all the particles into clusters, as proposed by Watson and Kennedy [Watson et al., 2005; Kennedy and Wyatt, 2000].

6.3.2 Settling

An outcome from the flow pattern study in the previous section was that the defects are carried by the flow within the mould. The thermal history at the location at which they finally settle is not always a good prediction of the thermal history of the defect. Settling of particles may occur when they are large enough to do so. This is most likely to occur in the central region of the mould as it is at this location the flow is much reduced in velocity and possesses no horizontal motion as it rises. This mechanism was assessed by comparing the settling velocity of a particle against the velocity of the rising stream using data from the previous analysis.

To establish the typical motion of a particle in this region, the settling velocity was predicted using Stoke's Law, [Qian et al., 2001]. The time for an intermetallic phase particle to settle in static AZ80 melt contained in a 1.5 m deep crucible, replicating those used in practice, was predicted and the velocity with which it falls, which is to be used for this analysis, using equation:

$$settling\ time = \frac{2}{9}\frac{(\rho_{Al8Mn5} - \rho_{AZ80})d^2 g}{\mu}$$

Where ρ_{Al8Mn5} is the density of the intermetallic Al_8Mn_5 particles, $\rho_{AZ80}$is the density of the AZ80 melt, *d* is the diameter of the settling particle, g represents gravity and μ is the viscosity of the AZ80 melt.

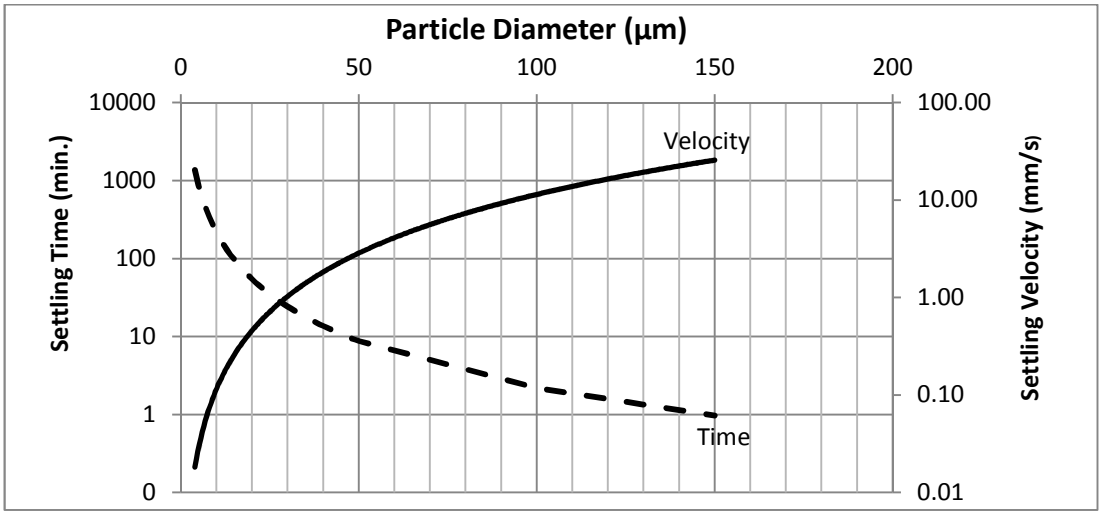

Figure 6-17 Settling velocity and time to settle in a crucible for a range of intermetallic (Al8Mn5) particle.

As predicted by the KWN model and experimentally measured average particle size at the centre the billet, the particles will grow from 5 µm up to a maximum 15 µm in radius, which can be predicted to fall with a velocity of around 0.1 mm/s up to about 1 mm/s. Comparing this with the typical velocity predicted for the circulating stream, observed to be around 2 mm/s, it is not expected that the particles will sink. This however is a very simplistic analysis and fails to consider the influence of fluctuating flow streams and agglomeration of particles and/or association with other entrained inclusions such as entrained oxide films in which cases the defects are much larger.

A more detailed analysis is possible when the combination of intermetallic particles and entrained oxide films is considered. However, the entrainment of an oxide film rarely occurs without the association of air trapped within the complex and folded oxide film, this would intuitively increase the buoyancy of any inclusion in a melt. This makes an assessment of the buoyancy of a defect comprising of the oxide film, intermetallic particle and air very complex but necessary to understand the resulting action.

A defect comprised of an entrained oxide film, intermetallic particles and air was shown to sink in Al alloys [Raiszadeh and Griffiths, 2011] and translation to the defects found in this study is easily achieved. It was calculated that an entrained oxide film of Al_2O_3, inflated by reduced pressure outside the casting resulting in a defect 180 µm in diameter, with an overall density of 200 kg/m^3 would achieve a terminal velocity of 38 mm/s [Raiszadeh and Griffiths, 2011]. This is comparable with MgO films (ρ_{MgO}= 3580 kg/m^3, $\rho_{Al_2O_3}$=3970 kg/m^3), when combined with air (density 1.225 kg/m^3), in an AZ80 melt which is slightly less dense than the Al alloy used in the calculation (ρ_{AZ80}=1790 kg/m^3 and ρ_{Al}=2331 kg/m^3). It would be expected using this analysis that the same sized defect when associated with Al_8Mn_5 particles and not inflated would reach a higher terminal velocity than that reported for the Al alloy. For the uninflated case, the defect with an equivalent diameter of 0.5 mm, was reported to reach a terminal velocity of 230 mm/s [Raiszadeh and Griffiths, 2011]. This size of defect is beyond those predicted in this study, Fig. 6-17, as this was done for particles in isolation. The defect comprised of oxide, air and particle in an Mg alloy would be expected to be of a similar size, around 0.5 mm, based on those found earlier in this study and therefore expected to settle with a similar velocity. Therefore, they can be shown to settle quite rapidly in the centre of the mould.

This indicates that the particle, oxide, air defect would be expected to settle in the central region of the billet as this is where the flow is at its slowest and has its lowest cross velocity which is more effective at carrying inclusions [Yuan and Thomas, 2005], so the defect is not carried away. The predicted settling velocities for a combined defect (one which consist of oxide film, air and particles) are much larger than those calculated in this study for particles alone, as the combined defects are typically much larger. Thus, it can be concluded that settling is most likely within the central region of the billet mould and that defects of the size characterised in this study would settle very quickly.

6.4 Discussion of Defect Formation Process

In attempt to prevent defects of the type found in this study from forming in the casting it is essential to understand the mechanism by which they form. This brings together individual processes that have been reported before such as the growth of intermetallic phases in alloys, oxides on free falling melt streams [Campbell, 2003] and flow patterns in DC moulds [Zhang, 2006].

The intermetallic particles present in the defects found in this study were simulated with considerable accuracy to predict those measured experimentally, section 6.1.1. By doing so a relationship between the cooling rate and resulting particle size was established to show that slower cooling rates resulted in larger particles, Fig. 6-4. However, translating these results to the case of a DC casting the predicted particle sizes, based on predicted cooling rates for certain billet positions, did not show a good correlation, section 6.1.2. This demonstrated that the actual factors affecting the growth of the particles were more than just the cooling rate for the location at which they were observed. This is comparable with the observations reported [Eskin et al., 2004] where the actual feature has a more complex thermal history than the measured/predicted thermal history of the location at which it was found. Particles are carried by the flow in the mould and recirculated, creating significantly longer periods of growth and through regions of very low cooling rates which were predicted to result in larger particles. Based on the calibrated KWN model the particles were shown to grow most rapidly at around 500°C, Fig. 6-7, which is near to the 550°C predicted to be the temperature at the mould centre during casting [Turski, 2013]. The particles are known to from at much higher temperatures than this (>600°C) and are expected to grow before reaching the predicted temperature for fastest growth. This mechanism would suggest the cause of the discrepancy between measured and predicted particle sizes.

The presence of the entrained oxide film appears to be the essential feature of the defects characterised in this study. Without which, the degree of clustering of the particles observed would not occur, sintering and coarsening may still occur to form

small clusters. Trawling of the entrained oxide film is the most likely cause of the coming together of the two phases. Entrainment of the oxide films primarily by the disruption of the inlet stream of melt which exists as a result of incomplete filling of the inlet pipe, Fig. 6-12, plus any previously entrained films that are present in the melt during preparation of the melt, represents a major problem. Filtering is essential in the production of high quality castings and in this study the filter used was shown to be effective at removing entrained films, Fig. 6-9. However, the use of a single filter upstream of the melt inlet into the mould is inadequate in removing the full range inclusions present in the final casting as is demonstrated by the presence of the defects found in this study. Improved filtering would most likely result in a step change in the quality of the casting produced.

Once in the mould, the melt was predicted to follow a recirculating path around the sump, Fig. 6-16(a), which matched with those reported [Eskin et al. 2004; Zhang, 2006]. This recirculation is a critical mechanism resulting in the defects observed in this study. The pattern begins as it emerges from the submerged entry nozzle, which it exits at high velocity and in a narrow, almost jet like, stream. Here the two inclusion phases become associated and then are carried by the melt flow which contacts the mould wall and then follows the profile of the sump towards the mould centre. Then the velocity of the flow slows as it rises towards the top of the mould. It is at this point when the flow slows that settling of the inclusions carried by the stream occurs. The velocity for settling is, as was discussed in section 6.3.2, much larger for the size of the combined defect found in this study than the predicted flow velocity and hence is expected to occur in the central region. This mechanism for settling in a region where the settling forces are greater than the flow carrying force accounts for the trend in defect locations shown in Fig. 5-13.

6.5 Summary

In summary the results of this study have suggested that the defects form as a result of many influencing factors. The cooling rate, the flow regime and velocity at the inlet of the melt in the mould, the resulting circulating path that the melt follows and settling were all modelled. The results indicated that the formation of the defects is principally initiated by the presence of the entrained oxide film.

The thermodynamic and kinetic modelling of the intermetallic phase demonstrated that the cooling rate does impact on the particle growth. Higher cooling rates will typically result in smaller particles. This relationship can not be directly transferred to the DC casting conditions where the feature of interest does not necessarily possess the thermal history of the location at which it is found [Eskin and Katgerman, 2009]. From this it is clear that the use of a constant cooling rate as the input for the KWN model is an over simplification of the particle growth process in the case of DC cast material. Accurate growth predictions could have been achieved using the same model but with a more accurate cooling rate profile, replicating that of a particle as it circulates around the mould sump.

Formation of the oxide film was suggested by the ALSIM model at the inlet pipe as it is fed to the mould. The simulations predicted the flow of melt to enter the inlet pipe at which point jetting may occur followed by incomplete filling of the inlet pipe itself, indicated by low velocity regions at which it can be interpreted as no fluid present and hence a free surface is created. This incomplete filling enables an oxide film to form on the free surface. This suggests a highly plausible mechanism by which the entrained oxide films are generated. The lack of filters after this stage means that any defect that is generated in the manner at this point will be free to enter into the melt.

Predicted flow patterns within the mould demonstrated that there is a strong recirculating flow. This flow is fast enough to carry any inclusions with it as it circulates in the mould. With knowledge that the central region of the mould is the hottest and where the flow slows to its lowest velocities, this would suggest that particle seeds would be washed through this region permitting extensive growth if

repeatedly exposed to this cycle. With the slowing of the flow at the centre of the mould it is likely here that those inclusions large enough to do so will settle out. Settling velocities were predicted for individual particles, however this analysis did not consider the effect of a defect comprising of intermetallic particles, oxide film and air.

The association between the oxide film and the intermetallic particles begins in the mould as both are carried by the circulating flow. Once the particles are collected by the oxide film they become entangled and are unlikely to separate. Both inclusions, usually found with associated entrained air, will then circulate and the particles will coarsen or sinter together until heavy enough to settle out of the flow. This settling is most likely to occur in the central region of the billet, resulting in the large defects at the locations found in this study.

7 Defect Prevention Methods

This section will discuss the lessons that can be learned as a result of this research project and will act as a deliverable to the sponsor organisation. This will include recommendations for improvement of the ultrasonic inspection process and also modifications to the casting process identified based on the findings this study. It will also discuss the feasibility of adopting these recommendations into the organisations practices in terms of financial and operational benefits.

7.1 Improved Inspection Technique

During this study a mid-term report was submitted to Magnesium Elektron, U.K. proposing recommendations that could improve the accuracy of their current ultrasonic inspection process. This section will summarise the points made in that report.

It was observed that the current inspection process did not follow a suitable calibration process by using an appropriate calibration block, additionally there was uncertainty around the accuracy of the results.

The following recommendations were made in order to address the observations made:

- Use of an accurate calibration block, manufactured to AA standard.
- Minimise the transfer difference used through the use of correct calibration block.
- Eliminate the practice of using manual gain adjustment to correct for transfer difference, to upgrade from A to AA standard and to correct for probe degradation.
- Modify the thresholds applied to the output of the ultrasonic data to provide more value than the current results offer.

It must be noted that most of the above recommendations have been implemented and are proving to be very beneficial. The modification of the thresholds applied to the results is permitting a more quantitative approach to product quality to be achieved by the use of the ultrasonic inspection.

An additional recommendation that has been discussed with Magnesium Elektron, U.K. technical staff is to apply suitable gating so that the distance of the defect below the surface will be recorded. This will enable a more accurate defect location to be captured without requiring any post scan analysis. This would again permit a more quantitative assessment of billet quality.

7.2 Recommended Improvements to Casting Practice

This section will recommend improvements to the casting equipment in order to improve the quality of the cast billets based on the findings of this study. These recommendations will be discussed further in the next section focusing on the operational and financial implications where applicable.

7.2.1 Filtering

A change in filter type to bonded ceramic particle filters is recommended. Current filtering practice was identified as being adequate but with scope for improvement. If an improvement in quality is sought, filtering must also be improved. The use of bonded particle ceramic filters is most commonly used in continuous or semi-continuous casting processes and would be significantly more effective. The use of steel mesh filters, as are currently used, is usually restricted to gravity and shape casting processes.

Additional filters should be included, if the current casting arrangement is to be retained. Filtering downstream of the inlet tube should be considered. This may take the form of a filter fitted around the submerged entry nozzle which may also be used as a method of flow conditioning, Fig. 7-1.

7.2.2 Melt Transfer

Melt transfer was identified as the primary cause of oxide entrainment defects during the current casting process, in this study. The existing launder and inlet pipe configuration has its limitations with regard to casting quality. The root cause of this is with regard the method of melt flow control.

A potential modification to the current melt transfer system is to adopt a laser level detector coupled with an automated crucible tilting system. However, the results of this study suggest that the same problem will persist with the current launder and inlet pipe arrangement.

Modification to the submerged entry nozzle offers an easy and inexpensive route to improved casting quality through control of the melt flow within the mould [Zhang,

2009]. A range of advanced nozzle designs have been trialled, including deliberate rotation of the melt as it enters the mould by designing the submerged entry nozzle [Kholmatov et al., 2007]. A simpler design identified to overcome the problems established in this study is the use of inverted stopper, Fig. 7-1. This type of flow control has the advantage of ensuring the inlet pipe is completely filled and the flow into the mould is restricted at a submerged location. With this geometry the stopper can also be selected to manipulate the direction of the flow into the mould. The circular flow patterns that establish in the mould may be enhanced or prevented by the stopper geometry as desired. Initial modelling work carried out as part of this study demonstrates that the flow regime in the mould would be very different to those with the traditional stopper configuration.

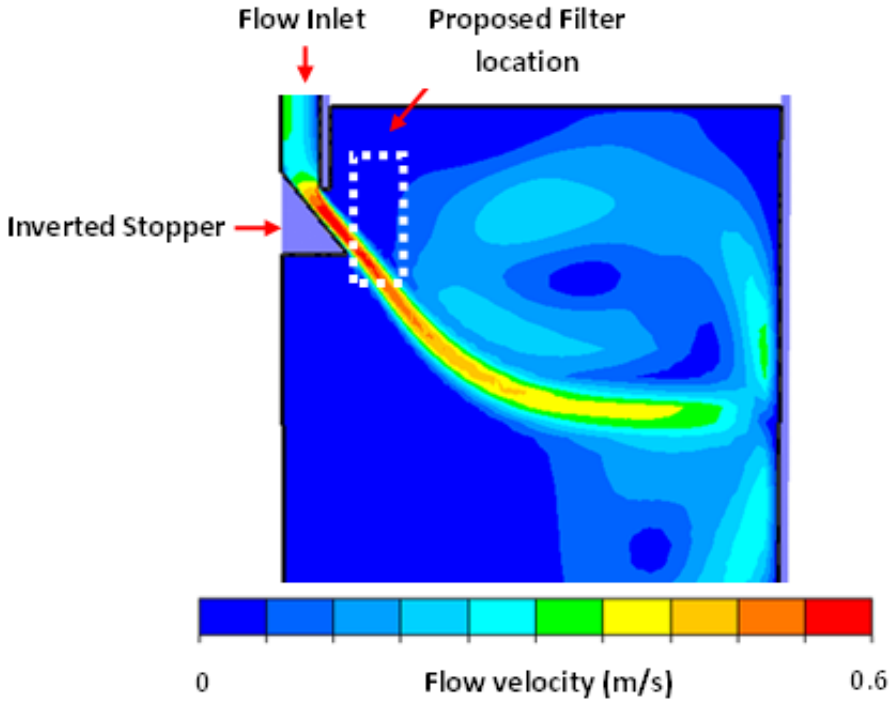

Figure 7-1 Inverted stopper simulation

More sophisticated melt transfer methods exist and are commonly used in the aluminium industry. The use of siphoning and electromagnetic pumping can provide an alternative method of melt transfer from the crucible to the mould and are common in the magnesium industry [McGlade and Baker, 2013]. These two approaches provide much greater control over the flow rate and remove the potential to cause oxide film entrainment, as discussed in section 2.2.5.3.

An increase in quality could also be achieved by the employment of a melt shearing device as discussed in section 2.2.4.1. When employed this would offer reduced oxide film defects, reduced intermetallic particle size and a more uniform grain structure by breaking up an inclusion in the melt. This option would provide a step change in casting quality and would require very little modification to the current filtering and casting arrangements. Extensive trials would be necessary to optimise the casting parameters but the continued production of high quality billets would be possible by this method.

Magnesium Elektron, U.K have been directed by the interim results of this research project. By highlighting the importance of the melt transfer equipment on the final quality of the cast product this research has suggested that significant investment in this area will be beneficial. Two approaches have been looked at in terms of eradicating oxide films:

1. Improvements in existing filtration

2. Improvements in melt transfer from the crucible to the moulds.

Work in both areas is still on-going but improvements have been made. Changes have been implemented in terms of launder and filter design. This has resulted, on average in a 10 % reduction in scrap rates for material required to AA ultrasonic standard.

7.3 Feasibility Study of Casting Equipment Modifications

A range of solutions exist to improve the quality of the casting by preventing defects of the type found in this study from forming. These offer a much higher yield in marketable product from each production run. The financial benefits of this are significant and it is hoped that this saving could be reflected in the market price of the cast material, making it more attractive to more customers. This section will discuss the potential benefits that could be realised, while also considering the costs involved in doing so and the implications this may have on the production process.

7.3.1 Financial Considerations

The previously suggested improvements range in cost to implement. The use of new filters may only require a small additional cost. In comparison the investment in a new electromagnetic pumping or melt shear unit presents a substantial investment.

The financial benefit of reducing the rejection rate will be realised in many ways. The costs associated with production of the product will be greatly reduced, firstly due to the reduction in man hours, required to produce the billet, which are effectively lost when the billet is scrapped and due to the manpower required to rework to material. The billet itself can be recycled thus reworking does not result in a loss of the value associated with material costs. The rejection of a billet also presents a delay to the production schedule. This delay has implications for the other production processes requiring use of the same production facilities and can damage the customer relationship.

The investment in new equipment offers a long term opportunity for continued higher billet quality. This will be recognised by customers in the market for forging feedstock and enhance the reputation of the organisation, building a reputation for reliable high quality products. Combined with a potential reduction in market price of the cast material, the sales of this product will reflect the improvements made, providing a return on the initial investment.

The production of higher quality product can also permit the entrance into new markets, those which demand very strict quality requirements. The financial return on doing so would be large as there is very little expense to achieve this as the same equipment can be used. Such high quality products can also be sold at a premium price. In the context of this research project the new market may be aerospace applications, which is a growing market.

The payback period for this project is about 9 months, this includes the EngD support and design work and equipment rebuilds that Magnesium Elektron, UK have produced to implement improvements in melt cleanliness. Changes to the

melt transfer system could potentially improve yields further, the costs required to implement such changes would be expected to have a payback time of between 1 to 2 years. Such changes are currently being reviewed.

7.3.2 Operational Implications

The use of a new filter does not require any operation changes as they will be a direct replacement for the filters used at present. The only change may be to the fitting and removal of filters before and after casting. This could be managed by training the relevant staff on correct and safe operating procedures to ensure maximum effectiveness when implemented. Explaining to the staff the benefit of the new filters may also ensure they embrace the changes and work constructively to achieve the desired outcome.

The use of a laser detection unit or electromagnetic pump may require specialist training and a result in a change of production method. This would require significant retraining for the equipment operators, which would best be carried out by the equipment manufacturer representative. It is essential that sufficient training is provided as incorrect usage of new equipment may not result in any improvement in quality.

Operationally new equipment can require new training and a familiarisation stage for the staff members. However, continually meeting the required production schedule will provide the staff with a satisfaction and pride in their work, as opposed to the displeasure realised that what they have produced is scrapped and must be repeated.

8 Conclusions and Key Points

A brief summary will be presented in this section which will capture all of the key outcomes of this study. Additionally a reflection on the objectives of this research project will be presented identifying which of these were met. This will be concluded with a short list of pertinent outcomes that have been expressed in this thesis.

8.1 Conclusions

This study identified that the ultrasonic inspection method is a reliable technique for defect detection only, sizing and characterisation is not possible. When used in combination with XCT imaging a fuller characterisation of the defects was possible. These defects were large clusters of intermetallic phase Al_8Mn_5 particles entangled with entrained oxide MgO films. These defects ranged from 0.5 mm up to 10 mm in size. Often the defect, assumed to be a single feature, was observed to be a number of oxide fragments.

Computer simulations suggested that oxide films are free to form and become entrained during casting as molten metal was transfer into the mould. The oxide film would be free to form on the outside of the falling stream and fracture as the result of any disruption in flow. The oxide film would most likely become entrained and enter into the mould ultimately becoming a defect feature in the cast material.

That flow regimes in the DC casting mould are responsible for supporting the growth of the intermetallic particles found in the defects. Nucleation of these particles may occur either within the crucible before or during pouring, however most growth occurs when in the DC mould. Thermodynamic and kinetic modelling demonstrated that the cooling rate at a specific billet location did not match with the expected particle size predicted by the KWN model when input with a constant cooling rate. This suggested that the growth of these particles is a complex process influenced by more than the cooling rate at a single point alone. The predicted flow pattern in the mould demonstrates that there is a degree of recirculation which suspends the particles in the melt before they are large enough to settle out of the flow. This is recognised to permit continued growth and result in particles much larger than would be expected if no recirculation took place. The same flow also brings together the entrained films and particles as it carries them both around the mould. There is no strong evidence for the nucleation of the intermetallic particles on the entrained oxide film.

The locations of the unacceptably large defects were always found to be in the central region of the billet, this again is due to the flow conditions in the mould.

The predicted flow pattern and velocity indicated the central region of the billet to be greatly reduced in velocity and in an almost vertically upward direction. These conditions offer the large defects the greatest opportunity to settle as there is no cross-flow velocity to wash and carry them away, which is more effective at carrying inclusions than a vertical flow. Thus settling is expected to be most likely in the central region, which corresponds with the trend established for the defect locations in this study.

In summary, if the entrained films are prevented from entering the melt the likelihood of such films leading to clustering of the intermetallic particles will be greatly reduced. This is because the entrained oxide clearly has a trawling effect, causing the intermetallic particles to be concentrated together and in some cases leading to contact and sintering of these particles. The net result of reducing oxide entrainment is thus expected to be a much cleaner casting with both fewer brittle oxide films and a reduced tendency for intermetallic clustering.

Finally, the limitations of the ultrasonic inspection method as used at Magnesium Elektron have been identified and improvements to current practice have been recommended. Through improved use of the ultrasonic inspection equipment and the reduction of the defects present, the rejection rate will be reduced, less material will be wrongly scrapped and the continued production of high quality material will be possible.

8.2 Review of Project Objectives

This study set out to identify methods to produce high quality forging feedstock and reduce the rejection rate currently experienced. Also to establish a reliable inspection technique suitable for the demands of an industrial environment.

A reduction in the scrappage rate could not be demonstrated however substantial recommendations were generated to achieve this goal. The production of higher quality material is also possible as a result of the same findings from this study and backed up by the available literature identified.

The ultrasonic inspection technique once configured and used in the correct manner as described in section 7.1 is a reliable defect detection method. Based on the improvements realised by implementing some of the recommendations made during this research this method is proving to be a reliable technique.

Since it has been indicated in this study that both the inspection and production methods can be improved this will lead to cleaner castings and more accurate inspection, both of which contribute towards the project objectives.

8.3 Key Points

Some of the main outcomes from this study are presented below,

- Ultrasonic inspection can reliably detect defects but not characterise them
- XCT is a very effective imaging technique able to characterise the entrained oxide and particle cluster type defect
- The defects found in the DC cast material are oxide film and intermetallic particle clusters
- Entrained oxide films occur due to the presence of a free falling stream of melt
- Intermetallic particle growth is the result of a complex thermal history and takes place in the DC mould
- The two phases of the defect combine after being brought together in the melt flow
- Settling of the defects occurs within the central region of the melt where the melt flow conditions are favourable
- Better quality castings can be achieved by careful control of the melt during transfer and improved filtering

9 Further Work

The results of this study have made some progress towards understanding the defects that form in DC cast AZ80 alloy. However, further research must be carried out to increase the knowledge of the use of inspection techniques and reducing defects in DC cast material in attempt to produce high quality castings. This section will present some potential areas for future studies that would further the knowledge gained from this study.

1. The ultrasonic inspection method was shown to be capable of detecting defects but was limited to indicating location. Development of a suitable technique which could characterise defects at the same time as meeting the demands of a production process would be massively beneficial to the quality of the final cast material. It would permit a more informed decision to be taken as to the materials cleanliness.

2. The flow pattern in the DC casting mould was shown to have a significant impact on the microstructure. A study to assess the impact of changing flow patterns on the microstructure would demonstrate further possible defect prevention methods.

3. The growth of the intermetallic phase particles were modelled in this study using the modified KWN model. Extending this to complete microstructural modelling (including the formation of the magnesium dendrites) would establish the impact of the defects on the microstructure and the effect of the developing microstructure on the final defect shape and location. Combining this with suggestion number 2 above, a non-constant cooling rate accurately replicating the particles complex thermal history influenced by fluid flow would be a first step in achieving this.

4. It is important to understand the relationship between the entrained oxide film and intermetallic phases and understand the influence (if any) of particles in the melt and nucleation of the oxide film.

5. This research identified that similar defects were present in ZW3 alloy, however the extension of this to other alloy types would be beneficial.

References

Abramoff et al., 2004 — M. Abramoff, P. Magalhaes, S. Ram, Biophotonics International, 11 (2004) 36-42, *Image Processing with ImageJ*

Aguilar et al., 2004 — J. Aguilar, M. Fehlbier, A. Ludwig, A. Buhrig-Polaczek, P. Sahm, Material Science and Engineering: A, 375-377 (2004) 651-655, *Non-equilibrium globular microstructure suitable for semisolid casting of light metal alloys by rapid slug cooling technology*

Aihua et al., 2008 — H. Aihua, C. Shusen, L. Yanchun, China Foundry, 5 (2008) 16-19, *Double oxide film defects in Ni-based super-alloy castings*

Asthana and Tewari, 1993 — R. Asthana, S. Tewari, Journal of Material Science, 28 (1993) 5414-5425, *The engulfment of foreign particles by a freezing interface*

Baker, 1992 — H. Baker, *ASM Handbook*, 3 (1992) 2-285

Bakke et al., 1994 — P. Bakke, T. Engh, E. Bathen, D. Oymo, A. Nordmark, Materials and Manufacturing Processes, 9 (1994) 111-138, *Magnesium filtration with ceramic foam filters and subsequent quantitative microscopy of the filters*

Banks et al., 1962 — B. Banks, G. Oldfiled, H. Rawding, *Ultrasonic Flaw Detections in Metals*, Iliffe Books Ltd, (1962)

Bennon and Incropera (a), 1987 — W. Bennon, F. Incropera, International Journal of Heat and Mass Transfer, 30 (1987) 2161-2170, *A continuum model for momentum, heat and species in binary solid-liquid phase change systems – 1. Model Formulation*

Bettles and Gibson, 2005 — C. Bettles and M. Gibson, JOM (2005) 46-49, *Current wrought magnesium alloys: strengths and weaknesses, research summary*

Bian et al., 2009	Z. Bian, I. Bayandorian, H.W. Zhang, G. Scamans, Z. Fan, Materials Science and Technology, 25 (2009) 559-606, *Extremely fine and uniform microstructure of magnesium AZ91D alloy sheets produced by melt conditioned twin roll casting*
Borman , 2009	S. Borman, University of South California, Los Angeles, (2009), *The expectation maximisation algorithm: A short tutorial*
Braszczynska-Malik, 2009	K. Braszczynska-Malik, Journal of Alloys and Compounds 477 (2009) 870-876, *Discontinuous and continuous precipitation in magnesium-aluminium type alloys*
Caceres, 1995	C. Caceres, Scripta Metallurgica et Materialia, 32 (1995) 1851-1856, *On the effect of macroporosity on the tensile properties of the Al-7% Si-0.4% Mg casting alloy*
Caceres et al., 2002	C. Caceres, C. Davidson, J. Griffiths, C. Newton, Material Science and Engineering: A, 325 (2002) 344-355, *Effects of solidification rate and ageing on the microstructure and mechanical properties of AZ91 alloy*
Caceres et al., 2005	C. Caceres, J. Griffiths, A. Pakdel, C. Davidson, Material Science and Engineering: A, 402 (2005) 258-268, *Microhardness mapping and the hardness-yield strength relationship in high-pressure diecast magnesium alloy AZ91*
Campbell, 1993	J. Campbell, *Castings*, Butterworth-Heinemann, 1993
Campbell, 2001	J. Campbell, *Complete Casting Handbook: Metal Casting Processes, Techniques and Design*, Butterworth-Heinemann, 2001
Campbell, 2006	J. Campbell, Journal of Materials Science and Technology, 22 (2006) 127-145, *Entrainment Defects*
Cao and Campbell, 2004	X. Cao, J. Campbell, International Journal of Cast Metals Research, 17 (2004) 1-11, *Effect of precipitation and*

sedimentation of primary α-Fe phase on liquid metal quality of cast Al-11.1Si-0.5Mg alloy

Cao and Campbell, 2005 — X. Cao and J. Campbell, Canadian Metallurgical Quarterly, 44 (2005) 435-448, *Oxide inclusion defects in Al-Si-Mg cast alloys*

Cao et al., 2004 — X. Cao, N. Saunders, J. Campbell, Journal of Materials Science, 39 (2004) 2303-2314, *Effect of iron and manganese contents on convection-free precipitation and sedimentation of primary α-Al(FeMn)Si phase in liquid Al-11.5Si-0.4Mg alloy*

Cao et al., 2007 — P. Cao, M. Qian, D. StJohn, Scripta Materialia, 56 (2007) 633-636, *Mechanism for grain refinement of magnesium alloys by superheating*

Capineri et al., 1992 — L. Capineri, H. Tattersall, J. Temple, M. Silk, Ultrasonics, 30 (1992) 275-288, *Time of flight diffraction tomography for NDT applications*

Cashion et al., 2002 — S. Cashion, N. Ricketts, P. Hayes, Journal of Light Alloys, (2002) 37-42, *Characterisation of protective surface films formed on molten magnesium protected by air SF_6 atmospheres*

Celotto, 2000 — S. Celotto, Acta Materialia, 48 (2000) 1775-1787, *TEM study of continuous precipitation in Mg-9 wt%Al-1 wt%Zn alloy*

Chaijaruwanich et al., 2007 — A. Chaijaruwanich, P. Lee, R. Dashwood, Y. Youssed, H. Nagaumi, Acta Materialia, 55 (2007) 285-293, *Evolution of pore morphology and distribution during the homogenization of direct chill cast Al-Mg alloys*

Chalmers, 1964 — B. Chalmers, *Principles of Solidification,* John Wiley & Sons, 1964

Chen and Wei, 2007	Y. Chen, P. Wei, Materials Transactions, 48 (2007) 3181-3189, *Diagnosis and analysis of oxide films in cast magnesium alloys by ultrasonic treatment*
Dahle et al., 2001	A. Dahle, Y. Lee, M. Nave, P. Schaffer, D. StJohn, Journal of Light Metals, 1 (2001) 61-72, *Development of the as-cast microstructure in magnesium aluminium alloys*
Dahle et al. (b), 2001	A. Dahle, S. Sannes, D. StJohn, H. Wetgengen, Journal of Light Metals, 1 (2001) 99-103, *Formation of defect bands in high pressure die cast magnesium alloys*
Davis and Elliot, 2006	G. Davis, J. Elliot, Materials Science and Technology, 22 (2006) 1011-1018, *Artefacts in X-ray microtomography of materials*
Davis, 1993	J. Davis, ASM Speciality Handbook, *Aluminium and Aluminium Alloys,* ASM International, 1993
Deutsch, 2000	K. Deutsch, WCNDT Conference Shanghai, 2000, *Automated ultrasonic pipe weld inspection*
Djurdjevic et al., 2010	M. Djurdjevic, Metalurgija – Journal of Metallurgy, 16 (2010) 63-76, *Melt quality control at aluminium casting plants*
Doege et al., 2001	E. Doege, W. Sebastian, K. Dröder, G. Kurz, Innovations in Processing and Manufacturing of Sheet Materials TMS Annual Meeting, (2001) 53-60, *Increased Formability of Mg sheets using Temperature Controlled Deep Drawing Tools*
Drinkwater and Wilcox, 2006	B. Drinkwater, P. Wilcox, NDT&E International, 39 (2006) 525-541, *Ultrasonic arrays for non-destructive evaluation: A review*
Du et al., 2003	Y. Du, Y. Chang, B. Huang, W. Gong, Z. Jin, H. Xu, Z. Yuan, Y. Liu, Y. He, F. Xie, Materials Science and Engineering: A, 363

(2003) 140-151, *Diffusion coefficients of some solutes in fcc and liquid Al: Critical evaluation and correlation*

El-Sayed et al., 2011 — M. El-Sayed, H. Salem, A. Kandeil and W. Griffiths, Metallurgical and Material Transactions: B, 42B (2011) 1104-1109, *Effect of holding time before solidification on double-oxide film defects and mechanical properties of aluminium alloys*

Engh, 1992 — T. Engh, *Principles of Metal Refining*, Oxford Science Publications, 1992

Eskin et al., 2004 — D. Eskin, J. Zuidema Jr., V. Savran, L. Katgerman, Material Science and Engineering: A, 384 (2004) 232-244, *Structure formation and macrosegregation under different process conditions during DC casting*

Eskin and Katgerman, 2009 — Eskin and Katgerman, Materials Technology, 24 (2009) 152-156, *Solidification phenomena related to direct chill casting of aluminium alloys: fundamental studies and future challenges*

Fan et al., 2009 — Z. Fan, Y. Wang, M. Xia, S. Arumuganathar, Acta Materialia 57 (2009) 4891-4901, *Enhanced heterogeneous nucleation in AZ91D alloy by intensive melt shearing*

Fan et al., 2010 — Z. Fan, M. Xia, Y. Wang, S. Arumuganathar, G. Scamas, Materials Science Forum, 649 (2010) 301-306, *Shear enhanced heterogeneous nucleation in AZ91D alloy*

Feldkamp et al., 1984 — L. Feldkamp, L. Davis, J. Kress, Journal of the Optical Society of America: A, 1 (1984) 612-619, *Practical cone beam tomography*

Feng and Froyen, 2000 — C. Feng, L. Froyen, Journal of Material Science, 35 (2000) 837-850, *Microstructure of in situ Al/TiB_2 MMCs prepared by a casting route*

Fisher, 1978	P. Fisher, International Metals Review, 6 (1978)269-285, *Production properties and industrial uses of magnesium and its alloys*
Flemings, 1974	M. Flemings, *Solidification Processing*, McGraw-Hill, 1974
Fox and Campbell, 2000	S. Fox and J. Campbell, Scripta Materialia, 43 (2000) 881-886, *Visualisation of oxide film defects during solidification of aluminium alloys*
Fox and Lardner, 1943	F. Fox, E. Lardner, (1943), *An investigation of the effects of precipitation treatment of binary magnesium-aluminium alloys*
Friedrich and Mordike, 2004	H. Friedrich, B. Mordike, *Magnesium Technology: Metallurgy, Design Data, Applications*, Springer, 2004
Gaines et al., 1996	L. Gaines, R. Cuenca, F. Stodolsky, S. Wu, Conference on Automotive Technology Development, Michigan, 1996, *Potential automotive uses of wrought magnesium alloys*
Glicksman and Hills, 2001	M. Glicksman, R. Hills, Philosophical Magazine A, 81 (2001) 153-159, *Non-equilibrium segregation during alloy soldification*
Gjestland et al., 1996	H. Gjestland, H. Westengen, S. Plahte, Proceedings of the Third international Mg conference, 1996, *Use of SF_6 in the magnesium industry: an environmental challenge*
Grandfield and McGlade, 1996	J. Grandfield, P. McGlade, Materials Forum (Australia), 20 (1996) 29-51, *DC casting of aluminium: Process behaviour and technology*
Grass et al., 2000	M. Grass, Th. Kohler, R. Proska, Physics in Medicine and Biology, 45 (2000) 329-347, *3D cone-beam CT reconstruction for circular trajectories*

Griffiths and Lai, 2007	W. Griffiths, N. Lai, Metallurgical and Materials Transactions A, 38 (2007) 190-196, *Double oxide film defects in cast magnesium alloys*
Guang et al., 2009	H. Guang, M. Guolong, L. Xiangfa, Journal of Alloys and Compounds, 486 (2009) 136-141, *Effect of manganese on the microstructure of Mg-3Al alloy*
Guo et al., 2005	Z. Guo, N. Saunders, A.P. Miodownik, J. Schille, Material Science and Engineering: A, 413-414 (2005) 465-469, *Modelling of materials properties and behaviour critical to casting simulation*
Halmshaw, 1991	R. Halmshaw, *Non-Destructive Testing*, 2nd Edition, Edward Arnold, 1991
Haghayeghi et al., 2008	R. Haghayeghi, Y. Liu, Z. Fan, Solid State Phenomena, 141-143 (2008) 403-408, *Melt conditioned direct chill casting (MC-DC) of wrought Al-alloys*
Herman, 1995	G. Herman, Real-Time Imaging, 1 (1995) 3-18, *Image reconstruction from projections*
Hislop, 1969	J. Hislop, Non-Destructive Testing, 2 (1969) 183-192, *Flaw size evaluation in immersion ultrasonic testing*
Hsieh, 2009	J. Hsieh, *Computed Tomography: Principles, Design, Artefacts and Recent Advances*, Society of Photo-Optical Instrumentation Engineers (2009)
Jones, 1993	H. Jones, Ultrasonics, 31 (1993) 353-360, *Recent activity in ultrasonic tomography*
Kainer, 2003	K. Kainer, *Magnesium Alloys and Technology*, Wiley-VCH, 2003
Kastner et al., 2010	J. Kastner, B. Harrer, G. Reuena, O. Brunke, NDT&E International, 43 (2010) 599-605, *A comparative study of*

high resolution cone beam X-ray tomography and synchrotron tomography applied to Fe- and Al- alloys

Katgerman et al., 2005 — L. Katgerman, J. Zuidema Jr, Light Metals, (2005) 927-931, *Upstream fluid flow particle removal*

Kaye and Street, 1982 — A. Kaye, A. Street, *Die Casting Metallurgy*, Butterworth-Heinemann, 1982

Ke, 2004 — Wei Ke, Magnesium – Science, Technology and Applications, Proceedings of International Conference on Magnesium, Beijing, 2004

Kennedy and Wyatt, 2000 — A. Kennedy, S. Wyatt, Composites Science and Technology, 60 (2000) 307-314, *The effect of processing on the mechanical properties and interfacial strength of aluminium/TiC MMCs*

Kholmatov et al., 2007 — S. Kholmatov, S. Takagi, L. Jonsson, P. Jonsson, S. Yokoya, ISIJ International, 47 (2007) 80-87, *Development of flow field and temperature distribution during changing divergent angle of the nozzle when using swirl flow in a square continuous casting billet mould*

Khvastunkov, 2004 — M. Khvastunkov, J. Leggoe, Material Science and Engineering: A, 383 (2004) 347-355, *Modelling the influence of the nature of spatial heterogeneity on the deformation and failure of porous ductile alloys*

Kirkpatrick, 1975 — R. Kirkpatrick, American Mineralogist, 60 (1975) 798-814, *Crystal growth from the melt: A review*

Kleiner et al., 2003 — M. Kleiner, M. Geiger, A. Klaus, CIRP Annals - Manufacturing Technology, 52 (2003) 521 – 542, *Manufacturing of lightweight components by metal forming*

Krumm et al., 2008	M. Krumm, S. Kasperl, M. Franz, NDT&E International, 41 (2008) 242-251, *Reducing non-linear artifacts of multi-material objects in industrial 3D computed tomography*
Kulekci, 2008	M. Kulekci, International Journal of Advanced Manufacturing Technology, 39 (2008) 851-865, *Magnesium and its alloys applications in automotive industry*
Lai et al. 2009	W. Lai, Y. Li, Y. Hsu, S. Trong, W. Wang, Journal of Alloys and Compounds, 476 (2009) 118-124, *Aging behaviour and precipitate morphologies in Mg-7.7Al-0.5Zn-0.3Mn (wt.%) alloy*
Langer and Schwartz, 1980	J. Langer and A. Schwartz, Physical Review A, 21 (1980) 948-958, *Kinetics of nucleation in near-critical fluids*
Larouche and Brochu, 1996	A. Larouche and C. Brochu, Light Metals, Canadian Institute of Mining, Metallurgy and Petroleum, (1996) 597-604, *Solidification Conditions in Aluminium D.C. Sheet ingot: Understanding and Control*
Laser et al., 2006	T. Laser, M. Nurnberg, A. Janz, Ch. Hartig, D. Letzig, R. Schmid-Fetzer, R. Bormann, Acta Materialia, 54 (2006) 3033-3041, *The influence of manganese on the microstructure and mechanical properties of AZ31 gravity die cast alloys*
Lee et al., 2002	P. Lee, R. Atwood, R. Dashwood, H. Nagaumi, Material Science and Engineering: A, 328 (2002) 213-222, *Modelling of porosity formation in direct chill cast aluminium-magnesium alloys*
Li et al., 2002	D. Li, J. Luo, S. Wu, Z. Xiao, Y. Mao, X. Song, G. Wu, Journal of Materials Processing Technology, 129 (2002) 431-434, *Study on the semi-solid rheocasting of magnesium alloy by mechanical stirring*

Li et al., 2011	S. Li, K. Sadayappan and D. Apelian, International Journal of Cast Metals Research, 24 (2011) 88-95, *Characterisation of hot tearing in Al cast alloys: methodology and procedures*
Lifshitz and Slyozov, 1961	I. Lifshitz and V. Slyozov, Journal of Physics and Chemistry of Solids, 19 (1961) 35-50, *The kinetics of precipitation from supersaturated solid solutions*
LLewandowski et al., 1989	J. LLewandowski, C. Liu, Materials Science and Engineering: A, 107 (1989) 241-255, *Effects of matrix microstructure and particle distribution on fracture of an aluminium metal matrix composites*
Lloyd et al., 1989	D. Lloyd, H. Lagace, A. McLeod and P. Morris, Materials Science and Engineering: A, 107 (1989) 73-80, *Microstructural aspects of aluminium-silicon carbide particulate composites produced by a casting method*
Locatelli and Liu, 2010	J. Locatelli, G. Liu, Light Metals 2010, 639-650, *Crucible transfer by siphoning: A review of the benefits and the latest technology*
Lu et al., 2000	Y. Lu, Q. Wang, W. Ding, X. Zeng, Y. Zhu, Materials Letters, 44 (2000) 265-268, *Fracture behaviour of AZ91 magnesium alloy*
Ludlow, 2007	D. Ludlow, *Influence of Direct Chill casting Parameters on the structure and Properties of Magnesium Alloys*, EngD Thesis, 2007, University of Manchester
Lutjering and Williams, 2007	G. Lutjering, J. Williams, *Titanium*, 2nd Edition, Springer, 2007
Mackie, 2011	D. Mackie, *Automated Ultrasonic Inspection – recommendations report*, Internal Report, April 2011
Makarov et al., 1999	S. Makarov, R. Ludwig and D. Apelian, Measurement science and technology, 10 (1999) 1047-1053,

Electromagnetic visualisation technique for non-metallic inclusions in a melt

Maire et al., 2001 — E. Maire, J.Y. Buffiere, L. Slavo, J.Blandin, W. Ludwig, J. Letang, Advanced Engineering Materials, 3 (2001) 539-546, *On the Application of X-ray Microtomography in the field of Materials Science*

Maire et al., 2006 — E. Maire, J. Grenier, D. Daniel, A. Baldacci, H. Klocker, A. Bigot, Scripta Materialia, 55 (2006) 123-126, *Quantitative 3D characterisation of intermetallic phases in an Al-Mg industrial alloy by X-ray microtomography*

Matys, 1988 — Paul Matys, PhD Thesis, University of Essen, 1985, *Fluid Flow and heat transfer in continuous casting processes*

McGlade and Baker, 2013 — P. McGlade, P. Baker, *Magnesium direct chill casting: A comparison with aluminium*, in Essential Readings for Light Metals: Cast Shop for Aluminium Production, Volume 3, John Wiley & Sons Inc, 2013

Men et al., 2010 — H. Men, B. Jiang, Z. Fan, Acta Materialia, 58 (2010) 6526-6534, *Mechanisms of grain refinement by intensive shearing of AZ91 alloy melt*

Monroe, 2005 — R. Monroe, *Porosity in castings*, American Foundry Society Transactions, 2005

Mordike and Ebert, 2001 — B. Mordike, T. Ebert, Materials Science and Engineering: A, 302 (2001) 37-45, *Magnesium: Properties-applications-potential*

Mortensen, 1999 — D. Mortensen, Metallurgical and Materials Transactions B, 30 (1999) 119-133, *A mathematical model of the heat and fluid flows in direct-chill casting of aluminium sheet ingots and billets*

Murphy et al., 1997 — A. Murphy, S. Howard and T. Clyne, Key Engineering Materials, 127-131 (1997) 919-928, *The effect of particle*

clustering on the deformation and failure with SiC particles: A quantitative study

Nadella et al., 2008 — R. Nadella, D. Eskin, Q. Du, L. Katgerman, Progress in Materials Science, 53 (2008) 421-480, *Macrosegregation in direct-chill casting of aluminium alloys*

Nicolas and Deschamps, 2003 — M. Nicolas, A. Deschamps, Acta Materialia, 51 (2003) 6077-6094 *Macrosegregation in direct-chill casting of aluminium alloys*

Nicoletto et al., 2010 — G. Nicoletto, G. Anzelotti, R. Konecna, Procedia Engineering 2 (2010) 547-554, *X-ray computed tomography vs. metallography for pore sizing and fatigue of cast Al-alloys*

Niu et al., 1990 — A. Niu, C. Han, W. Wee, Journal of X-ray Science and Technology, 2 (1990) 95-116, *A new three dimensional reconstruction method using algebraic reconstruction techniques*

Ohno et al., 2006 — M. Ohno, D. Mirkovic, R. Schmid-Fetzer, Acta Materialia, 54 (2006) 3883-3891, *Liquidus and solidus temperatures of Mg-rich Mg-Al-Mn-Zn alloys*

Ohno et al. (b), 2006 — M. Ohno (b), D. Mirkovic, R. Schmid-Fetzer, Material Science and Engineering: A, 421 (2006) 328-337, *Phase equilibria and solidification of Mg-rich Mg-Al-Zn alloys*

Ono, 2003 — Y. Ono, O. Moisan, C. Jen, Ultrasonics, Ferroelectrics and Frequency Control, 50 (2003) 1711-1721, *Ultrasonic techniques for imaging and measurements in molten aluminium*

Polmear, 1994 — I. Polmear, Materials science and technology, 10 (1994) 1-16, *Overview: Magnesium alloys and applications*

Polmear, 1996 — I. Polmear, *Light Alloys: Metallurgy of the Light Metals,* 3rd Edition, John Wiley & Sons, 1996

Porter and Easterling, 1992	D. Porter, K. Easterling, Phase Transformation in Metal and Alloys, 2nd Edition, Stanley Thornes, 1992
Qian et al., 2001	M. Qian, L. Zheng, D. Graham, M. Frost, D. StJohn, Journal of Light Metals, 1 (2001) 157 – 165, *Settling of undissolved zirconium particles in pure Mg melts*
Qian et al., 2003	M. Qian, D. Graham, L. Zheng, D. StJohn and M. Frost, Materials Science and Technology, 19 (2003) 156-162, *Alloying of pure magnesium with Mg-33.3wt%Zr master alloy*
Raiszadeh and Griffiths, 2001	R. Raiszadeh, W. Griffiths, Metallurgical and Materials Transactions B, 42 (2011) 133-143, *The effect of holding aluminium alloys in oxide film content*
Ramirez et al., 2008	A. Ramirez, M. Qian, B. Davis, T. Wilks, D. StJohn, Scripta Materialia, 59 (2008) 19-22, *Potency of high-intensity ultrasonic treatment for grain refinement of Mg alloys*
Ravi et al., 2008	K. Ravi, R. Pillai, K. Amaranathan, B. Pai, M. Chakraborty, Journal of Alloys and Compounds, 456 (2008) 201-210, *Fluidity of aluminium alloys and composites: A review*
Rederick and Mei, 2001	Rederick and Mei, Metalurgical and Materials Transactions B, 32 (2001), 1081 – 1093, *Inline detection of inclusions in melt*
Ricou and Vives, 1982	R. Ricou and C. Vives, International Journal of Heat and Mass Transfer, 25 (1982) 1579-1588, *Local velocity and mass transfer measurements in molten metals using an incorporated magnet probe*
Robson, 2004	J. Robson, Acta Materialia, 52 (2004) 4669-4676, *Modelling the overlap of nucleation, growth and coarsening during precipitation*

Robson and Prangnell, 2001 J. Robson, and P. Prangnell, Acta Materialia, 49 (2001) 599-613, *Dispersoid precipitation and process modelling in zirconium containing commercial aluminium alloys*

Rohatgi and Asthana, 2001 P. Rohatgi, R. Asthana, JOM, 53 (2001) 9-13, *Solidification science in cast MMCs: The influence of Merton Fleming*

Sajuri et al., 2006 Z. Sajuri, Y. Miyashita, Y. Hosokai, Y. Mutoh, International Journal of Mechanical Sciences, 48 (2006) 198-209, *Effects of Mn content and texture on fatigue properties of as-cast and extruded AZ61 magnesium alloys*

Salvo et al., 2003 L. Salvo, P. Cloetens, E. Maire, S. Zabler, J. Blandin, J. Buffiere, W. Ludwig, E. Boller, D. Bellet, C. Josserond, Nuclear Instruments and Methods in Physics Research B: Beam Interactions with Materials and Atoms, 200 (2003) 273-286, *X-ray micro-tomography an attractive characterisation technique in materials science*

Saunders, 2001 N. Saunders, Japan Institute of Light Metals, 51 (2001) 141-150, *The application of calculated phase equilibria to multicomponent aluminium alloys*

Saunders and Miodownik, 1998 N. Saunders, A. Miodownik, CALPHAD: Calculation of Phase Diagrams, A Comprehensive Guide, Pergamon, 1998

Saunders et al., 2003 N. Saunders, Z. Guo, X. Li, A. Miodownik, J. Schille, JOM, 55 (2003) 60-65, *Using JMatPro to model materials properties and behaviour*

Scarfe and Farman, 2008 W. Scarfe, A. Farman, The Dental Clinics of North America, 52 (2008) 707-730, *What is cone beam CT and how does this work?*

Sengupta et al., 2005 J. Sengupta, B. Thomas and M. Wells, Metallurgical and Materials Transactions A, 36 (2005) 187-204, *The use of water cooling during the continuous casting of steel and aluminium alloys*

Shukla and Pelton, 2009	A. Shukla and A. Pelton, Journal of Phase Equilibria and Diffusion, 30 (2009) 28-39, *Thermodynamic assessment of the Al-Mn and Mg-Al-Mn systems*
Simmons and Wang, 2000	J. Simmons, C. Shen, Y. Wang, Scripta Materialia, 43 (2000) 935-942, *Phase field modelling of simultaneous nucleation and growth by explicitly incorporating nucleation events*
Sin et al., 2007	S. Sin, D. Dube, R. Tremblay, Materials Characterisation, 58 (2007) 989-996, *Characterisation of Al-Mn particles in AZ91D investment castings*
Smith, 1982	R. Smith, Ultrasonics, 20 (1982) 211-214, *The effect of grain size distribution on the frequency dependence of the ultrasonic attenuation in polycrystalline materials*
Spencer, 2008	P. Spencer, Calphad, 32 (2008) 1-8, *A brief history of CALPHAD*
Sproule , 1967	D. Sproule, Non-Destructive Testing, 1 (1967) 91-98, *Information from ultrasonic flaw detection*
Srivatsan and Wie, 1995	T. Srivatsan, L. Wie, JOM, 30 (1995) 1832-1838, *The tensile behaviour of rapidly solidified magnesium alloys*
StJohn and Qian, 2009	M. Qian and D. StJohn, International Journal of Cast Metals Research, 22 (2009) 256-259, *Grain nucleation and formation in Mg-Zr alloys*
Sumitomo et al., 2002	T. Sumitomo, C. Caceres, M. Veidit, Journal of Light Alloys, 2 (2002) 49-56, *The elastic modulus of cast Mg-Al-Zn alloys*
Szekely and Yadoya, 1927	J. Szekely, R. Yadoya, Metallurgical Transactions, 3 (1927) 2673-2680, *The physical and mathematical modelling of the flow field in the mold region in continuous casting systems: Part 1. Model studies with aqueous systems*
Tamura et al., 2003	Y. Tamura, J. Yagi, T. Motegi, N. Kono, H. Tamehiro, Materials Science Forums, 419-422 (2003) 703-708,

Manganese-Bearing Particles in Liquid AZ91 Magnesium Alloy

Thomas, 2001 — B. Thomas, Encyclopaedia of Materials: Science and Technology, (2001) 1599-1609, *Continuous Casting: Complex Models*

Thomas and Zhang, 2001 — B. Thomas, L. Zhang, ISIJ International (Japan), 41 (2001) 1181-1193, *Mathematical modelling of fluid flow in continuous casting*

Thompson, 1984 — R. Thompson, Wave Propagation in Homogenous Media and Ultrasonic Non-destructive Evaluation, 1984, *Application of elastic wave scattering theory to the detection and characterisation of flaws in structural materials*

Thorvaldsen and Aliravci, 1992 — A. Thorvaldsen, C. Aliravci, 1992, 227, *Adv. Prod Fabr Light Met Met Matrix Comp. In: Proceedings of the International Symposium*

Tiryakioglu, 2008 — M. Tiryakioglu, Material Science and Engineering: A, 476 (2008) 174-177, *On the size distribution of fracture-initiating defects in Al- and Mg- alloy castings*

Turski, 2013 — M. Turski, Private Communication, 2013

Tzamtzis et al., 2009 — S. Tzamtzis, H. Zhang, G. Liu, Y. Wang, N. Babu, Z. Fan, Magnesium Technology Symposium, San Francisco, 2009, *Melt conditioned high pressure die casting (MC-HPDC) of Mg-alloys*

Vreeman and Incropera, 2000 — C. Vreeman, F. Incropera, International Journal of Heat and Mass transfer, 43 (2000) 677-686, *The effect of free-floating dendrites and convection on macrosegregation in direct chill casting aluminium alloys: Part 1 model development*

Vreeman and Incropera(b), 2000C. Vreeman and F. Incropera, International Journal of Heat and Mass transfer, 43 (2000) 687-704, *The effect of free-floating dendrites and convection on macrosegregation in direct chill casting aluminium alloys: Part 2 predictions for Al-Cu and Al-Mg alloys*

Vugt and Froyen, 2000 L. Vugt, L. Froyen, Journal of Processing Materials and Technology, 104 (2000) 133-144, *Gravity and temperature effects on particle distribution in Al-Si/SiC composites*

Wagner and Kampmann, 1991 R. Wagner, R. Kampmann, Materials Science and Technology: A Comprehensive Treatment, VCH New York, (1991) 213

Wang et al., 2002 Y. Wang, B. Sun, Q. Wang, Y. Zhu, W. Ding, Materials Letters, 53 (2002) 35-39, *An understanding of the hot tearing mechanism in AZ91 magnesium alloy*

Wang et al., 2003 Y. Wang, Q. Wang, C. Ma, W. Ding, Y. Zhu, Material Science and Engineering: A, 342 (2003) 178-182, *Effects of Zn and RE additions on the solidification behaviour of Mg-9Al magnesium alloy*

Wang et al., 2009 L. Wang, H. Rhee, S. Felicelli, A. Sabau, J. Berry, Shape Casting: The 3rd International Symposium, TMS, 2009, *Oxide film and porosity defects in magnesium alloy AZ91*

Wang et al., 2010 Y. Wang, M. Xia, Z. Fan, X. Zhou, G. Thompson, Intermetallics, 18 (2010) 1-7, *The effect of Al_8Mn_5 intermetallic particles on grain size of as-cast Mg-Al-Zn AZ91D alloy*

Wannasin et al., 2007 J. Wannasin, D. Schwam, J. Wallace, Journal of Materials Processing Technology, 191 (2007) 242-246, *Evaluation of methods for melt cleanliness assessment in die castings*

Watson et al., 2005 G. Watson, M. Forster, P. Lee, R. Dashwood, R. Hamilton, A. Chirazi, Composites part A: Applied science and Manufacturing, 36 (2005) 1177-1187, *Investigation of the*

clustering behaviour of titanium diboride particles in aluminium

Weiler et al., 2005 — J. Weiler, J. Wood, R. Klassen, E. Maire, R. Berkmortel, G. Wang, Materials Science and Engineering: A, 395 (2005) 315-322, *Relationship between internal porosity and fracture strength of die-cast magnesium AM60B alloy*

Weissenfluh, 1985 — T. Weissenfluh, International Journal of Heat and Mass Transfer, 28 (1985) 1563-1574, *Probes for local velocity and temperature measurements in liquid metal flow*

Xu et al., 1998 — D. Xu, W. Jones, J. Evans, D. Cook, Applied Mathematical Modelling, 22 (1998) 883-893, *Mathematical and physical modelling of systems for metal delivery in the continuous casting of steel and DC casting of aluminium*

Xu et al., 2009 — S. Xu, N. Matsumoto, S. Kamado, T. Honma, Y. Kojima, Materials Science and Engineering: A, 523 (2009) 47-52, *Effect of Mg17Al12precipitates on the microstructural changes and mechanical properties of hot compressed AZ91 magnesium alloy*

Ye and Liu, 2006 — H. Ye, X.Liu, Journal of Alloys and Compounds, 419 (2006) 54-60, *In situ behaviours of Al_8Mn_5 particles in Mg-Al alloys*

Youssef et al., 2005 — Y. Youssef, R. Dashwood, P. Lee, Composites: Part A, 36 (2005) 747-763, *Effect of clustering on particle pushing and solidification behaviour in TiB2 reinforced aluminium PMMCs*

Yuan and Thomas, 2005 — Q. Yuan, B. Thomas, 3rd International Congress on Science and Technology of Steel Making, Charlotte, 2005, *Transport and Entrapment of particles in continuous casting of steel*

Zeng, 2001 — G. Zeng, Computerized Medical Imaging and Graphics, 25 (2001) 97-103, *Image reconstruction – a tutorial*

Zhang et al., 2005 M. Zhang, P. Kelly, M. Qian, J. Taylor, 53 (2005) 3261-3270, *Crystallography of grain refinement in Mg-Al based alloys*

Zhang, 2006 L. Zhang, Fifth International conference on CFD in the Process Industries, Australia, 2006, *Fluid flow and inclusion removal in molten steel continuous casting strands*

Zhou et al., 2007 J. Zhou, D. Zhao, R. Wang, Z. Sun, J. Wang, J. Gui, O. Zheng, Materials Letters, 61 (2007) 4707-4710, *In situ observations of ageing process and new morphologies of continuous precipitates in AZ91 magnesium alloys*

Zuidema and Katgerman, 2002 J. Zuidema jr., L. Katgerman, Materials Science Forum, 396-402 (2002) 65-70, *Upstream fluid flow effects in aluminium DC casting*

Zuo et al., 2011 Y. Zuo, B. Jiang, Z. Fan, Materials Science Forum, 690 (2011) 137-140, *Microstructures of DC Cast Light Alloys under the Influence of Intensive Melt Shearing*

Appendix 1

Temper designations for magnesium alloys.

General Divisions	
F	As fabricated
O	Annealed recrystallised (wrought products)
H	Strain hardened
T	Thermally Treated to produce stable tempers
W	Solution heat treated
Subdivisions of H	
H1	Strain hardened only
H2	Strain hardened and then partially annealed
H3	Strain hardened and then stabalised
Subdivisions of T	
T1	Cooled and naturally aged
T2	Annealed
T3	Solution heat treated and then cold worked
T4	Solution heat treated
T5	Cooled and artificially aged
T6	Solution heat treated and artificially aged
T7	Solution heat treated and stabilised
T8	Solution heat treated, cold worked and artificially aged
T9	Solution heat treated, artificially aged and cold worked
T10	Cooled, artificially aged and cold worked

Appendix 2

Thermal Data from JMatPro used for flow modelling in Alsim software.

(K) T	(kg/m^3) Density	(J/Kg K) Specific Heat	(W/(m*K)) Thermal Conductivity	Fraction Liquid
973.15	1626.98	1387.4	79.0587	1
963.15	1629.55	1387.4	78.3876	1
958.15	1630.83	1387.4	78.05205	1
948.15	1633.39	1387.4	77.38095	1
943.15	1634.66	1387.4	77.0454	1
933.15	1637.19	1387.4	76.3743	1
928.15	1638.45	1387.2	76.03875	1
918.15	1640.97	1379	75.36765	1
913.15	1642.22	1373.8	75.03209	1
903.15	1644.71	1363.2	74.36099	1
898.15	1645.95	1358.4	74.02544	1
888.15	1648.43	1348.2	73.35434	1
878.15	1650.89	1340.47	72.68324	1
873.15	1658.93	8087.6	76.39571	0.88482
863.68	1672.13	5704.8	82.8927	0.69952
858.15	1678.04	4279.6	85.93995	0.62076
848.15	1686.49	3416.4	90.43761	0.51403
838.15	1693.04	2859.4	93.9279	0.43751
828.15	1698.34	2481.4	96.65478	0.38028
818.15	1702.82	2214.6	98.78978	0.33604
808.15	1706.7	2033.4	100.46597	0.30088
804.83	1707.89	1881.4	100.9384	0.29079
798.15	1710.16	1765.4	101.79312	0.27217

788.15	1713.31	1675.6	102.83716	0.24832
778.15	1716.2	1604	103.64951	0.22828
768.15	1718.89	1546	104.27555	0.2112
758.15	1721.43	1498.4	104.74959	0.19641
748.15	1723.84	1458.6	105.0978	0.18348
738.15	1726.15	1425	105.34051	0.17203
728.15	1728.38	1396.8	105.49314	0.16181
718.15	1730.53	3220	105.56815	0.15259
714.53	1731.29	1445.4	105.57788	0.14948
708.15	1732.62	1191	105.57587	0.14423
703.15	1739.36	1186.6	108.65237	0.0506289
693.15	1743.36	1181.8	109.8982	0.00441725
683.15	1744.97	1177.2	109.6177	0
673.15	1746.59	1172.6	109.17546	0
668.15	1747.39	1170.4	108.95437	0
658.15	1748.99	1165.8	108.51224	0
653.15	1749.79	1163.6	108.29121	0
643.15	1751.39	1159.2	107.84922	0
638.15	1752.18	1156.8	107.62826	0
628.15	1753.77	1152.4	107.18643	0
623.15	1754.56	1150	106.96557	0
613.15	1756.13	1145.8	106.52393	0
608.15	1756.92	1143.4	106.30317	0
598.15	1758.48	1139.2	105.86176	0
593.15	1759.26	1136.8	105.64112	0
583.15	1760.81	1132.6	105.19998	0
578.15	1761.59	1130.4	104.97948	0